

REVIEW

[View Article Online](#)  
[View Journal](#) | [View Issue](#)



Cite this: *Inorg. Chem. Front.*, 2024, **11**, 7682

## Active molecular units in metal organic frameworks for artificial photosynthesis

Subrata Mandal, <sup>a</sup> Sahar Yoosefi, <sup>a</sup> Alexander K. Mengele, <sup>a</sup> Sven Rau <sup>\*a</sup> and Andrea Pannwitz <sup>\*a,b</sup>

Metal organic frameworks (MOFs) are polymeric solid-state coordination compounds that can link photoactive and catalytically active molecular entities and maintain their activity and mechanism within their 3D structure, resembling the large photosynthetic apparatus in natural photosynthesis. This review categorizes photocatalytically active MOFs according to their structural properties and the location of the photosensitizer (PS) and catalyst (CAT) in the following types with respect to the linker and secondary building unit (SBU): (I) the PS and CAT are represented or localized at the linker and SBU, respectively, (II) the PS and CAT are represented or localized by/at different linkers, (III) the PS and CAT are both bound to the SBU, (IV) the PS and CAT are bound to the linker or SBU but as a PS-CAT dyad, and (V) the PS and/or CAT are assembled non-covalently within MOF pores. Furthermore, all reported studies on artificial photosynthesis are summarized in the context of light-driven H<sub>2</sub> evolution, CO<sub>2</sub> reduction, overall water splitting, water oxidation and other oxidations such as alcohol and amine oxidation, which are relevant in the field of artificial photosynthesis. Additionally, this review presents an overview on the stability and repair strategies for these MOFs.

Received 30th May 2024,  
Accepted 10th September 2024  
DOI: 10.1039/d4qi01363h  
[rsc.li/frontiers-inorganic](http://rsc.li/frontiers-inorganic)

<sup>a</sup>Institute of Inorganic Chemistry I, Ulm University, Albert-Einstein-Allee 11, 89081 Ulm, Germany. E-mail: [sven.rau@uni-ulm.de](mailto:sven.rau@uni-ulm.de), [andrea.pannwitz@uni-ulm.de](mailto:andrea.pannwitz@uni-ulm.de)

<sup>b</sup>Institute of Inorganic and Analytical Chemistry, Faculty of Chemistry and Earth Sciences, Friedrich-Schiller University Jena, Humboldtstraße 8, 07743 Jena, Germany. E-mail: [andrea.pannwitz@uni-jena.de](mailto:andrea.pannwitz@uni-jena.de)



Subrata Mandal

Dr Subrata Mandal received his PhD in chemistry from the Indian Institute of Technology, Kharagpur, India, in 2021 under the guidance of Prof. Rajakumar Ananthakrishnan. His doctoral thesis focused on the strategic synthesis and characterization of semiconductors and hybrid materials for photocatalytic and sensory applications. He is currently a postdoctoral researcher at the Institute of Inorganic Chemistry I, Ulm University, Germany. His research centers on the synthesis and characterization of metal complex-based coordination compounds for artificial photosynthesis, exploring various matrices such as metal-organic frameworks and lipid bilayers.

## 1. Introduction

Since fossil fuel supplies are limited, alternative energy sources such as solar energy are becoming more significant in the energy market and chemical industry. The knowledge about photosynthetic processes in green plants provides a very good perspective on the concepts needed and their interplay in accomplishing sustainable light-driven catalysis. Translation



Sahar Yoosefi

Sahar Yoosefi is a second-year PhD student in the Department of Inorganic Chemistry I at Ulm University, working under the supervision of Prof. Sven Rau. She earned her bachelor's degree in chemistry from Shahid Beheshti University in 2015 and her master's degree in inorganic chemistry from the University of Tehran in 2018. Her research interests focus on the synthesis and characterization of photoactive metal-organic frameworks for solar energy conversion and storage. She was awarded the LGFG (Landesgraduiertenförderungsgesetz) scholarship from Ulm University to pursue her PhD studies.



of key concepts into artificial processes provides a very attractive avenue for sustainable solar fuel generation and other photochemical conversions. One of these promising concepts is artificial photosynthesis, which links several redox processes and utilizes light energy to perform precise energy conversion, chemical synthesis, and, consequently, energy storage.<sup>1,2</sup> Therefore, the development of artificial photosystems or photocatalysts that mimic natural process by converting  $\text{H}_2\text{O}$  and  $\text{CO}_2$  into energy-rich reduced products or organic compounds into valuable goods has attracted considerable interest. In this regard, a general perspective on the elementary photochemical and -physical steps in natural and artificial photosynthesis is provided to highlight the inspiration for MOF designs discussed herein and set the basis for the discussion on MOF-based solar fuel generation.

### 1.1. Elementary photochemical and -physical steps leading to photocatalysis

Generally, photocatalytic processes are initiated by (visible) light excitation of a photosensitizer (PS), leading to the formation of an electronically excited state  $\text{PS}^*$ .<sup>3,4</sup> As the uptake of extra photonic energy makes  $\text{PS}^*$  easier to be oxidized and reduced simultaneously compared to its electronic ground state, redox reactions with a variety of suitable reagents can occur upon the absorption of photons. By increasing the effective local concentration of these reagents and adjusting thermodynamic driving force for desired forward electron transfer *via* redox potential tuning, photocatalytic processes can be improved.<sup>3</sup> Following photon absorption, the reduction or oxidation of  $\text{PS}^*$  is called reductive or oxidative quenching, respectively, and regardless of the mechanism, both processes lead to the formation of highly reactive reduced and oxidized products. Consequently, efficiency-limiting charge recombination processes, which typically possess large driving force,

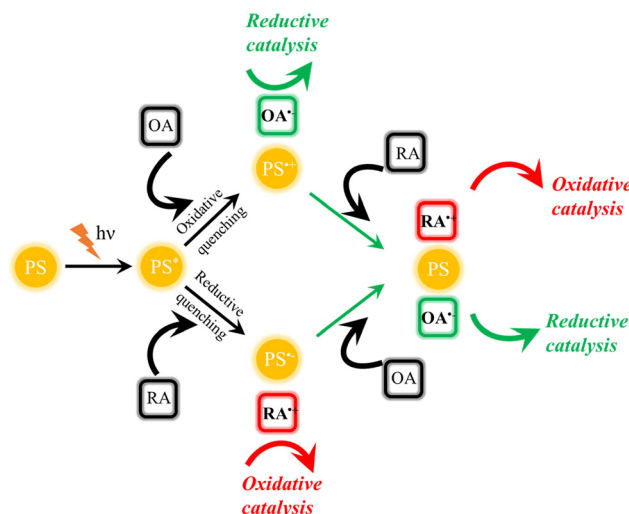


Fig. 1 Principle of photochemical processes leading to redox processes (PS: photosensitizer, OA: oxidizing agent, and RA: reducing agent).

have to be minimized by outcompeting them kinetically. If this is achieved by comparably fast subsequent electron transfer steps involving the transiently reduced or oxidized PS, *i.e.*,  $\text{PS}^-$  or  $\text{PS}^+$ , respectively, the restoration of PS and, consequently, closing of the catalytic cycle are achieved, as shown in Fig. 1. In this scheme, if the oxidizing agent (OA) and/or the reducing agent (RA) are represented by a (molecular) catalyst (CAT) capable of facilitating specific small molecule activation, artificial photosynthetic systems are generated.

### 1.2. Molecular building blocks in natural photosynthesis and enzyme catalysis

Although at first sight the similarities between heterogeneous photoactive MOF materials and the soft matter (= thylakoid



Alexander K. Mengelé

*NADH and ATP formation. He is also applying supramolecular chemistry to accelerate selective NADH photooxidations for NAD<sup>+</sup>-driven enzymatic oxidations.*



Sven Rau

*Prof. Dr Sven Rau studied chemistry at the Friedrich-Schiller-University of Jena and Dublin City University. He obtained his Diploma in chemistry in 1997 and his PhD in 2000. Following his habilitation in 2007, he took on a W 2 professorship at the Friedrich-Alexander-University Erlangen-Nuremberg in 2008. Since 2011, he has been leading the Institute for Materials and Catalysis at Ulm University. Since 2018, he has been the spokesperson of the CRC CataLight, and since 2022 he has been a co-spokesperson. His research interests include the synthesis and characterization of photoredox-active metal complexes and their applications in light-driven catalytic conversions, photoelectrochemistry, and photodynamic therapy.*



membrane) embedded natural photosynthetic apparatus seem limited, there are several commonalities, allowing the development of biomimetic design strategies for the future optimization of the photoactivity of MOFs. As generalized in Fig. 1, nature has to adapt to the elementary processes to design an efficiently performing photocatalytic processes, where light excitation in the P680 and P700 dimeric chlorophyll reaction centers ultimately leads to long-range charge transfers. The reaction sequence in both schemes follows an oxidative quenching mechanism. A detailed description is provided for P700 in photosystem I of green plants, where the excited state is quenched by electron transfer to the phylloquinone A1 (Vitamin K1) aided by auxiliary chlorophyll molecules (Fig. 2a). This generates a charge-separated state with a distance of 25–30 Å for the radical cationic P700 and anionic A1.<sup>5,6</sup> This efficient long-range electron transfer between molecular entities is only possible because each entity is integrated into a rigid protein scaffold, ensuring the optimal distance and orientation to allow electron transfer to proceed with high efficiency.<sup>7</sup> This large charge separation distance not only effectively suppresses the thermodynamically favorable back-electron transfer but also fast reduction of the P700 radical cation by plastocyanin, a copper-based protein. On the other side of the redox chain, reduced A1 reduces an adjacent iron sulphur cluster, which is also spatially fixed by protein integration, consequently providing reducing equivalents for final electron fixation *via* the conversion of NADP<sup>+</sup> to NADPH<sub>2</sub><sup>+</sup>.

In enzymatic catalysis, besides long-range electron transfer, other cofactors are also precisely managed by three-dimensional biological scaffolds to influence the catalytic performances. Therefore, the outer coordination spheres play a significant role. The third coordination sphere manages the long-range transport of cofactors such as electrons, hydride equivalents and other species to facilitate reactive pathways, while the 2<sup>nd</sup> coordination sphere stabilizes the transition states and

reactive intermediates through non-covalent interactions at the molecularly defined catalyst. As a specific example (Fig. 2b and c), in proton reduction catalysts, [FeFe] hydrogenases (H<sub>2</sub>ases) have dedicated substrate and product channels together with an energetically highly tuned electron transport chain (Fig. 2b).<sup>8,9</sup> Importantly, the terminal hydride species, which is crucial for the function of the enzyme, is kinetically stabilized by hydrogen bonding interactions (Fig. 2c). The formation of the thermodynamically more stable μ-H product is prevented by a high energy transition state caused by interactions with the surrounding peptide matrix. Specifically, catalysis proceeds through a kinetically stabilized state before it converts to the thermodynamically more stable, and thus less reactive ground state. Therefore, this three-dimensional organization by protein integration of photochemically and redox active molecular building blocks into a suitable (soft matter) matrix provides the functional basis for harvesting solar energy in biological photosynthesis in a surprisingly good yield.<sup>10</sup> Accordingly, the rational matrix immobilization of catalytically active molecular species shows great potential for optimized artificial (photo)catalytic systems.

### 1.3. Artificial photosynthetic systems and their heterogenization

The above-described important steps in natural photosynthesis and enzyme catalysis, such as (visible) light-induced charge separation, suppression of charge recombination, terminal charge consumption by chemical catalysis, and outer coordination sphere interaction in the catalyst, have been translated to artificial systems (Fig. 2d–f). This started with the groundbreaking work by Lehn and Sauvage in the late 1970s,<sup>11</sup> generating a plethora of different functional unit-based materials and molecular units. However, the integration of these simple entities into function-enabling structural materials, *e.g.*, to achieve improved charge separation, has not been accomplished with sufficient precision to date. Thus, significant effort has been devoted to the development of bulk material photocatalysts such as metal oxides, metal chalcogenides, and organic semiconductors, or nanoparticulate compounds and their heterojunctions.<sup>12–23</sup> However, the molecular systems or structurally defined metal complexes are more relevant because they provide definite active sites and distinctive reaction mechanisms, and therefore can offer high product selectivity, scalability and atom economy.<sup>24–26</sup> Nevertheless, their separated forms (Fig. 2d) often fail to achieve precise proximity for electron transfer, leading to an increase in cross-reactivity. Thus, to overcome this, molecularly defined oligonuclear metal complexes containing PS bridged to CAT sites (Fig. 2e) provide sufficient precision but require significant effort for their synthesis.<sup>27</sup> Most importantly, the commonly observed lack of long-term stability and recyclability of homogenous systems has led to the development of heterogenized systems, trying to exploit the best properties of two components, in which molecular units such as PS and CAT and other cofactors are either directly assembled into a solid-state structure or immobilized onto freestanding solid materials



Andrea Pannwitz

*Jun.-Prof. Dr Andrea Pannwitz Since 2024 Andrea Pannwitz holds a CZS endowed junior professorship with tenure track for sustainable molecular catalysis for energy conversion and focus on light-driven processes at the Friedrich-Schiller-University Jena, Germany. She is also a young research group leader at Ulm University, Germany, where she had started her independent career in 2020. She completed postdoctoral research at Leiden*

*University in the Netherlands, obtained her PhD from the University of Basel, Switzerland, and studied Chemistry at the Georg-August-University in Göttingen, Germany.*



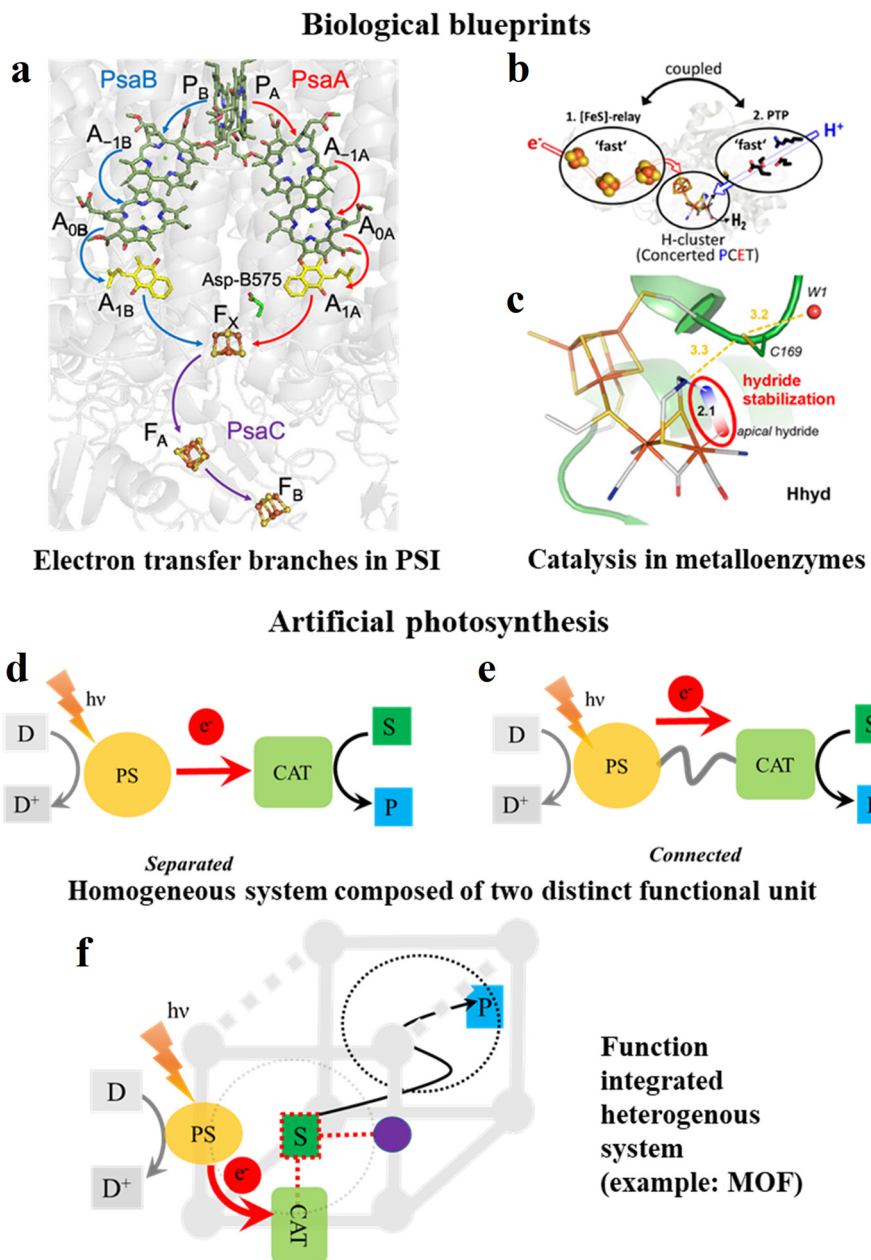


**Fig. 2** Electron transfer and catalysis aspects in biological blueprints vs. artificial photosynthesis. (a) Protein-bound functional building blocks in photosystem I, where P = P700, A<sub>1A</sub> and A<sub>1B</sub> represent the phylloquinones of both active branches in photosystem I, and F<sub>X</sub> is the first Fe<sub>4</sub>S<sub>4</sub> cluster of photosystem I. The protein scaffold is depicted in shaded grey. Reprinted with permission from ref. 5. Copyright 2022, the American Chemical Society. (b) Depiction of the proton and electron transfer pathways of FeFe hydrogenase. Adapted with permission from ref. 8 and 9. Copyright 2020, National Academy of Sciences. (c) Active site of FeFe hydrogenase showing how the protonated bridgehead amino group can act via hydrogen bonding to stabilize a hydride intermediate. Numbers indicate distances in Å and the red-blue color scheme indicates negative and positive partial charges, respectively. Adapted with permission from ref. 8 and 9. Copyright 2019, the American Chemical Society. (d–f) Schematic of artificial photosynthesis (example: a typical photocatalytic reduction reaction) with active molecular units in (d and e) homogenous (PS, and CAT units are either separated or connected), and (f) heterogenous (PS, CAT and other cofactor integrated MOF) conditions. (S = substrate, P = product, and D = sacrificial donor). Purple sphere in (f) represents an additional function-built linker, which can provide intermediate stabilization of the substrate through interaction and dotted circle is the pore of the MOF, indicating the feasibility of product diffusion.

(Fig. 2f).<sup>20,21,28–31</sup> This type of support should ideally provide synthetic flexibility to adjust the chemical environment beyond the initial coordination sphere, in addition to structurally stabilizing the catalytic site.<sup>32,33</sup> Supramolecular struc-

tures such as cages, polymers, dendrimers, and zeolites are a few examples of this tactic<sup>34–36</sup> but they are frequently quite challenging in terms of synthesis, and in particular zeolites have limited synthetic flexibility.

#### 1.4. Scope of this article

Therefore, this review focuses on an alternative heterogenization approach that involves adding molecularly defined catalytic/light-absorbing function to metal–organic frameworks (MOFs), which are three-dimensional (3D) coordination polymers composed of metal cations or their clusters (referred to as secondary building units or SBUs, respectively), which are periodically linked by organic linker molecules.<sup>37</sup> When creating highly active catalysts, the high interior surface areas and high porosity of MOFs are desirable characteristics. They may also be electrically conductive through band-like charge transport or hopping mechanisms.<sup>38</sup> Furthermore, MOFs are desirable platforms for the methodical engineering of outer-sphere interactions due to their high degree of modularity and the available variety of synthetic functionalization techniques utilizing organic chemistry.<sup>33,39</sup> Simultaneously, the high local concentration of active components being linked within the MOF structure leads to improved charge transfer properties, and thus optimized photocatalytic activity.

Therefore, we discuss MOFs in which their essential components enabling artificial photosynthesis are molecularly defined entities and will describe the construction opportunities and classification of these MOFs for application in the area of solar fuel generation. Importantly, herein, we summarize the photocatalytic MOFs based on their reaction scope including light-driven hydrogen evolution reaction (HER), oxygen evolution reaction (OER), overall water splitting, CO<sub>2</sub> reduction reaction (CO<sub>2</sub>RR), amine oxidation, and alcohol oxidation reactions. Considering sustainability, we also present general strategies for improving the stability of these MOFs and repair approaches.

## 2. Construction of MOFs

MOFs are crystalline and porous materials assembled from rigid bi- or multi-podal organic linkers connecting a metal node or SBU into a three-dimensional (3D) lattice structure, as shown in Fig. 3.<sup>40–42</sup> The first example of this class of solid

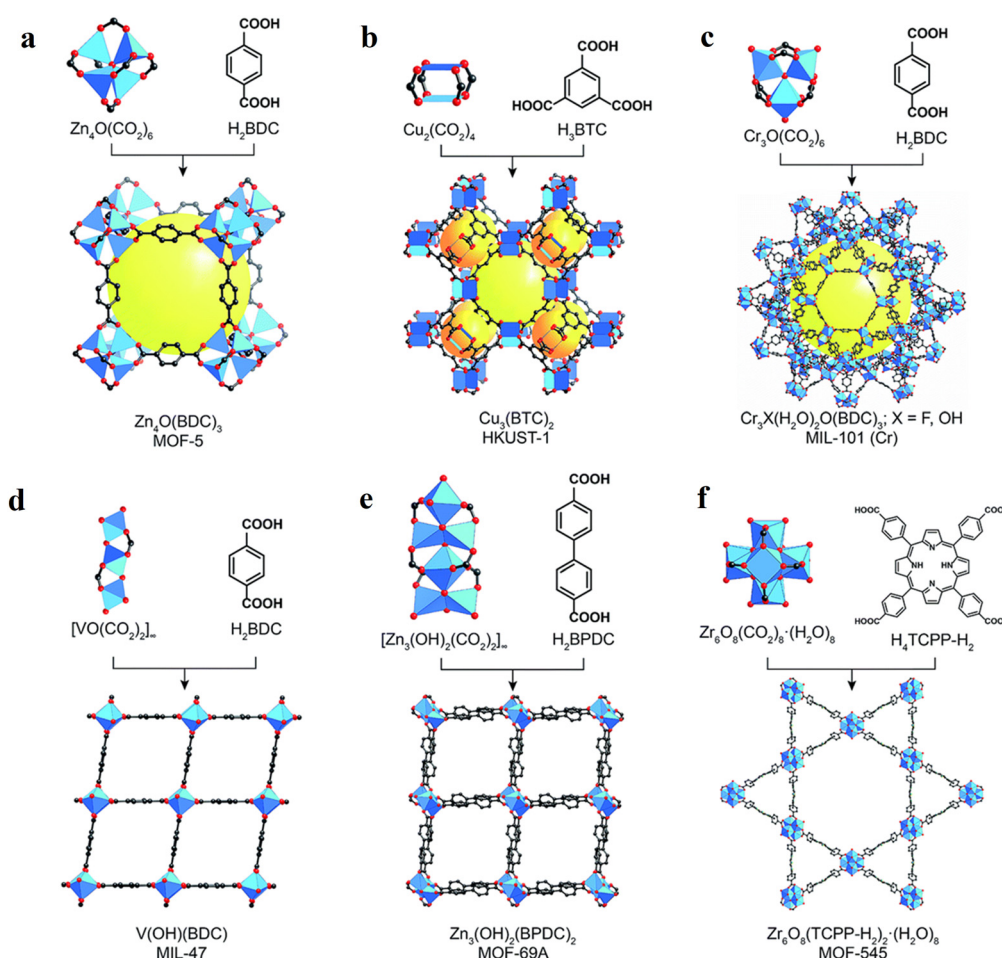


**Fig. 3** Representation of some common secondary building units (SBUs) and linker combinations to afford a selection of MOFs such as (a) MOF-5, (b) HKUST-1, (c) MIL-101(Cr), (d) MIL-47, (e) MOF-69A, and (f) MOF-545. Atom labelling: C, black; O, red; metals, and blue polyhedra. H atoms are omitted for clarity. Yellow and orange spheres represent the space in the framework. Reproduced with permission from ref. 51. Copyright 2017, the Royal Society of Chemistry.



materials was found in 1999, when Yaghi and co-workers crystallized a robust and highly porous solid (namely MOF-5:  $\text{Zn}_4\text{O}(\text{BDC})_3(\text{DMF})_8(\text{C}_6\text{H}_5\text{Cl})$ , BDC = 1,4-benzene dicarboxylate, DMF = dimethylformamide).<sup>43</sup> This archetype solid was comprised of  $\text{Zn}_4\text{O}(\text{CO}_2)_6$  octahedral SBUs each linked by six chelating BDC units to give a cubic framework. Following this seminal work, the associated building blocks in the main type of MOFs, *i.e.*, metal-oxo clusters (referred to as  $\text{M}_n$ ) bearing carboxylate organic moieties as functional linkers attached to these clusters, can also be viewed as the nm-controlled version of dye-sensitized solar cells (DSSCs) or dye-sensitized photoelectrochemical cells (DSPECs), where dye (and/or CAT) cover the surface of a metal-oxo semiconductor *via* carboxylate anchors.<sup>44</sup> As illustrated by a few examples in Fig. 3, the variation in the linkers and SBUs can lead to diverse structures, making MOFs highly tunable materials. The large number of available SBUs and linkers enables the design of countless 3D MOFs, showcasing unique structures, which differ in topology, reactivity, stability, pore size, and internal surface area.<sup>42,43,45–47</sup> The geometry of the linker and SBU and their connection also enables the creation of other structures, such as zero-dimensional (0D) metal-organic polyhedra (MOPs), and 2D-metal-organic layer (MOLs) structures.<sup>41,48</sup> Superior to the classical solid-state materials and semiconductors, MOFs provide the beneficial mass transport characteristics of substrates and simple product-catalyst separation, allowing their facile recycling.<sup>47,49,50</sup> Most importantly, the backbones (linker and SBU) of MOFs can preserve their molecular characteristics such as light absorption properties and redox activities within these porous structures, allowing the bottom-up design of functional (photocatalytically active) materials.

In addition, MOFs can be functionalized with molecular moieties to provide molecule-inherent photoactivity and catalytic function. These units can be integrated into MOFs either through covalent interactions using the linker and SBUs or by non-covalent interactions within the pores (see Fig. 4). The advantage of the covalent functionalization of the SBU and linker is that the microscopic structural integrity of the MOF and the structure of the added molecular components are typically maintained. In the case of non-covalent functionalization, the pores of MOFs can be loaded reversibly with active molecular components with an appropriate size in addition to the uptake of the substrate. A molecular component relevant to artificial photosynthesis (CAT or PS) can be incorporated into MOFs using a direct one-pot synthesis method, as follows: (i) *via* “linker engineering approach” (reactive center is structurally tailored to serve as the linker during framework formation) and (ii) encapsulation strategy. In contrast, post-synthetic methods involve synthesizing molecular species and MOF scaffolds separately, and then combining them by soaking the virgin MOFs in a solution of the compounds or their precursors. Therefore, this allows the molecules to dock at a node (node-docking), linker (linker docking), or cavity (ship-in-a-bottle), respectively. The details of these strategies have been described in the review by Waran and co-workers.<sup>52</sup> The direct injection of the molecular species into

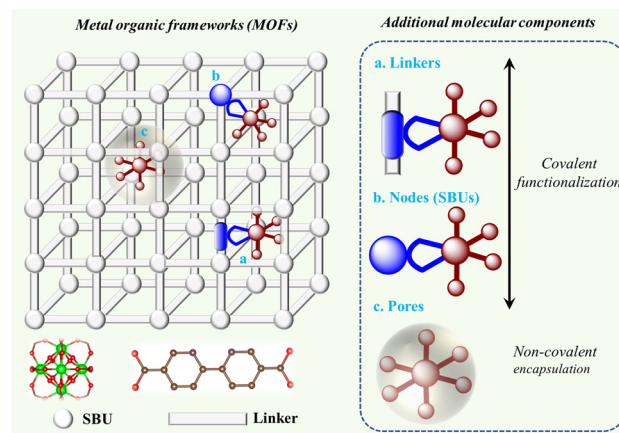


**Fig. 4** Schematic representation of the an exemplary MOF having three distinct types of molecular component (PS/CAT) functionalizations *via* covalent interaction at (a) linkers, (b) nodes/SBUs, and (c) non-covalent interaction at the pores. In the same category of noncovalent encapsulation (c), direct injection of the molecular components into the solution during the photocatalytic experiment is also considered as the MOF offers porous channels to transport and interact with the active sites. (Additional molecular components include (a) an octahedral metal complex with bipyridine-like dicarboxylate, (b) monocarboxylate anchoring motif, and (c) coordinatively isolated segment. The SBU represents a metal-oxo cluster, while the linker is a biphenyl dicarboxylate. The blue-highlighted regions emphasize the scaffolds connected to the metal complex through anchoring motifs, with the sphere representing the pore space within the framework.)

the solution during the photocatalytic experiment is also considered in the same category of noncovalent encapsulation assuming that the MOF offers porous channels for the species to interact with the active sites.

## 2.1. Modular MOF constructions for artificial photosynthesis

Molecular photoactive (PS) or catalytically active units (CAT) can be incorporated/built into the MOF structure through various synthetic steps, as described above. Therefore, the resulting MOF structures can be grouped based on the localization of the individual functional modules at or in the MOF, leading to the following five options, which are also represented in Fig. 5.

**2.1.1. Type I-MOF, linker-SBU.** The organic or metalloligand-based linker in MOFs acts as PS and SBU or an additional molecular species covalently attached to SBU serves as CAT (Fig. 5). Most of the examples in this section refer to MOFs that are built from high-valent metal-based SBUs of Zr (IV), Ti(IV), Ce(IV), Ru(III), Eu(III), and Bi(III) and a strong light-absorbing linker such as 2-aminoterephthalate ( $\text{NH}_2\text{-BDC}$ ), tetrakis(4-carboxyphenyl)porphyrin (TCPP), and Ru(II)-polypyridyl carboxylate derivatives.<sup>53–64</sup> Typically, in metalloligand linker-based MOFs, the origin of light absorption results from the direct metal coordination sphere (for example, metal-to-ligand charge transfer, MLCT-based excitation), whereas, in organic linker-based MOFs, it can be ligand-centered (LC) or ligand-to-metal charge transfer (LMCT) states that induce photoactivity.



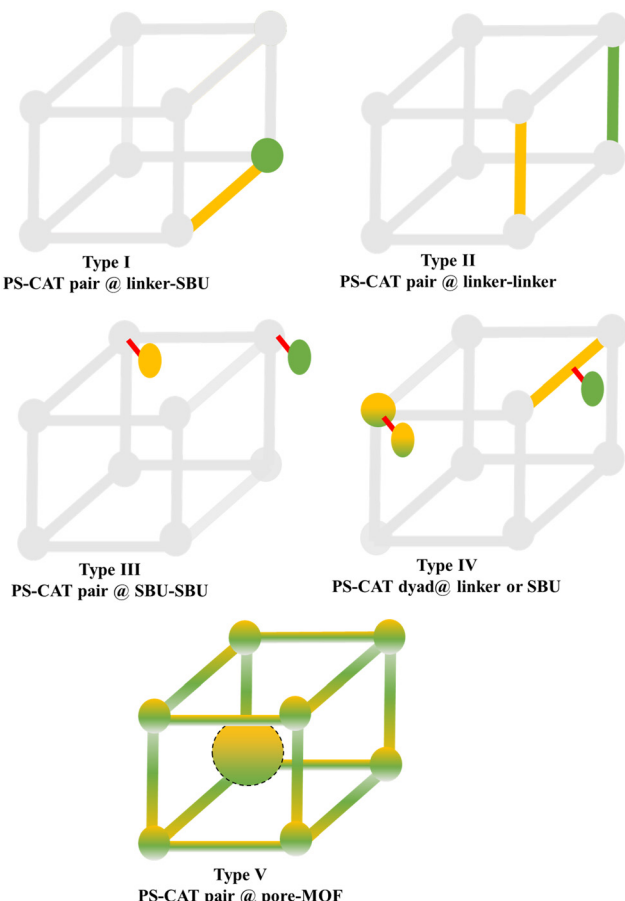


**Fig. 5** Schematic representation of the types of photocatalytic MOFs based on the localization of individual functional modules (Type I, linker-SBU: bare/functionalized linker (PS)-bare/functionalized SBU (CAT); Type II, linker-linker: bare/functionalized linker 1 (PS)-bare/functionalized linker 2 (CAT); Type III, SBU-SBU: bare/functionalized SBU (PS)-bare/functionalized SBU (CAT); Type IV, oligonuclear species at the SBU or at linker: PS-CAT dyad at the linker or PS-CAT dyad at the SBU; Type V: pore-MOF backbone: encapsulated or loaded species (PS/CAT)-pristine MOF or covalently functionalized MOF (CAT/PS)). Color code: yellow (PS); green (CAT); red line (covalently connected); yellow-green gradient (indicating that the location of PS and CAT can be altered), dashed circle (pore occupied by a noncovalently attached or isolated component).

The specific origin depends on the linker-SBU interaction and their orbital contribution in the ground state (HOCO/VB, highest occupied crystal orbital state/valence band) and excited state (LUOC/CB, lowest unoccupied crystal orbital state/conduction band) electronic structure. Despite the different origins of light absorption, the charge separation between two distinct scaffolds in these types of photocatalytic MOFs results in a transiently oxidized species at the linker and a reduced species at the SBU site (or *vice versa* in rare cases), which have enormous potential to drive redox reactions. One classical example is the  $\text{Ti}_8$  cluster-containing MOF,  $\text{NH}_2\text{-MIL-125}(\text{Ti})$  (Fig. 6a), which yields formate during the reduction of  $\text{CO}_2$  under the irradiation of visible light in the presence of triethanolamine (TEOA) as a sacrificial electron donor.<sup>65</sup> It was

proposed that the  $\text{NH}_2\text{-BDC}$  linker acts as the primary PS. Upon photoexcitation,  $\text{Ti}^{4+}$  is reduced to  $\text{Ti}^{3+}$  by the transfer of an electron from the excited  $\text{NH}_2\text{-BDC}$  linker to the SBU, creating a charge-separated state that can reduce  $\text{CO}_2$ . The electrons for this process are provided by TEOA, which reduce the transiently oxidized  $\text{NH}_2\text{-BDC}$  back to its starting state.

Moreover, structural engineering of the organic linker in type I-MOFs offers significant potential for (i) fine-tuning the electronic structure and light absorption properties, (ii) enhancing the charge carrier density and dynamics, (iii) modulating the porosity, and (iv) achieving greater stability of the substrate intermediate through interframework stabilization. This engineering includes either the introduction of electron-withdrawing and electron-donating substituents<sup>66</sup> or the linear and lateral  $\pi$ -expansion using oligo-arylene and azolinks.<sup>67-69</sup> Additionally, leveraging the semiconductive nature of MOFs and the multinuclearity of the SBU, the SBU-based CAT can accumulate multiple electrons simultaneously, making this type of MOF suitable for all types of reduction reactions such as HER,  $\text{CO}_2\text{RR}$  and reactive oxygen species generation (ROS) in the presence of a suitable donor.

**2.1.2. Type II-MOF, linker-linker.** In this type of MOFs, two organic linker or metalloligand linkers are confined in a closed space (Fig. 5). To ensure the structural integrity of the MOF and its formation, a prerequisite for these MOFs is that the linkers are similar in length. Importantly, one of these molecularly defined units acts as PS and another unit serves as CAT. This type of MOF is an ideal conceptualization of a function-integrated system, where the role of the MOF structure is to provide a nanoreactor-like reaction space within the porous channels<sup>70</sup> and support the molecularly defined PS and CAT unit to generate proximity between them to improve the charge transfer. Both factors contribute to achieving higher photocatalytic activity compared to their homogeneous control.<sup>71-74</sup> One elegant example is the  $\text{Zr}_6$ -based dual photocatalytic MOFs, namely mPT-Cu/Co comprised of a  $[\text{Cu}(\text{PT})(\text{dppe})]\text{PF}_6$  PS (dppe = 1,2-bis(diphenylphosphanyl)ethane, and PT = 4,4'-(1,10-phenanthroline-3,8-diyi)dibenzoate), and a  $[\text{Co}(\text{PT})]^{2+}$  CAT, yielding an impressive turnover number (TON) of 18 700 in the photocatalytic HER in the presence of BIH (1,3-dimethyl-2-phenyl-2,3-dihydro-1*H*-benzo[*d*]imidazole) which serves as a sacrificial electron donor (Fig. 6b).<sup>75</sup> Photocatalytic HER is initiated *via* the reductive quenching of  $\text{PS}^*$  by BIH, forming  $\text{PS}^-$ , which subsequently injects electrons to CAT for HER. Despite having a similar mechanism as observed for the homogeneous system, the authors demonstrated that the spatial proximity between PS and CAT (i) increased the stability of PS and molecular CATs and (ii) accelerated electron transfer processes between  $\text{PS}^-$  and CAT, which led to a significant boost (almost 95-fold enhancement over their homogeneous controls) in the photocatalytic activity of mPT-Cu/Co.

Moreover, this type II-MOF approach enhances the stability of the coordination sphere for both molecular PS and CAT concurrently within the MOF. This significantly contributes to improving the overall efficiency compared to their homogeneous counterparts. Examples of this type of photocatalytic



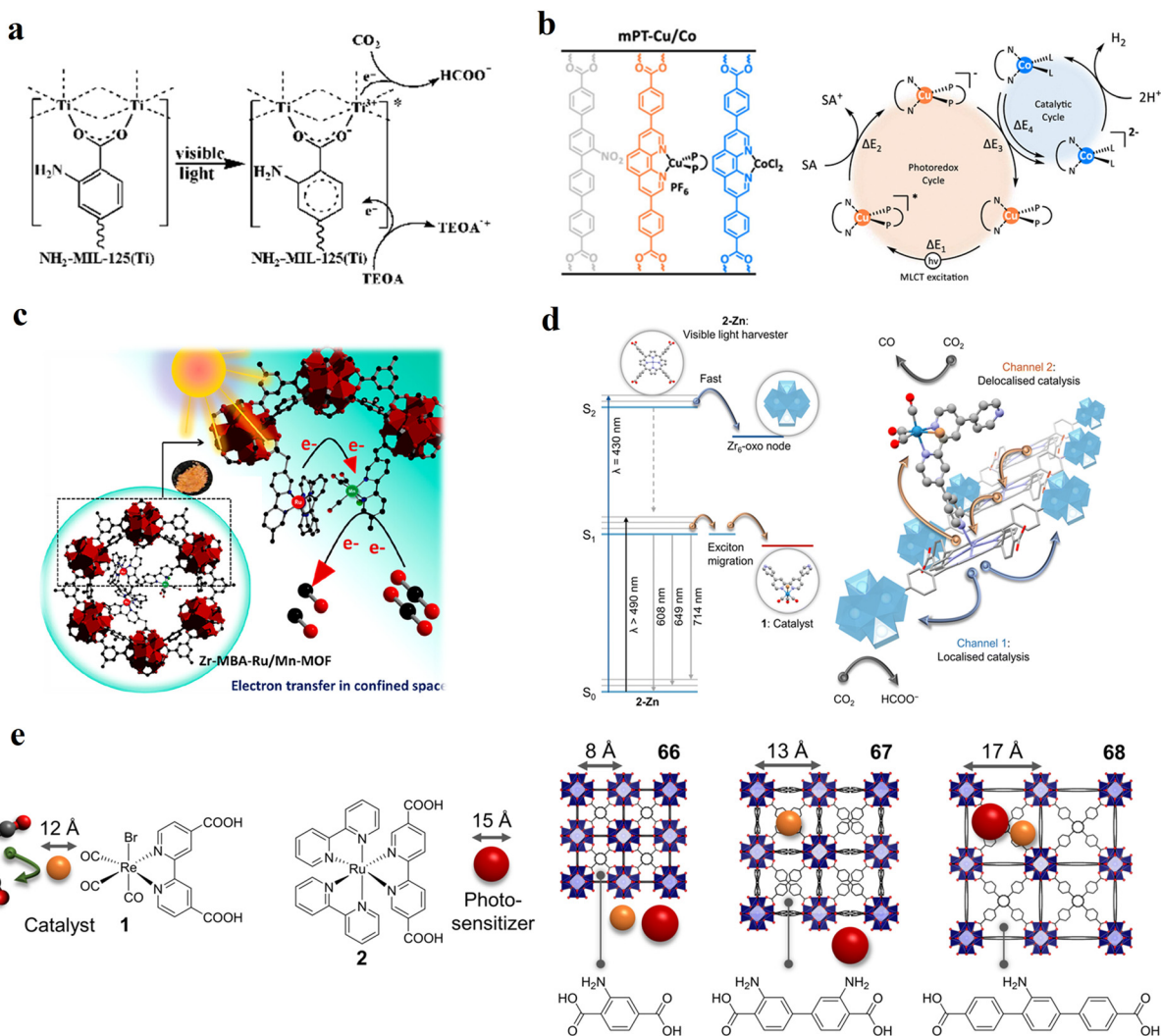


**Fig. 6** Examples of different types of PS-CAT pairs in MOF-based photocatalysis: (a) type I ( $\text{NH}_2\text{-BDC-Ti}_8$ , linker-SBU) in  $\text{NH}_2\text{-MIL-125 (Ti)}$  MOF. Adapted with permission from ref. 65. Copyright 2012, WILEY-VCH Verlag GmbH & Co. (b) Type II ( $[\text{Cu}(\text{PT})(\text{dppe})]\text{PF}_6\text{-}[\text{Co}(\text{PT})]^{2+}$ , linker-linker) in  $\text{mPT-Cu/Co}$  MOF. Adapted with permission from ref. 75. Copyright 2020, the American Chemical Society. (c) Type III ( $[\text{Ru}(\text{bpy})_2(\text{MBA})]\text{-}[\text{Mn}(\text{MBA})(\text{CO})_3\text{Br}]$ , SBU-SBU) in  $\text{Zr-MBA-Ru/Mn-MOF}$  (red balls: oxygen and black balls: carbon). Adapted with permission from ref. 79. Copyright 2023, the American Chemical Society. (d) Type IV (2-Zn-1 dyad) in Re-PCN hybrids (2-Zn:  $\text{Zn-TCPP}$  linker and 1:  $[\text{ReBr}(\text{CO})_3(\text{qtpy})]$ ). Reproduced with permission from ref. 82. Copyright 2022, the Royal Society of Chemistry. (e) Type V (encapsulated 1:  $[\text{ReBr}(\text{CO})_3(4,4'\text{-dcbpy})]$  and 2:  $[\text{Ru}(\text{bpy})_2(5,5'\text{-dcbpy})]\text{Cl}_2$ ) in various assembly-controlling MOF topologies  $\text{UiO}(66, 67, 68)$ . Adapted with permission from ref. 88. Copyright 2021, WILEY-VCH Verlag GmbH & Co.

MOFs are discussed in the respective chapters (Chapter 3.1–3.5).<sup>71,73,74,76,77</sup> Additionally, this approach unlocks significant opportunities for PS engineering. For example, Guo *et al.* demonstrated a method to markedly enhance the sensitizing capability of  $\text{UiO-67}$  MOFs, composed of Ir/Cu or Ir/Co pairs, by shifting the excited state distribution of Ir from  $^3\text{MLCT}$  to  $^3\text{IL}$  (intraligand).<sup>76</sup> This was achieved by incorporating a coumarin 6 (Cou-6) ligand to form the  $[\text{Ir}(\text{Cou-6})_2(5,5'\text{-dcbpy})]^+$  moiety ( $5,5'\text{-dcbpy} = 2,2'\text{-bipyridine-5,5'-dicarboxylate}$ ), replacing the 2-phenylpyridine (ppy) ligand in  $[\text{Ir}(\text{ppy})_2(5,5'\text{-dcbpy})]^+$ . The resulting hierarchical organization of  $^3\text{IL}$  MOFs, paired with Co (for hydrogen evolution) or Cu (for  $\text{CO}_2$  reduction) catalysts, facilitates efficient electron transfer. This

innovation led to remarkable photocatalytic  $\text{H}_2$  evolution, yielding  $26\,844.6\, \mu\text{mol g}^{-1}$ , and  $\text{CO}_2$  photoreduction, achieving a record  $\text{HCOOH}$  yield of  $4807.6\, \mu\text{mol g}^{-1}$ . Additionally, the isolated photocatalytic sites (PS/CAT pair) enable selective light excitation, thereby preventing any unintended damage to the modular construction.

**2.1.3. Type III-MOF, SBU-SBU.** The exploitation of photocatalytic MOFs with SBU/SBU-based PS/CAT pairs is less abundant given that it is a synthetic challenge to achieve MOFs with two molecularly defined units attached to two separate SBU scaffolds (Fig. 5). Most importantly, bare SBUs are found to be almost inert in harvesting visible light ( $\text{Ce}_6^{54}$  and  $\text{Fe}_3^{78}$  clusters are exceptional). However, the post-synthetic

functionalization of the SBU by the carboxylate function of an *N,N'*-chelating ligand (MBA = 2-(5'-methyl-[2,2'-bipyridin]-5-yl)acetate), followed by metalation in the chelating sites made it possible to achieve molecularly defined assemblies of PS/CAT pairs with close proximity. The most precise example is Zr-MBA-Ru/Mn MOFs, as reported by Karmakar *et al.*<sup>79</sup> The chosen Zr-MOF (= MOF-808) was first post-synthetically modified through the solvent-assistant exchange of formates with MBA ligands at the SBUs. By consecutive post-synthetic metalation with  $[\text{Ru}(\text{bpy})_2\text{Cl}_2]$  and  $[\text{Mn}(\text{CO})_5\text{Br}]$  both functional units were installed at the *N,N'*-chelating sites of the MBA ligands to afford the Zr-MBA-Ru/Mn-MOF (Fig. 6c). The built-in  $[\text{Ru}(\text{bpy})_2(\text{MBA})]^{2+}$  at SBU acts as PS and  $[\text{Mn}(\text{MBA})(\text{CO})_3\text{Br}]$  at SBU acts as CAT for  $\text{CO}_2\text{RR}$ , yielding a selectivity of >99% in CO formation. The control experiments with Zr-MBA-Mn-MOF and Zr-MBA-Ru-MOF separately employed as the photocatalyst showed only trace amounts of a  $\text{CO}_2$  reduction product, supporting the hypothesis that the close proximity between the PS and CAT within the MOF shortens the distances for the transport of charge carriers. Interestingly, the photocatalysis experiments were conducted without an exogenous electron donor, implying that water may be the terminal electron donor. Similar to type II-MOFs, this strategy also enables photocatalytic reactions within the isolated domains of the framework. However, unlike the use of dicarboxylate entities, a monocarboxylate-based entity is employed. This monocarboxylate entity is integrated either by replacing the surface carboxylate molecules attached to the SBU or by substituting one of the SBU-linker coordination. This process reduces the dimensionality and particle size of the MOF, allowing the active components (PS and CAT) to access a greater number of sites at the SBU.<sup>80,81</sup> Moreover, the increased exposure to light, together with these factors, plays a crucial role in heterogeneous photocatalysis, thereby enhancing the overall photocatalytic performance.

**2.1.4. Type IV-MOF, oligonuclear species at SBU or at linker.** Molecularly defined oligonuclear metal complexes containing photocenters bridged to catalytic centers (PS-CAT) can be employed to build MOFs using either the SBU or linker as the binding site (Fig. 5). One recent example is two hexanuclear zirconium ( $\text{Zr}_6$ ) cluster-based MOFs (namely PCN 224 and PCN 222 with different topologies) comprised of Zn-TCP linkage, which have been post-synthetically modified with a molecular  $\text{CO}_2\text{RR}$  catalyst (namely, *fac*- $[\text{Re}^{\text{I}}\text{Br}(\text{CO})_3(\text{qtpy})]$  complex). The anchoring motif in qtpy (qtpy = 4,4':2',2":4,4"-quaterpyridine) uses its terminal pyridine N to coordinate the central motif (Zn) of one or two Zn-TCP linkers, resulting in a self-assembled PS-CAT dyad-like system in both MOFs (Fig. 6d). These hybrid MOFs (namely Re 222, and Re 224) engaged in the photocatalytic  $\text{CO}_2\text{RR}$  under visible light irradiation in the presence of BIH, serving as sacrificial electron donor.<sup>82</sup> The heterogenized dyad in these MOFs yielded a significantly improved TON for solar  $\text{CO}_2$ -to-CO reduction compared to the homogeneous porphyrin-based PS-CAT dyad. Moreover, these hybrid-MOFs delivered an alternative charge carrier separation pathway, which functions in parallel to their

linker-SBU-based charge separation pathways. Therefore, a wavelength-dependent photocatalytic pathway was observed, where a shorter wavelength resulted in localized charge transfers from the excited porphyrin linkers to the  $\text{Zr}_6$  clusters, producing formate. Alternatively, lower energy irradiation was used to activate the CO-selective Re catalysts with exciton migration enabling long-range, delocalized catalysis. Generally, the type IV PS-CAT pair in TCPP-based MOFs coexist with the type II and type I PS/CAT pair, resulting from the periodic assembly of the porphyrin and semiconductive nature of the MOF, which creates multiple photocatalytic channels for redox reaction. The synergy among these photocatalytic channels and the long-range transportation of the charge carrier resulted in a significant decrease in the recombination rate and boosted the overall photocatalytic activity of the MOF. In some specific examples, the dominance of type IV over other types of photocatalytic channels and better product selectivity were observed by (1) choosing a suitable source of light, as discussed above, and (2) utilizing a specific CAT entity in the dyad such as an  $[\text{FeFe}]$  hydrogenase model<sup>83</sup> and  $\text{Pt}(\text{II}), \text{Pd}(\text{II})$ -based single-atom catalysts (SACs).<sup>84-86</sup> Similarly, given the broader potential for creating type IV PS-CAT dyads at the SBU, innovative charge transfer complexes or monocarboxylate-based PSs have been reported,<sup>80,82,87</sup> which can electronically communicate (*via* electron transfer) with the SBU through covalent connections and sensitize pristine light-inactive MOF systems for various photocatalytic reactions (Tables 1-4).

**2.1.5. Type V-MOF, pore-MOF backbone.** This type of photocatalytic system is built with an ideal molecularly defined species as one of the active units, which is either added directly as a homogenous phase to a solid MOF dispersion at the time of photocatalytic reaction or encapsulated in the MOF *via* non-covalent interaction prior to the photocatalytic reaction (Fig. 5). One of the perquisites in type V-MOFs is that the active molecular species must fit into the pore size of the MOF, and therefore the topology and linker length of the MOF play a crucial role in achieving photocatalytic performances. There are many examples of this type of photocatalytic system (see Tables 1-4), where the pristine/covalently functionalized MOF particles serve as the chromophore and the encapsulated/homogenous molecular units act as the catalytic center or *vice versa*, building diverse MOF-supported PS/CAT pairs. In addition, some MOFs only serve as a photo-inactive templating host to encapsulate both the molecular PS and CAT units. One recent example from Stanley and co-workers shows the immobilization of a  $\text{CO}_2\text{RR}$  CAT  $[\text{ReBr}(\text{CO})_3(4,4'\text{-dcbpy})]$  ( $4,4'\text{-dcbpy}$  = 2,2'-bipyridine-4,4'-dicarboxylate) and  $[\text{Ru}(\text{bpy})_2(5,5'\text{-dcbpy})]\text{Cl}_2$  serving as PS onto the isoreticular series of UiO-66, UiO-67, and UiO-68 (Fig. 6e).<sup>88</sup> The pore size determines the anchoring site (inside *vs.* outside), which has a distinct impact on the electronic communication between CAT and PS. This work provided a rational understanding of the host-guest effects, specific anchoring sites and reactive center distance in the photocatalytic  $\text{CO}_2$  reduction (Fig. 5). However, this approach is no longer limited to carboxylate linker-based MOFs, which now includes solution-state PS



**Table 1** Active molecular components (PS-CAT pairs) in MOF-based photocatalysts for the visible light-driven HER

Photocatalytic MOF system	Primary building units		Active molecular components		Cofactors	Type	Ref.
	Linker	SBU	PS	CAT			
Ni <sub>1.5</sub> S/MOF (UiO-66-NH <sub>2</sub> )		Zr <sub>6</sub> -oxo cluster	Linker NH <sub>2</sub> -BDC	Ni(SH)(OH <sub>2</sub> )@SBU	TEA	I	126
Fe-X@Zr <sub>6</sub> -Cu		Zr <sub>6</sub> -oxo cluster		Fe <sup>II</sup> -X@SBU X = Br <sup>-</sup> , Cl <sup>-</sup> , AcO <sup>-</sup> , and BF <sub>4</sub> <sup>-</sup>	BiH	I	71
PT		TPHN		[Cu(Pt)(dppe)] <sup>+</sup>	SBU and H <sub>2</sub> PtCl <sub>6</sub> as a cocatalyst	MeOH or EDTA	122
Ti-MOF-Ru(cptpy) <sub>2</sub>		Ti <sub>8</sub> -oxo cluster		[Ru(cptpy) <sub>2</sub> ] <sup>2+</sup>	Linker TBAPy	BiH	I
Co-NU (N <sub>C</sub> 0.27)				[Ru(cptpy) <sub>2</sub> ] <sup>2+</sup>	Linker TBAPy		125
							[Co(dmgH) <sub>2</sub> (4-COOH-py)Cl] @SBU



Table 1 (Contd.)

Photocatalytic MOF system	Primary building units			Active molecular components		
	Linker	SBU	PS	CAT	TEOA	Cofactors
Ru-TBP-Zn		Ru <sub>2</sub> -Paddle wheel	Linker Zn-TCPP	SBU		I
Zn-TCPP (= Zn-TBP)		Zr <sub>6</sub> -oxo cluster	Linker [Ru(bpydc) <sub>3</sub> ] <sup>2+</sup>		BnOH	I
SYD-1-CuNi						128
Ti <sub>3</sub> -BPDC-Ru or Ti <sub>3</sub> -BPDC-Ir		[Ru(bpydc) <sub>3</sub> ] <sup>2+</sup>	Ti <sub>3</sub> -hydroxo cluster	SBU	BiH	I
	bpydc and 5,5'-dcbpy					118



Table 1 (Contd.)

Photocatalytic MOF system	Primary building units			Active molecular components			Cofactors	Type	Ref.
	Linker	SBU	PS	CAT	SBU and H <sub>2</sub> PtCl <sub>6</sub> cocatalyst	TEOA or ascorbic acid			
Ru-Eu MOF or Ru-Pr MOF		$[\text{Ru}(\text{cptpy})_2]^{2+}$	$\text{Eu or Pr}$	$\text{Linker } [\text{Ru}(\text{cptpy})_2]^{2+}$	$\text{SBU and H}_2\text{PtCl}_6$ cocatalyst	TEOA or ascorbic acid	I	I	121
M-Sas @Pd-PCN-222-NH <sub>2</sub>		$[\text{Ru}(\text{cptpy})_2]^{2+}$	$\text{Hf}_6^{\text{+}}$ oxo cluster	$\text{Linker Pd-TCPP}$	M-single atoms@-NH <sub>2</sub> modified SBU M = Ru, Ir, Pt, Au	Tri-isopropanol amine	I	I	225
In-MOF/Pt		$[\text{Ru}(\text{cptpy})_2]^{2+}$	$\text{Pd-TCPP}$	Decahedron In		TEOA	I	I	226
NML-PtN <sub>x</sub> ( $x = 2, 4$ )		$[\text{Ru}(\text{cptpy})_2]^{2+}$	$\text{L8}$	$\text{Ti}_8^{\text{+}}$ oxo cluster		TEOA	I	I	129
UiO-66-dcadbt-Cd		$[\text{Ru}(\text{cptpy})_2]^{2+}$	$\text{L8}$	$\text{NH}_2\text{-BDC}$		TEOA and Pt NPs cocatalyst	SBU and Pt NPs cocatalyst	SBU [S- Cd-S-]@SBU	227
								$[\text{Cd}(\text{dcdbt})](\text{solv})_2$	



Table 1 (Contd.)

Photocatalytic MOF system	Primary building units			Active molecular components				Cofactors	Type	Ref.
	Linker	SBU	PS	CAT	SBU and Pt NPs	TEOA	I and V			
Pd/Yb-PMOF (2 wt% Pt)	Yb <sub>2</sub> -oxo chain									
UiO-67-Ir-ppy/Co or UiO-67-Ir-Cou 6/Co	CO <sub>2</sub> Pd-TCPP	CO <sub>2</sub> Pd-TCPP	PS	CO <sub>2</sub> Zr <sub>6</sub> -oxo cluster	CO <sub>2</sub> [Ir(ppy) <sub>2</sub> (5,5'-dcbpy)] <sup>+</sup> or [Ir(Cou) <sub>2</sub> (5,5'-dcbpy)] <sup>2+</sup>	CO <sub>2</sub> BIH	CO <sub>2</sub> [Co(5,5'-dcbpy)](NO <sub>3</sub> ) <sub>2</sub>	CO <sub>2</sub> ascorbic acid	II	76
UiO-MOF-Fe <sub>2</sub> S <sub>2</sub>	CO <sub>2</sub> 5,5'-dcbpy	CO <sub>2</sub> Zr <sub>6</sub> -oxo cluster		CO <sub>2</sub> [Ru(bpy) <sub>2</sub> (L <sub>2</sub> )] <sup>2+</sup>	CO <sub>2</sub> [FeFe] hydrogenases@ L <sub>3</sub>	CO <sub>2</sub>	CO <sub>2</sub>	CO <sub>2</sub>	II	77



Table 1 (Contd.)

Photocatalytic MOF system	Primary building units			Active molecular components				Ref.
	Linker	SBU	PS	CAT	BIH	Cofactors	Type	
mPT-Cu/Co		Zr <sub>6</sub> -oxo cluster			EDTA or DMA	II	73 and 74	75
Ru-Pt-UoO-67		Zr <sub>6</sub> -oxo cluster			EDTA or DMA	II	73 and 74	75
Co-Ru-UoO-67(bpy)		Zr <sub>6</sub> -oxo cluster			EDTA or DMA	II	73 and 74	75
HER-MOF		Hf <sub>6</sub> -oxo cluster			EDTA or DMA	II	73 and 74	75
H <sub>2</sub> -TCPP					EDTA or DMA	II	73 and 74	75



Table 1 (Contd.)

Photocatalytic MOF system	Linker	Primary building units		Active molecular components		Cofactors	Type	Ref.
		SBU	PS	CAT				
PtSA-MNSS		$\text{Cu}_2(\text{COO})_4$ paddle-wheel		$\text{CO}_2^-$	$\text{CO}_2^-$	ascorbic acid	II and IV	85
PCN-H <sub>2</sub> /Pt <sub>VV</sub>	Pt-TCPP	Zr <sub>6</sub> -oxo cluster		$\text{CO}_2^-$	$\text{Pt-TCPP/Pt}$ single atom	TEOA	II and IV	131
Al-TCPP-Pt <sub>(II)</sub>	H <sub>2</sub> -TCPP	Al <sub>2</sub> hydroxo cluster		$\text{CO}_2^-$	$\text{Pt-TCPP}$	TEOA	II and IV	132
[FeFe] <sub>2</sub> @ZrPFF	H <sub>2</sub> -TCPP	Zr <sub>6</sub> -oxo cluster		$\text{CO}_2^-$	$\text{Pt-TCPP/Zn-TCPP}$ unit	Linker Zn-TCPP	IV	83
[Fe <sub>2</sub> (CO) <sub>6</sub> ] <sub>2</sub> N(C <sub>5</sub> H <sub>4</sub> N) <sub>2</sub> @linker	Zn-TCPP			$\text{CO}_2^-$	$\text{Pt-TCPP/Pt}$ single atom			



Table 1 (Contd.)

Photocatalytic MOF system	Primary building units			Active molecular components			Cofactors	Type	Ref.
	Linker	SBU	PS	CAT	BIH				
Ce <sub>6</sub> BTB-Ru or Ce <sub>6</sub> BTB-Ir		Ce <sub>6</sub> -oxo cluster		SBU					
							M = Ru, X = N M = Ir, X = C		
							[Ru(bpy) <sub>2</sub> (MBA)] <sup>2+</sup> @ SBU or [Ir(ppy) <sub>2</sub> (MBA)] <sup>+</sup> @ SBU and Ce <sup>3+</sup> (SBU)		
Pd-MOF		Cu <sub>2</sub> paddlewheel					Ascorbic acid	IV	84
Co@NH <sub>2</sub> -MIL-125(Ti)		Pd-TCPP		Pd-TCPP			Triethyl- amine	V	135
NH <sub>2</sub> -BDC		Ti <sub>8</sub> -oxo cluster		NH <sub>2</sub> -MIL-125(Ti) MOF					
ZrTTA-6SH-MTFPP		Zr <sub>6</sub> -oxo cluster		ZrTTA-6SH MOF			TEOA	V	229
TTA-6SH									
							M = Zn, Ni, FeCl M-TFPP and H <sub>2</sub> PtCl <sub>6</sub> cocatalyst		



Table 1 (Contd.)

Photocatalytic MOF system	Primary building units			Active molecular components			Cofactors	Type	Ref.
	Linker	SBU	PS	CAT	Tri-methyl-amine	V			
Zn-PDTP/[Co(bpy) <sub>3</sub> ]Cl <sub>2</sub>	Zn <sub>2</sub> cluster	Zn-PDTP MOF							230
	[Co(bpy) <sub>3</sub> ]Cl <sub>2</sub>								
Gd-TCA MOF + [FeFe]-H <sub>2</sub> ase or [Co(bpy) <sub>3</sub> ]Cl <sub>2</sub>	PD and TP CO <sub>2</sub> TCA	Gd-O pillar	Gd-TCA MOF		[N'Pr <sub>2</sub> EtH] [OAc]	V	139		
Co(II)@MIL-125-NH <sub>2</sub>	CO <sub>2</sub> NH <sub>2</sub> -BDC	Ti <sub>8</sub> oxo cluster	MIL-125-NH <sub>2</sub> MOF		[FeFe]-H <sub>2</sub> ase or [Co(bpy) <sub>3</sub> ] <sup>2+</sup>	TEOA	V	136	
Ni <sub>4</sub> P <sub>2</sub> @MOF	Zr <sub>6</sub> oxo cluster				[Co(TPA)Cl]Cl [Ni <sub>4</sub> (H <sub>2</sub> O) <sub>2</sub> (PW <sub>9</sub> O <sub>34</sub> ) <sub>2</sub> ] <sup>110-</sup> (POM)	MeOH	V	231	
	L2				[Ir(ppy) <sub>2</sub> (L2)] <sup>+</sup>				



Table 1 (Contd.)

Photocatalytic MOF system	Primary building units		Active molecular components				Cofactors	Type	Ref.
	Linker	PS	SBU	CAT	TEOA	V			
UiO-66-dcbd-M + $[\text{Ru}(\text{bpy})_3]^{2+}$		Zr <sub>6</sub> -oxo cluster			TEOA	V	232		
$[\text{Ru}_2(p\text{-BDC})_2]_n + \text{Ru}(\text{bpy})_3^{2+}$		Ru <sub>2</sub> paddlewheel			EDTA	V	233 and 234		
UiO-66-[FeFe]dcbd + $[\text{Ru}(\text{bpy})_3]^{2+}$		Zr <sub>6</sub> -oxo cluster			Ascorbic acid	V	142		
RuCl@UiO or RuOH <sub>2</sub> @UiO or RhCl@UiO or RhOH <sub>2</sub> @UiO + $[\text{Ru}(\text{bpy})_3]^{2+}$		bpd and 5,5'-dcbpy			DMA or TEOA	V	156		
MIL-101-CH <sub>2</sub> @1 + Eosin-Y		BDC			TEOA	V	219		



Table 1 (Contd.)

Photocatalytic MOF system	Primary building units			Active molecular components					Ref.
	Linker	SBU	PS	CAT	Colloidal Pt	EDTA	V	Type	
Al-PMOF/Pt		Al <sub>2</sub> hydroxo cluster	Al-PMOF (H <sub>2</sub> -TCPP)					Cofactors	
Pt@Pd-PMOF-2(Hf)		Hf <sub>6</sub> -oxo cluster						TEOA	V
Pt/fluorinated MOF(Cu)-NH <sub>2</sub> + RhB								EtOH	V
L9		Cu <sub>2</sub> -paddlewheel						Pt NPs	237
TP-EYTP + [Co(bpy) <sub>3</sub> ]Cl <sub>2</sub>		Zn <sub>2</sub> cluster						TEA	V
Zn-TTPy/PtNPs		TP and Eosin Y	Zn <sub>4</sub> chain					TEOA	222
			TTPy						

Table 1 (Contd.)

Photocatalytic MOF system	Linker	Primary building units	Active molecular components						
			SBU	PS	CAT	EDTA	Cofactors	Type	Ref.
Ru@dpdhpz/BASF-A520 + MV/ Pt NPs		Al octahedral chain		Pt NPs				V	138
Zr/Cu-(H <sub>2</sub> BDC-BPD) + Eosin Y		Cu <sub>2</sub> paddlewheel		Zr-O <sub>x</sub> @SBU	TEOA	V		V	140
M-dcbbdt + [Ru(bpy) <sub>3</sub> ] <sup>2+</sup>		[MS <sub>4</sub> ] <sup>-</sup> and octahedral M							91
Mn-TBAPy-NT/Pt NPs				Pt NPs					238
HHTHATN-Ni-Pt-NS + [Ru(bpy) <sub>3</sub> ] <sup>2+</sup>		TBAPy <sup>4+</sup>		-[NiS <sub>4</sub> ] <sup>-</sup> -square-planar	Ascorbic acid	V		V	141
HHTHATN					DMA				

**Table 2** Active molecular components (PS-CAT pairs) in MOF-based photocatalysts for the visible light-driven  $\text{CO}_2$ RR

Photocatalytic MOF system	Primary building units		Active molecular components				Cofactors	Type	Ref.
	Linker	SBU	PS	CAT	SBU	TEOA			
Eu-Ru(phen) <sub>3</sub> -MOF		Eu <sub>2</sub> -cluster	Linker: [Ru(1,4)] <sup>2+</sup>						94
Cu-PMOF or Co-PMOF				Cu <sub>2</sub> paddle wheel or Cu <sub>3</sub> hydroxo cluster	Linker: M-TCPP (M = Cu or Co)	SBU	TEOA	I	239
MAF-34-CoRu				M = Co, Cu	Co-imidazolate tetrahedra [Co(ip) <sub>4</sub> ] <sup>2-</sup>		H <sub>2</sub> O	I	240
							[Co(ip) <sub>4</sub> ] <sup>2-</sup>		



Table 2 (Contd.)

Photocatalytic MOF system	Primary building units		Active molecular components				Cofactors	Type	Ref.
	Linker	SBU	PS	CAT	BnOH				
SYD-1-CuNi		Zr <sub>6</sub> -oxo cluster	Linker [Ru(L1) <sub>3</sub> ] <sup>2+</sup>				BnOH	I	128
Re-NU (NC 0.46)		Zr <sub>6</sub> -oxo cluster	Linker: TBAPy <sup>4-</sup>				BH	I	125
FDH@Rh-NU-1006		Zr <sub>6</sub> -oxo cluster	Linker: ptba				TEOA	I	111
Hf <sub>12</sub> -Ru-Re or Hf <sub>12</sub> -Ru-Mn	ptba	Hf <sub>12</sub> -oxo cluster	Linker: [Ru(bpy) <sub>2</sub> (L2)] <sup>2+</sup>				BH or BNAH	I	153

[Rh (Cp\*)(5,5'-dcbpyH)Cl]  
@SBU

for NAD reduction followed  
by FDH enzyme for CO<sub>2</sub>RR

[M(MBA)(CO)<sub>3</sub>X]  
@SBU

Table 2 (Contd.)

Photocatalytic MOF system	Primary building units				Active molecular components				Cofactors	Type	Ref.			
	Linker	SBU		PS	CAT		Linker: H <sub>2</sub> O	Linker: TEOA						
		Linker: Zn-ZTCPP	Linker: TBAPy <sup>4+</sup>		Linker: H <sub>2</sub> O	Linker: TEOA								
PMOF/Re				[Re(4,4'-dcbpy)(CO) <sub>3</sub> Cl] @SBU					BIH	I	241			
TCP(Co)CN-1000				Zr <sub>6</sub> -oxo cluster	Linker: TBAPy <sup>4+</sup>					I	242			
Cu-ZnTCPP/g-C <sub>3</sub> N <sub>4</sub> hybrid				TBAPy <sup>4+</sup>					Co-TCPP@SBU	I	243			
Bi-PMOFs									SBU	I	244			
H <sub>2</sub> -TCPP									TEOA	I				



Table 2 (Contd.)

Photocatalytic MOF system	Primary building units		Active molecular components				Cofactors	Type	Ref.
	Linker	SBU	PS	CAT	SBU				
UiO-67- <i>o</i> -(CH <sub>3</sub> ) <sub>2</sub>		Zr <sub>6</sub> -oxo cluster					H <sub>2</sub> O	I	66
UiO-67- <i>o</i> -CF <sub>3</sub> -CH <sub>3</sub>									
UiO-67- <i>o</i> -(CF <sub>3</sub> ) <sub>2</sub>							TEOA	I	181
SC-Bi-PMOFs		Bi <sub>2</sub> -oxo cluster					SBU	TEOA	I
Zr-Co MOF@TBAPy									245
GDUT-8 ( <i>n</i> = 1)		Zr <sub>6</sub> -oxo cluster					SBU	TEOA	I
GDUT-8-Ox ( <i>n</i> = 2)									
Fe-DBP(Co)									
					<img				



Table 2 (Contd.)

Photocatalytic MOF system	Primary building units		Active molecular components				Cofactors	Type	Ref.
	Linker	SBU	PS	CAT	SBU				
DGIST-1		Ti-oxo chain				TEOA	I		224
Ti-MOF		H2-TCPP				TEOA	I		247
mPT-Cu/Re		Tp-PABA				BiH	II		75
PT		TPHN				[Re(PT)(dppe)]+			



Table 2 (Contd.)

Photocatalytic MOF system	Primary building units			Active molecular components			Cofactors	Type	Ref.
	Linker	SBU	PS	CAT	BIH	II			
UiO-67-Ir-bpy/Cu or UiO-67-Ir-Cou 6/Cu		Zr <sub>6</sub> -oxo cluster			TIPB	II	248	[Cu(5,5'-dcbpy)Cl <sub>2</sub> ]	76
Eu-bpy-Ru-x%-CuClIX		Eu <sub>6</sub> -oxo cluster			TIPB	II	248	[Ir(Cou6)2(5,5'-dcbpy)] <sup>+</sup>	249
(Co/Ru) <sub>n</sub> -UiO-67 (bpydc)		Zr <sub>6</sub> -oxo cluster			TEOA	II	249	[Co(5,5'-dcbpy)(THF) <sub>2</sub> ] <sup>2+</sup>	249



Table 2 (Contd.)

Photocatalytic MOF system	Primary building units			Active molecular components			Cofactors	Type	Ref.
	Linker	SBU	PS	CAT	BIH	II			
MOF-253-Ir/Ni		Al-hydroxo cluster							250
MOF-1		Zr <sub>6</sub> oxo cluster					TEA	II with similar scaffold	251
MOF-4		Zr <sub>6</sub> oxo cluster					TEA		189
Re-MOF-NH <sub>2</sub>		Zr <sub>6</sub> oxo cluster					TEA		150



Table 2 (Contd.)

Photocatalytic MOF system	Primary building units			Active molecular components			Cofactors	Type	Ref.
	Linker	SBU	PS	CAT					
MOF-253-Ru(CO) <sub>2</sub> Cl <sub>2</sub> or Sensitized MOF-253-Ru(CO) <sub>2</sub> Cl <sub>2</sub>		Al-hydroxo cluster			CO <sub>2</sub> <sup>·</sup>	TEOA	II with similar or dissimilar scaffold	252	
					[Ru(5,5'-dcbpy)(CO) <sub>2</sub> Cl <sub>2</sub> ]				
S <sub>Cu</sub> : Cu@Al-PMOF		Al <sub>2</sub> -hydroxo cluster			CO <sub>2</sub> <sup>·</sup>	TEA	II and IV	253	
					[Ru(bipy) <sub>2</sub> (5,5'-dcbpy)] <sup>2+</sup>				
					CO <sub>2</sub> <sup>·</sup>				
MOF-525-Co		Zr <sub>6</sub> -oxo cluster			CO <sub>2</sub> <sup>·</sup>	TEOA	II and IV	254	
					CO <sub>2</sub> <sup>·</sup>				
					CO <sub>2</sub> <sup>·</sup>				
					CO <sub>2</sub> <sup>·</sup>				
					CO <sub>2</sub> <sup>·</sup>				
					CO <sub>2</sub> <sup>·</sup>				
					CO <sub>2</sub> <sup>·</sup>				

Table 2 (Contd.)

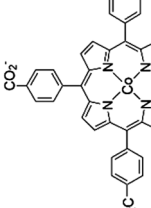
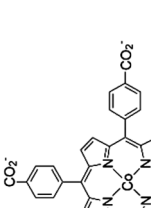
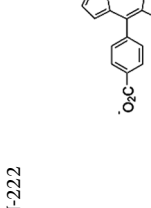
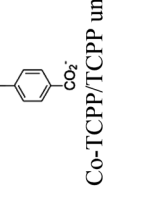
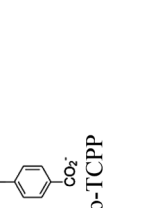
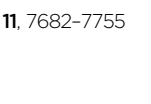
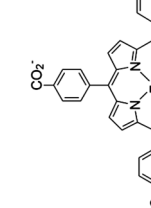
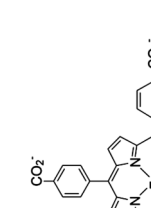
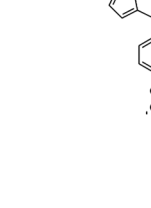
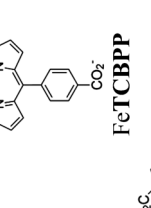
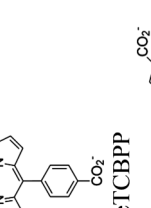
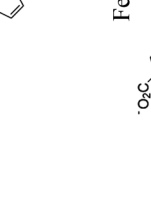
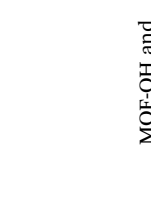
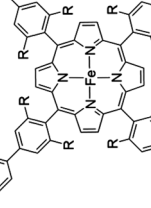
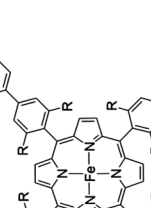
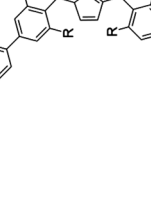
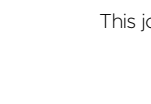
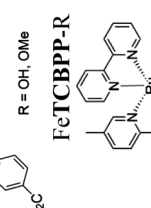
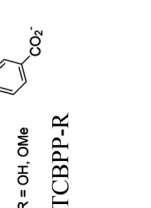
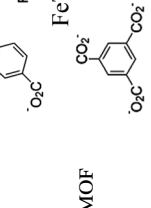
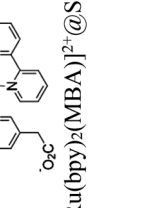
Photocatalytic MOF system	Primary building units		Active molecular components				Cofactors	Type	Ref.
	Linker	SBU	PS	CAT	TEA	II and IV			
$(\text{Cu}_x\text{Pd}_y)_z@\text{PCN-222}_{(\text{Co})}$							255		
Co-TCPP							256		
MOF-526-H							257		
MOF-OH and MOF-OCH <sub>3</sub>									
Zr-MBA-Ru/Re-MOF							81		
							81		
							81		



Table 2 (Contd.)

Photocatalytic MOF system	Primary building units			Active molecular components			Cofactors	Type	Ref.
	Linker	SBU	PS	CAT					
Zr-MBA-Ru/Mn-MOF		Zr <sub>6</sub> -oxo cluster			H <sub>2</sub> O	III	79		
ReRu66NH <sub>2</sub>		Zr <sub>6</sub> -oxo cluster			[Mn(MBA)(CO)3Br] @SBU	III	258		
NH <sub>2</sub> -BDC					[Re(4,4'-dcbpy)(CO)3 Br] @SBU				
Rh-Ru@UiO-66		Zr <sub>6</sub> -oxo cluster			[Rh(Cp*)(4,4'-dcbpy)Cl] <sup>+</sup> @SBU	III	159		
Re-Ru@U (U = UiO-66)		Zr <sub>6</sub> -oxo cluster			[Rh(Cp*)(4,4'-dcbpy)Cl] <sup>+</sup> @SBU	III	148		
RhB@Zr-MOF		Zr <sub>6</sub> -oxo cluster			RhB	IV	259		



Table 2 (Contd.)

Photocatalytic MOF system	Primary building units			Active molecular components			Cofactors	Type	Ref.
	Linker	SBU	PS	CAT					
Cu@808-NH <sub>2</sub> IPA-NO <sub>2</sub>		Zr <sub>6</sub> -oxo cluster			Ascorbic acid	IV	260		
Re-224 or Re-222		Zr <sub>6</sub> -oxo cluster			Cu(II)-Schiff base complex	IV	82		
UiO-66-CrCAT		Zr <sub>6</sub> -oxo cluster			[ReBr(qipy)(CO)3Br]@Zn-TCPP linker				
GaCAT		Zr <sub>6</sub> -oxo cluster			catbdc with Cr (LMCT)	IV and TEOA	261		
g-CNQDs/PMOF hybrids (2D)		Co <sub>2</sub> paddle wheel			Co-TCPP and carbon nitride quantum dots (g-CNQDs)	IV and V	262		
Ni-74-Am <sup>+</sup>		Ni <sub>2</sub> cluster			[Ru(bpy) <sub>3</sub> ] <sup>2+</sup>	TEOA	263		
[Ru(bpy) <sub>3</sub> ] <sup>2+</sup>		DHBDC				SBU			



Table 2 (Contd.)

Photocatalytic MOF system	Primary building units			Active molecular components			Cofactors	Type	Ref.
	Linker	SBU	PS	CAT					
$[\text{Ru}(\text{bpy})_3]^{2+} + (\text{PW}_{12}, \text{Cp}^*\text{Rh})@\text{UiO-67}$	$\text{CO}_2^-$ 	Zr <sub>6</sub> -oxo cluster		$\text{CO}_2^-$ 	$[\text{Rh}(\text{Cp}^*)(5,5'\text{-dcbpy})\text{Cl}]^{2+}$ and electron relay: $[\text{PW}_{12}\text{O}_{40}]^{n-} @ \text{SBU}$	TEOA	V	158 and 207	
$[\text{Ru}(\text{dmbpy})_3]^{2+} + \text{UiO-67-Mn}(\text{bpy})(\text{CO})_3\text{Br}$	$\text{CO}_2^-$ 	Zr <sub>6</sub> -oxo cluster		$\text{CO}_2^-$ 	$[\text{Mn}(5,5'\text{-dcbpy})(\text{CO})_3\text{Br}]^{2+}$	BNAH	V	154	
$[\text{Ru}(\text{bpy})_3]^{2+} + \text{Cp}^*\text{Rh}@\text{UiO-67}$	$\text{CO}_2^-$ 	Zr <sub>6</sub> -oxo cluster		$\text{CO}_2^-$ 	$[\text{Rh}(\text{Cp}^*)(5,5'\text{-dcbpy})\text{Cl}]^{2+}$	TEOA	V	157	
$[\text{Ru}(\text{bpy})_3]^{2+} + \text{Co-UiO-67}$ or $\text{Re-UiO-67}$	$\text{CO}_2^-$ 	Zr <sub>6</sub> -oxo cluster		$\text{CO}_2^-$ 	$[\text{Rh}(\text{Cp}^*)(5,5'\text{-dcbpy})\text{Cl}]^{2+}$ or $[\text{Co}(5,5'\text{-dcbpy})\text{Cl}_2]$ or $[\text{Re}(5,5'\text{-dcbpy})(\text{CO})_3\text{Cl}]^{2+}$	TEOA	V	264	



Table 2 (Contd.)

Photocatalytic MOF system	Primary building units			Active molecular components			Cofactors	Type	Ref.
	Linker	SBU	PS	CAT					
$[\text{Ru}(\text{bpy})_3]^{2+} + \text{UiO-}\text{Co-N}_x$		$\text{CO}_2^-$	$[\text{Ru}(\text{bpy})_3]^{2+}$	Zr <sub>6</sub> -oxo cluster			BIH	V	265
$[\text{Ru}(\text{bpy})_3]^{2+} + \text{UiO-}\text{Co-N}_x$		$\text{CO}_2^-$	$[\text{Ru}(\text{bpy})_3]^{2+}$				BIH	V	265
$[\text{Ru}(\text{bpy})_3]^{2+} + \text{MOF-808 CuNi}$		$\text{CO}_2^-$	$[\text{Ru}(\text{bpy})_3]^{2+}$	Zr <sub>6</sub> -oxo cluster			TEOA	V	266
$[\text{Ru}(\text{bpy})_3]^{2+} + \text{Zr-bpdc/}\text{RuCO}$		$\text{CO}_2^-$	$[\text{Ru}(\text{bpy})_3]^{2+}$	Zr <sub>6</sub> -oxo cluster			TEOA	V	267
$[\text{Ru}(\text{bpy})_3]^{2+} + \text{Zr-bpdc/}\text{RuCO}$		$\text{CO}_2^-$	$[\text{Ru}(\text{bpy})_3]^{2+}$	Zr <sub>6</sub> -oxo cluster			TEOA	V	267
$[\text{Ru}(\text{bpy})_3]^{2+} + \text{MX@UiO}$ M: Ru or Rh X: H <sub>2</sub> O or Cl		$\text{CO}_2^-$	$[\text{Ru}(\text{bpy})_3]^{2+}$				TEOA or DMA	V	156
$[\text{Ru}(\text{bpy})_3]^{2+} + \text{MX@UiO}$ M: Ru or Rh X: H <sub>2</sub> O or Cl		$\text{CO}_2^-$	$[\text{Ru}(\text{bpy})_3]^{2+}$				TEOA or DMA	V	156
$[\text{Ru}(\text{bpy})_3]^{2+} + \text{MX@UiO}$ M: Ru or Rh X: H <sub>2</sub> O or Cl		$\text{CO}_2^-$	$[\text{Ru}(\text{bpy})_3]^{2+}$				TEOA or DMA	V	156
$[\text{Ru}(\text{bpy})_3]^{2+} + \text{BPDC}$		$\text{CO}_2^-$	$[\text{Ru}(\text{bpy})_3]^{2+}$				TEOA or DMA	V	156
$[\text{Ru}(\text{bpy})_3]^{2+} + \text{BPDC}$		$\text{CO}_2^-$	$[\text{Ru}(\text{bpy})_3]^{2+}$				TEOA or DMA	V	156
$[\text{Ru}(\text{bpy})_3]^{2+} + \text{BPDC}$		$\text{CO}_2^-$	$[\text{Ru}(\text{bpy})_3]^{2+}$				TEOA or DMA	V	156
$[\text{Ru}(\text{bpy})_3]^{2+} + \text{BPDC}$		$\text{CO}_2^-$	$[\text{Ru}(\text{bpy})_3]^{2+}$				TEOA or DMA	V	156
$[\text{Ru}(\text{bpy})_3]^{2+} + \text{BPDC}$		$\text{CO}_2^-$	$[\text{Ru}(\text{bpy})_3]^{2+}$				TEOA or DMA	V	156
$[\text{Ru}(\text{bpy})_3]^{2+} + \text{BPDC}$		$\text{CO}_2^-$	$[\text{Ru}(\text{bpy})_3]^{2+}$				TEOA or DMA	V	156
$[\text{Ru}(\text{bpy})_3]^{2+} + \text{BPDC}$		$\text{CO}_2^-$	$[\text{Ru}(\text{bpy})_3]^{2+}$				TEOA or DMA	V	156
$[\text{Ru}(\text{bpy})_3]^{2+} + \text{BPDC}$		$\text{CO}_2^-$	$[\text{Ru}(\text{bpy})_3]^{2+}$				TEOA or DMA	V	156
$[\text{Ru}(\text{bpy})_3]^{2+} + \text{BPDC}$		$\text{CO}_2^-$	$[\text{Ru}(\text{bpy})_3]^{2+}$				TEOA or DMA	V	156
$[\text{Ru}(\text{bpy})_3]^{2+} + \text{BPDC}$		$\text{CO}_2^-$	$[\text{Ru}(\text{bpy})_3]^{2+}$				TEOA or DMA	V	156
$[\text{Ru}(\text{bpy})_3]^{2+} + \text{BPDC}$		$\text{CO}_2^-$	$[\text{Ru}(\text{bpy})_3]^{2+}$				TEOA or DMA	V	156
$[\text{Ru}(\text{bpy})_3]^{2+} + \text{BPDC}$		$\text{CO}_2^-$	$[\text{Ru}(\text{bpy})_3]^{2+}$				TEOA or DMA	V	156
$[\text{Ru}(\text{bpy})_3]^{2+} + \text{BPDC}$		$\text{CO}_2^-$	$[\text{Ru}(\text{bpy})_3]^{2+}$				TEOA or DMA	V	156
$[\text{Ru}(\text{bpy})_3]^{2+} + \text{BPDC}$		$\text{CO}_2^-$	$[\text{Ru}(\text{bpy})_3]^{2+}$				TEOA or DMA	V	156
$[\text{Ru}(\text{bpy})_3]^{2+} + \text{BPDC}$		$\text{CO}_2^-$	$[\text{Ru}(\text{bpy})_3]^{2+}$				TEOA or DMA	V	156
$[\text{Ru}(\text{bpy})_3]^{2+} + \text{BPDC}$		$\text{CO}_2^-$	$[\text{Ru}(\text{bpy})_3]^{2+}$				TEOA or DMA	V	156
$[\text{Ru}(\text{bpy})_3]^{2+} + \text{BPDC}$		$\text{CO}_2^-$	$[\text{Ru}(\text{bpy})_3]^{2+}$				TEOA or DMA	V	156
$[\text{Ru}(\text{bpy})_3]^{2+} + \text{BPDC}$		$\text{CO}_2^-$	$[\text{Ru}(\text{bpy})_3]^{2+}$				TEOA or DMA	V	156
$[\text{Ru}(\text{bpy})_3]^{2+} + \text{BPDC}$		$\text{CO}_2^-$	$[\text{Ru}(\text{bpy})_3]^{2+}$				TEOA or DMA	V	156
$[\text{Ru}(\text{bpy})_3]^{2+} + \text{BPDC}$		$\text{CO}_2^-$	$[\text{Ru}(\text{bpy})_3]^{2+}$				TEOA or DMA	V	156
$[\text{Ru}(\text{bpy})_3]^{2+} + \text{BPDC}$		$\text{CO}_2^-$	$[\text{Ru}(\text{bpy})_3]^{2+}$				TEOA or DMA	V	156
$[\text{Ru}(\text{bpy})_3]^{2+} + \text{BPDC}$		$\text{CO}_2^-$	$[\text{Ru}(\text{bpy})_3]^{2+}$				TEOA or DMA	V	156
$[\text{Ru}(\text{bpy})_3]^{2+} + \text{BPDC}$		$\text{CO}_2^-$	$[\text{Ru}(\text{bpy})_3]^{2+}$				TEOA or DMA	V	156
$[\text{Ru}(\text{bpy})_3]^{2+} + \text{BPDC}$		$\text{CO}_2^-$	$[\text{Ru}(\text{bpy})_3]^{2+}$				TEOA or DMA	V	156
$[\text{Ru}(\text{bpy})_3]^{2+} + \text{BPDC}$		$\text{CO}_2^-$	$[\text{Ru}(\text{bpy})_3]^{2+}$				TEOA or DMA	V	156
$[\text{Ru}(\text{bpy})_3]^{2+} + \text{BPDC}$		$\text{CO}_2^-$	$[\text{Ru}(\text{bpy})_3]^{2+}$				TEOA or DMA	V	156
$[\text{Ru}(\text{bpy})_3]^{2+} + \text{BPDC}$		$\text{CO}_2^-$	$[\text{Ru}(\text{bpy})_3]^{2+}$				TEOA or DMA	V	156
$[\text{Ru}(\text{bpy})_3]^{2+} + \text{BPDC}$		$\text{CO}_2^-$	$[\text{Ru}(\text{bpy})_3]^{2+}$				TEOA or DMA	V	156
$[\text{Ru}(\text{bpy})_3]^{2+} + \text{BPDC}$		$\text{CO}_2^-$	$[\text{Ru}(\text{bpy})_3]^{2+}$				TEOA or DMA	V	156
$[\text{Ru}(\text{bpy})_3]^{2+} + \text{BPDC}$		$\text{CO}_2^-$	$[\text{Ru}(\text{bpy})_3]^{2+}$		<img alt="Chemical structure of the active molecular component, a Ru(II) complex with				



Table 2 (Contd.)

Photocatalytic MOF system	Primary building units	Active molecular components						Cofactors	Type	Ref.
		Linker	SBU	PS	CAT	SBU	PS			
$[\text{Ru}(\text{bpy})_3]^{2+} + \text{Co-ZIF-9}$	bIm		Co imidazolate tetrahedra $[\text{Co}(\text{bIm})_4]^{2-}$					TEOA	V	268
$[\text{Ru}(\text{bpy})_3]^{2+} + \text{Ni MOFs (2D)}$	BDC		$[\text{Ni}_2 \text{ hydroxo cluster}]^{2+}$					TEOA	V	269
$[\text{Ru}(\text{bpy})_3]^{2+} + \text{ZIF-67}$	$(\text{Co})$		2-MIM <sup>-</sup>					TEOA	V	90
$[\text{Ag} \square \text{Re}_3\text{-MOF}$			$\text{Zr}_6\text{-oxo cluster}$					TEA	V	270
$\text{Zn MOF} + \text{Cobalt complex}$								$[\text{Re} (5,5'\text{-dcbpy})(\text{CO})_3\text{Cl}]$	V	271
$\text{Gd-TCA MOF} + \text{Ni} (\text{Cyclam})\text{Cl}_2$								TEA	V	139

Table 2 (Contd.)

Photocatalytic MOF system	Primary building units			Active molecular components			Cofactors	Type	Ref.
	Linker	SBU	PS	CAT					
Re-Ru@MIL		Al <sub>3</sub> -Oxo cluster					TEOA, BIH, BNAH, DMA, KEX, TEA TPP	V	149 and 272
Ru and Re@UiO-66, 67, 68 (-NH <sub>2</sub> )		Zr <sub>6</sub> -Oxo cluster					TEOA	V	88
LTG-FeZr + Eosin Y		Zr-carboxylate octahedra					TEOA	V	273
66-IS-M, M = Ni, Co, Cu + [Ru(bpy) <sub>3</sub> ] <sup>2+</sup>		Zr <sub>6</sub> -Oxo cluster					TEOA	V	274
									Isatin-Schiff base complex

Table 2 (Contd.)



Table 2 (Contd.)

Photocatalytic MOF system	Primary building units	Active molecular components				Cofactors	Type	Ref.
		Linker	SBU	PS	CAT			
Ru-MOF			No specified catalytic site	TEOA	NA	277		
MOF-808-PBA-MV				BNAH	NA	151		

such as  $[\text{Ru}(\text{bpy})_3]^{2+}$  to unlock the SBU of non-carboxylate linker-based MOFs. This includes the  $\text{Co}_8$ -hydroxo cluster in metal azolate frameworks (MAFs)<sup>89</sup> and Co-imidazolate tetrahedra  $[\text{Co}(2\text{-MIM})_4]^{2-}$  in zeolitic imidazolate frameworks (ZIFs).<sup>90</sup> The former demonstrates water oxidation reactions (OER) in the presence of  $\text{Na}_2\text{S}_2\text{O}_8$ , while the latter is effective in catalyzing  $\text{CO}_2$  reduction reactions ( $\text{CO}_2\text{RR}$ ) in the presence of TEOA. Recently, a new butterfly-shaped metal-bis(dithiolene) linker was developed, forming 2D metal-organic frameworks (M-dcbdt, where M = Ni, Co, or Fe). The  $[\text{Ru}(\text{bpy})_3]^{2+}$  with an  $[\text{MS}_4]$ -rich network was established as a promising pair for the hydrogen evolution reaction (HER).<sup>91</sup>

### 3. Techniques for mechanistic elucidations

Besides the development of techniques to address the challenge of size distribution, crystallographic properties, and porosities of MOF-based nanoparticles (NPs),<sup>92,93</sup> the understanding of the elementary electron transfer steps originating from the photoexcited states is essential in the context of catalysis and artificial photosynthesis. A mechanistic understanding allows the rational optimization for improved catalytic output and in the best-case scenario (i) all incident photons get absorbed by PS and (ii) the resulting excited states undergo electron transfer steps with CATs and sacrificial reagents with unity quantum yield. Furthermore, (iii) there are no unproductive charge recombination events, and thus charge separation is solely used for catalytic turnover. However, this is not usually the case, and therefore it is crucial to understand the deviation in the real behavior of MOF-based systems from the above-mentioned best-case scenario, *i.e.*, the extent to which non-productive events occur in each step. However, it should also be noted that due to the large size of MOF NPs and their aggregates (often  $>100$  nm), the typically applied optical techniques suffer from strong light scattering, making the acquired data difficult to interpret.<sup>94</sup> Thus, during the preparation of samples for optical spectroscopy and evaluating “molecular” PS and CAT inside the MOF scaffold, special care must be taken and a specific/an appropriate technique must be used to collect meaningful data.<sup>95</sup> One of the numerous advantages of MOF-based photocatalysts over their homogeneous, freely diffusing molecular counterparts is the close spatial proximity of PS, CAT, and (sometimes) sacrificial reagents by design. This increases their local concentration, and consequently the efficiency of the desired electron transfer, minimizing unproductive diffusion processes. Proximity is not only realized by attaching PS and CAT to the MOF skeleton, *e.g.*, *via* carboxylated linker systems, but can also be generated by the high porosity of the MOF itself. Pore trapping of one or several of the necessary components (also see type V in Fig. 5), *i.e.*, host-guest interactions, can experimentally be followed by techniques such as IR spectroscopy, Raman spectroscopy,<sup>96</sup> resonance Raman<sup>97</sup> and (solid-state, ss) NMR spectroscopy<sup>98</sup> but also optical techniques such as steady-state UV-vis spec-

**Table 3** Active molecular components (PS-CAT pairs) in MOF-based photocatalyst for the visible light-driven OER

Photocatalytic MOF system	Primary building units		Active molecular components				Ref.
	Linker	SBU	PS	CAT	Cofactors	Type	
WOR-MOF		Zr <sub>12</sub> -oxo cluster			Fe <sup>3+</sup>	II	278
P <sub>2</sub> W <sub>18</sub> Co <sub>4</sub> POM@MOF-545		Zr <sub>6</sub> -oxo cluster			[Ir (5,5'-dcbpy)] <sup>3+</sup> [(PW <sub>9</sub> O <sub>34</sub> ) <sub>2</sub> Co <sub>4</sub> (H <sub>2</sub> O) <sub>2</sub> ] <sup>10-</sup>	Na <sub>2</sub> S <sub>2</sub> O <sub>8</sub>	V
		H <sub>2</sub> -TCPP			Fe <sub>3</sub> -oxo cluster	Na <sub>2</sub> S <sub>2</sub> O <sub>8</sub>	164
		H <sub>2</sub> -TCPP			Co <sub>8</sub> -hydroxo cluster	Na <sub>2</sub> S <sub>2</sub> O <sub>8</sub>	V
		H <sub>2</sub> -TCPP			Co <sub>2</sub> Ti	Na <sub>2</sub> S <sub>2</sub> O <sub>8</sub>	V
		H <sub>2</sub> -TCPP			ABTC	Na <sub>2</sub> S <sub>2</sub> O <sub>8</sub>	V
		H <sub>2</sub> -TCPP			[Ru(bpy) <sub>3</sub> ] <sup>2+</sup>	[Ru(bpy) <sub>3</sub> ] <sup>2+</sup>	166
		H <sub>2</sub> -TCPP			Ti sites @SBU	[Ru(bpy) <sub>3</sub> ] <sup>2+</sup>	165



Table 3 (Contd.)

Photocatalytic MOF system	Primary building units		Active molecular components			Cofactors	Type	Ref.
	Linker	SBU	CAT	PS				
CoBIM-1 + $[\text{Ru}(\text{bpy})_3]^{2+}$						$\text{Na}_2\text{S}_2\text{O}_8$	V	89

troscopy.<sup>88</sup> In contrast to crystallographic methods, which typically address long-range effects such as crystallinity, phase identification, topology and 3D structure, IR, Raman and ssNMR spectroscopy allow the local environments of the MOF to be probed, which are important for efficient electron transfer cascades induced by visible light.

### 3.1. Tools to study photon capture

Photocatalysis-inducing light absorption in MOFs can be probed by steady-state UV-vis absorption spectroscopy. However, in contrast to molecular systems, which are often completely soluble in one or several suitable solvents, MOFs are not. Thus, their optical properties are often determined in the solid state using diffuse reflectance spectroscopy (DRS) rather than in the liquid state, where diluted solutions and classical cuvettes can be used for molecular systems.<sup>96</sup> However, some solution-state UV-vis measurements provided an interpretable result for MOF particles possessing a size of less than 100 nm and formed a stable colloidal solution when dispersed in a solvent.<sup>95</sup> After DRS data treatment with the Kubelka–Munk function and/or from solution-state UV-vis data, a comparison between an MOF and its soluble molecular analogue is possible. Generally, the absorption properties of the PS component as observed in the homogenous state can be either retained or changed in an integrated-MOF platform and varies from case to case. For example, the  $\text{NH}_2$ -BDC linker connected to a Ce(IV)-based SBU produced a new LMCT band in the  $\text{UiO-66}(\text{Ce})\text{-NH}_2$  MOF, while the same linker retained its ligand-centered absorption (LC) band in Zr(IV)-based  $\text{UiO-66}(\text{Zr})\text{-NH}_2$  MOF.<sup>54</sup> Additionally, density functional theory (DFT) calculation is commonly used to theoretically interpret these absorption features by estimating the band gap, and relative orbital contribution of the components (metal and linker) at the HOCO (VB) and LUCO (CB) level of the semiconductive MOF.<sup>54,55,99</sup> In contrast, upon the incorporation of a metalloligand-based PS such as  $[\text{Ru}(\text{bpy})_2(5,5'\text{-dcbpy})]^{2+}$  (ref. 100) and  $[\text{Cu}(\text{PT})(\text{dppe})]^{+}$  (ref. 75) into the MOF scaffold, their UV-vis absorption properties did not significantly change, *i.e.*, for the rational bottom-up design of a MOF-based artificial photosynthetic scheme, the UV-vis absorption properties of the dissolved molecular PSs and their analogues can be extrapolated.

### 3.2. Tools to study electron/energy transfer

Here, examples are presented where the methods of luminescence quenching, optical transient absorption (OTA) and electron paramagnetic resonance (EPR) spectroscopy have been used to elucidate the details of the respective light-driven processes and catalysis. Once the steady-state absorption properties of the MOFs are known, examination of the processes upon (visible) light absorption is possible.

One possibility to study electron transfer events originating from  $\text{PS}^*$  is time-resolved and steady state luminescence (quenching) measurements. If a MOF-incorporated  $\text{PS}^*$  (MOF\*) represents a luminescent species, then the influence of a catalytic component (already in the MOF scaffold or introduced later), and addition of various reagents (in variable con-

**Table 4** Active molecular components (PS-CAT pairs) in MOF-based photocatalyst for visible light-driven oxidative organic transformation of alcohols and amines

Photocatalytic MOF system	Primary building units		Active molecular components				Cofactors	Type	Ref.
	Linker	SBU	PS	CAT	CAT	CAT			
SYD-1-CuNi		Zr <sub>6</sub> -oxo cluster	Linker: [Ru(L1) <sub>3</sub> ] <sup>2+</sup>		BnOH oxidation using CO <sub>2</sub> or H <sup>+</sup>	I	128		
PCN-22		[Ru(L) <sub>3</sub> ] <sup>2+</sup>	Ti <sub>7</sub> -oxo cluster	Linker: H <sub>2</sub> -TCPP	SBU	BnOH oxidation using O <sub>2</sub> and TEMPO	I	175	
UCFMOF-n		H <sub>2</sub> -TCPP	Ti <sub>6</sub> -oxo cluster		SBU	BnOH oxidation using O <sub>2</sub>	I	68	
NH <sub>2</sub> -MIL-125 (Ti)		Multivariate dicarboxylates	Ti <sub>8</sub> -oxo cluster		SBU	BnOH oxidation using NaBr and O <sub>2</sub>	I	180	
		NH <sub>2</sub> -BDC							



Table 4 (Contd.)

Photocatalytic MOF system	Primary building units		Active molecular components				Cofactors	Type	Ref.
	Linker	PS	CAT	CAT	CAT	CAT			
$[\text{Ru}(\text{bpy})_3]^{2+} + \text{MIL}-125-\text{NH}_2$		Ti <sub>8</sub> -oxo cluster		BnOH oxidation using $\text{O}_2$	I and V	197			
NH <sub>2</sub> -BDC			$[\text{Ru}(\text{bpy})_3]^{2+}$ and MIL-125-NH <sub>2</sub> MOF						
Cr-PCN-600		Cr <sub>3</sub> -oxo cluster	Dual photoexcitation $\text{H}_2\text{-TCPP}$ (Cr-MOFs)	Cr-MOFs No specific local site	BnOH alcohol oxidation using $\text{O}_2$	I	184		
$\text{Zr}_6\text{-Cu/Fe-1}$ $\text{Zr}_6\text{-Cu/Fe-2}$		Zr <sub>6</sub> -oxo cluster		BnOH alcohol oxidation using $\text{O}_2$ and $\text{H}_2\text{O}$	II	184			
			$\text{H}_2\text{-TCPP}$						
			$5,5'\text{-dcbpy}$		$[\text{Fe}(5,5'\text{-dcbpy})(\text{H}_2\text{O})_2\text{Cl}_2]$				
					$[\text{Cu}(5,5'\text{-dcbpy})(\text{XantP})]^+$ or $[\text{Cu}(5,5'\text{-dcbpy})(\text{POP})]^+$				



Table 4 (Contd.)

Photocatalytic MOF system	Primary building units		Active molecular components			Cofactors	Type	Ref.
	Linker	SBU	PS	CAT				
Fe@PCN 224		Zr <sub>6</sub> -oxo cluster	Linker: H <sub>2</sub> -TCPP	H <sub>2</sub> -TCPP but co-occurring Fenton reaction with Fe <sup>III</sup> at TCPP	<sup>i</sup> PrOH oxidation using O <sub>2</sub>		II and IV	195
NH <sub>2</sub> -UiO-66-1D-Fe		Zr <sub>6</sub> -oxo cluster	No specific local site Energy transfer		BnOH alcohol oxidation using O <sub>2</sub>		NA	196
PCN-224(Sb)-L	Isatin-Schiff base complex and NH <sub>2</sub> -BDC		Zr <sub>6</sub> -oxo cluster	Linker: [TCPP(Sb)-X] <sup>+</sup> X: -OH, -OCH <sub>3</sub> , -Br	[TCPP(Sb)-X] <sup>+</sup> and SBU Multiple photocatalytic channel	BnOH oxidation using O <sub>2</sub>	NA	192



Table 4 (Contd.)

Photocatalytic MOF system	Primary building units		Active molecular components				Cofactors	Type	Ref.	
	Linker	SBU	PS	CAT						
Ru or Ir doped-UiO-67		Zr <sub>6</sub> -oxo cluster			[Ru(bpy) <sub>2</sub> (5,5'-dcbpy)] <sup>2+</sup> or [Ir(Cp*) <sub>2</sub> (5,5'-dcbpy)Cl] or [Ir(Cp*) <sub>2</sub> (5,5'-dcbpy)Cl] <sup>2+</sup>		BnOH oxidation using O <sub>2</sub>	NA	279	
NH <sub>2</sub> -MIL-101 (Fe)		Fe <sub>3</sub> -oxo cluster			[Ir(Cp*) <sub>2</sub> (5,5'-dcbpy)Cl] <sup>+</sup> or [Ir(Cp*) <sub>2</sub> (5,5'-dcbpy)Cl] <sup>2+</sup>	NH <sub>2</sub> -MIL-101(Fe) No specific local site	BnOH Oxidation using O <sub>2</sub> followed by Knoevenagel condensation with methylene compounds	I	172	
Bi-TATB		Bi <sub>2</sub> cluster			Bi-TATB No specific local site		BnOH oxidation using O <sub>2</sub>	—	191	
NaRh-MW <sub>12</sub> M: Si, Ge, As	TATB	Rh <sub>2</sub> -paddlewheel			[Rh <sub>2</sub> (OAc) <sub>4</sub> ] and SBU (POMs)		Oxidative coupling of BnNH <sub>2</sub> using O <sub>2</sub>	I	177	
UiO-66-NH <sub>2</sub>		Zr <sub>6</sub> -oxo cluster			[Rh <sub>2</sub> (OAc) <sub>4</sub> ]	Linker: NH <sub>2</sub> -BDC	SBU	Oxidative coupling of BnNH <sub>2</sub> using O <sub>2</sub> and anaerobic condition	I	174
NH <sub>2</sub> -MIL-125 (II)		Ti <sub>6</sub> -oxo cluster			Linker: NH <sub>2</sub> -BDC		NH <sub>2</sub> -BDC and SBU	Oxidative coupling of BnNH <sub>2</sub> using O <sub>2</sub>	I	173



Table 4 (Contd.)

Photocatalytic MOF system	Primary building units		Active molecular components				Cofactors	Type	Ref.
	Linker	SBU	PS	CAT	TATB and SBU/Pt nanoparticles				
Pt/PCN-777			Zr <sub>6</sub> -oxo cluster	Linker: TATB			BnNH <sub>2</sub> using H <sup>+</sup>	I	182
Ti-PMOF			Ti <sub>7</sub> -oxo cluster			SBU	Oxidative coupling of BnNH <sub>2</sub> using O <sub>2</sub>	I	176
LTG-NiRu			H <sub>2</sub> -TCPP	Ni octahedra		SBU	Oxidative coupling of BnNH <sub>2</sub> using O <sub>2</sub>	I	183
Zr-NDI-H <sub>2</sub> DPBP			[Ru(L4) <sub>3</sub> ] <sup>2+</sup>	Zr <sub>6</sub> -oxo cluster		DPBP	NDI and through multiple photocatalytic channels	II	190

Table 4 (Contd.)

Photocatalytic MOF system	Primary building units		Active molecular components			Cofactors	Type	Ref.
	Linker	SBU	PS	CAT				
PMo-1 or SiW-2		Octahedral Cd		Linker and POMs (PMo12O403- or SiW12O404-) through multiple photocatalytic channels	Oxidative coupling of BnNH2 using O2	V	178	
MOF-Ru1		Al2-oxo cluster		[Ru(bpy)2(5,5'-dcbpy)]2+	Oxidative coupling of BnNH2 using O2	V	280	
Mn-MIX		Zn3 cluster		[Ru(5,5'-dcbpy)(L10)2]2+ Energy transfer mechanism	No specific local sites Cooperative effect of two photoactive ligand	NA	193	
				[Ru(5,5'-dcbpy)(L6)2]2+	Oxidative coupling of BnNH2 derivatives using O2	L6		
				[Ru(5,5'-dcbpy)(Zn-TCPP)2]2+	Oxidative coupling of BnNH2 derivatives using O2	Zn-TCPP		



Table 4 (Contd.)

Photocatalytic MOF system	Primary building units		Active molecular components				Cofactors	Type	Ref.
	Linker	SBU	PS	CAT					
Zn-PDI		Tetrahedral Zn	Zn-PDI MOF	Energy transfer			Oxidative coupling of BnNH <sub>2</sub> using O <sub>2</sub>	NA	188
UNLPF-11 or UNLPF 12		[In(COO) <sub>4</sub> ] <sup>-</sup>	[SnCl <sub>2</sub> L7] [SnL7] (BF <sub>4</sub> ) <sub>2</sub>	UNLPF-11 or UNLPF 12. No specific sites and proceed via multiple photocatalytic channels			Oxidative coupling of BnNH <sub>2</sub> using O <sub>2</sub>	NA	187
MOF-LS10		[SnCl <sub>2</sub> L7] or [SnL7] (BF <sub>4</sub> ) <sub>2</sub>	Pillared-Zn <sub>2</sub> paddlewheel				Oxidative coupling of BnNH <sub>2</sub> using O <sub>2</sub>	NA	194
JNU 212-215		H <sub>4</sub> TCPP and DPTZTZ		H <sub>4</sub> TCPP and DPTZTZ No selective site Donor-acceptor linker Energy and electron transfer			O <sub>2</sub>	NA	281

$M_n$  clusters with similar values of  $n$  do not necessarily represent similar structural formulas of SBUs and may vary from one MOF to another. "NA" used in the "Type" column indicates a miscellaneous type of MOF that cannot be categorized.

centrations) such as electron donors and acceptors results in a decrease in the emission intensity<sup>94,101,102</sup> and shorter excited-state lifetimes of PS\* (MOF\*) in the case of successful electron transfer. For example, this has been demonstrated by C. Wang and W. Lin in an  $[\text{Ru}(\text{bpy})_3]^{2+}$ -like metalloligand-based MOF upon the addition of different tertiary amines, serving as reductive quenchers of the Ru-based  $^3\text{MLCT}$  state. These authors not only determined the size-dependent effects on the luminescence quenching efficiency but also the diffusion constants for the various amines through the pores of the MOF utilizing time-dependent luminescence data. If the size of the electron donor was too large, no diffusion into the pores was possible, and consequently no electron transfer, as indicated by the observed reduction in luminescence intensity and lifetime. This also reveals important design criteria for well-working photocatalytic MOF-based systems.<sup>103</sup> It is known that crystalline MOFs with ordered networks offer an extra advantage, which can facilitate the transport of excited states or photoinduced charges to the surface or active site through energy transfer and exciton migration processes.<sup>104–107</sup> Inevitably, the luminescence and charge or energy transfer kinetics of PS\* (MOF) are strongly influenced in these cases, and they exert a significant impact in heterogenous photocatalysis. A detailed analysis of the time-resolved photoluminescence data allowed the excited state events in Re-loaded UiO-67 MOFs to be rationalized (Fig. 7a). Excitation of pristine UiO-67 MOF bearing a  $\text{Zr}_6$ -based SBU and 5,5'-dcbpy linker led to radiative (at 390 nm) and non-radiative deactivation with rate constants of  $7.7 \times 10^5 \text{ s}^{-1}$  and  $1.9 \times 10^7 \text{ s}^{-1}$ ,

respectively. The addition of a Re-sites to the framework caused the deactivation of the excited state by Förster resonance energy transfer (FRET) (Fig. 7b). It was demonstrated that the population of the lower-lying singlet excited state of  $[\text{Re}(5,5'\text{-dcbpy})(\text{CO})_3\text{Cl}]$ , either by direct excitation or energy transfer, led to rapid intersystem crossing to a mixed singlet-triplet state, which decayed to the ground state by radiative (610 nm) and non-radiative pathways with rate constants of  $4.5 \times 10^3 \text{ s}^{-1}$  and  $5.1 \times 10^6 \text{ s}^{-1}$ , respectively.<sup>108</sup> By applying similar techniques, Ferrer *et al.* studied the photoredox properties of an  $[\text{Ru}(\text{bpy})_2(5,5'\text{-dcbpy})]^{2+}$ -incorporated MOF (Rudcbpy-UiO-67(Zr)).<sup>109</sup> According to their investigation, the  $^3\text{MLCT}$  state generated upon visible light excitation decays partly to a very long-lived (millisecond timescale) photoinduced charge-separated state following similar behavior to that of analogous  $[\text{Ru}(\text{bpy})_3]^{2+}$  dissolved in water, except that the lifetime of the soluble complex excited state is orders of magnitude shorter. Contrary to homogenous conditions, it has been demonstrated that MOFs provide a suitable platform for the PS, in which the excited  $[\text{Ru}(\text{bpy})_2(5,5'\text{-dcbpy})]^{2+*}$  triplet electrons transfer to the MOF lattice cluster (e) and the charge on the oxidized species migrates *via* the nearby linker (h) of Rudcbpy-UiO-67 (Zr) MOF upon visible light irradiation (Fig. 7c). Therefore, this PET process inside the MOF leads to a distinct and durable photoinduced charge separation state, which is beneficial for the photocatalytic debromination of  $\alpha$ -bromoketones to achieve high conversions.

The excited-state dynamics in MOFs can also be followed by optical transient absorption (OTA) spectroscopy using UV or

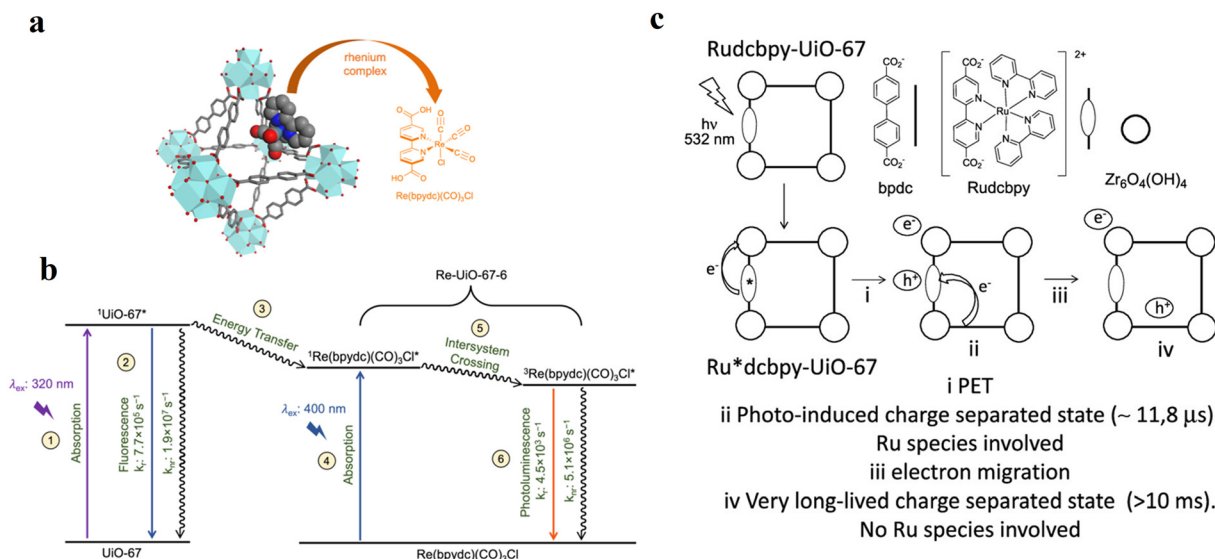


**Fig. 7** (a) Idealized representation of UiO-67 octahedral cavity doped with Re(bpydc)(CO)<sub>3</sub>Cl and (b) simplified Jablonski diagram of UiO-67 and Re-UiO-67-6. (1) Excitation at 320 nm of the UiO-67 MOF results in the formation of  $^1\text{UiO-67}^*$ , which can decay to the ground state by emission or non-radiative relaxation (2).  $[\text{Re}(\text{bpydc})(\text{CO})_3\text{Cl}]$  incorporated in the MOF, as in Re-UiO-67-6, can be excited either by energy transfer from the MOF (3) or direct excitation (4). This singlet excited state undergoes intersystem crossing (5) and then decay to the ground state *via* photoluminescence or non-radiative relaxation (6). Rate constants in (2) represent the excited state evolution of pure UiO-67 with no rhenium complex, given that the fluorescence of the MOF in Re-UiO-67-6 is too quenched to obtain quantum yield and lifetime data. Adapted with permission from ref. 108. Copyright 2022, Elsevier. (c) Proposed PET process upon 532 nm laser excitation of the Rudcbpy-UiO-67(Zr) MOF. Adapted with permission from ref. 109. Copyright 2018, the American Chemical Society.



vis pump and probe pulses. Data analysis of OTA can reveal electron transfer events by identification of the excited state absorption (ESA) or ground state bleach (GSB) signals, which are similar to the signals obtained from spectroelectrochemical measurements of oxidized or reduced PS and CAT. The appearance of signals, and especially their decay can be kinetically analyzed to provide information on the rate of electron transfer and potential charge recombination events. In contrast to the OTA analysis of soluble molecules inside the classical cuvette, samples of MOF-based systems are measured in thin films. For example, S. Yang *et al.* analyzed a mixed-linker MOF with Ru-PS and Pt-CAT moieties designed for light-driven hydrogen evolution. The kinetic analysis of the OTA spectra revealed that compared to the Ru-only MOF, the excited-state lifetime of the Ru-based  $^3\text{MLCT}$  state was reduced by a factor of 4 in the presence of the Pt center. This was assigned to the successful electron transfer from Ru-PS to Pt-CAT.<sup>74</sup> The kinetic analysis of the obtained OTA signals in the presence of various reagents such as sacrificial electron donors and CATs can also be used to unravel the sequence of individual electron transfer steps in MOF-based photocatalysts. In the OTA spectra on the nanosecond timescale, a mixed-linker Zn-PS/Pt-CAT system showed a remarkable decrease in the Zn-PS\* lifetime compared to the Zn-PS-only MOF, whereas the addition of the electron donor phenol had no effect. Thus, it could be concluded that oxidative quenching of Zn-PS\* occurs *via* electron transfer to the neighboring Pt-centers followed by the regeneration of Zn-PS with phenol.<sup>110</sup>

Electron paramagnetic resonance (EPR) spectroscopy interrogates unpaired electrons at specific parts of MOF-based photocatalysts and can support the results from OTA spectroscopy, *i.e.*, it can verify successful charge transfer events. The EPR signals are very sensitive to the surrounding micro-environment, thus providing a more site-specific statement on charge localization compared to the typically broad signals obtained by OTA. In a representative study, a MOF-based photocatalyst for  $\text{CO}_2$  reduction bearing Ru-linkers and  $\{\text{Eu}\}_2$  active sites was analyzed by EPR spectroscopy in the presence of TEOA as an electron donor. Upon irradiation, charge transfer to the  $\{\text{Eu}\}_2$  SBU was confirmed as broad EPR signals, which were attributed to Eu(II). Interestingly, when  $\text{CO}_2$  was introduced, the EPR signal immediately disappeared, confirming electron transfer to  $\text{CO}_2$ .<sup>94</sup>

### 3.3. Tools to study the catalysis and products

Once the electron transfer among PS, CAT and other (sacrificial) agents has occurred, the utilization of the photogenerated charges *via* catalytic turnover is necessary. To achieve the latter, the substrates need to bind to the metal-containing CAT to be activated. Therefore, the CAT needs to offer open coordination sites. The formation of open binding sites is either linked to the charge transfer process itself, *e.g.*, as in  $[(\text{bpy})\text{Rh}(\text{Cp}^*)\text{X}]$ -based CATs, where ligand X is lost from the metal upon Rh reduction,<sup>111</sup> or the open binding site is formed directly from the electronically excited state. Interestingly, time-resolved IR spectroscopy could reveal the photoinduced

dynamics on the MOF scaffold itself, potentially opening the vacant coordination sites necessary for catalytic activity at the SBUs.<sup>112</sup> IR spectroscopy in a diffuse reflectance setup (DRIFTS) was also used to monitor the final step of the photocatalytic cycle, *i.e.* substrate conversion at CAT. Maji and co-workers observed the  $\text{CO}_2$  to CO reduction at the Re-site of a type III MOF bearing Ru-PS and Re-CAT attached to the SBUs. The gradual conversion of the Re-bound COOH species to Re-bound CO species was followed by the formation of characteristic IR bands.<sup>81</sup> Moreover, small molecular products can be identified and quantitatively analyzed using chromatographic techniques such as gas chromatography (GC) and liquid chromatography (LC) coupled with mass spectrometry (MS), as well as spectroscopic methods such as nuclear magnetic resonance (NMR). Additionally, tools such as GC-MS and NMR allow isotope tracing experiments with substrates such as  $^{13}\text{CO}_2/\text{H}_2^{18}\text{O}$ , enabling the study of the reaction mechanisms.

## 4. Examples of MOFs in visible light-driven catalysis

Based on the above-described categorization of MOF designs, the following chapter discusses their applications in various fields, mainly including solar fuel-related light-driven catalysis, *e.g.*, hydrogen evolution reaction (HER), oxygen evolution reaction (OER), overall water splitting,  $\text{CO}_2$  reduction reaction (CO<sub>2</sub>RR), and oxidative organic transformation (benzyl amine/alcohol oxidation) reactions.

### 4.1 Hydrogen evolution reaction (HER)

HER is a two-electron reduction reaction, which occurs at a specifically designed catalytic site. In most cases, HER is investigated independently of the challenging water oxidation reaction (OER), and thus is fueled by a parallel oxidation reaction with a solution-state sacrificial electron donor such as BIH, TEOA, ascorbate, and EDTA (ethylenediaminetetraacetic acid). From a thermodynamic perspective, the catalytically active component must have suitable redox potentials to drive the  $2\text{H}^+/\text{H}_2$  reduction process, and from a kinetic perspective, it must have accessible coordination sites for binding the substrate such as water or  $\text{H}^+$  for generating and stabilizing the reactive metal-hydride intermediate. This intermediate either by homolytic (metal-hydride reacts with another metal hydride to generate  $\text{H}_2$  *via* reductive elimination) or heterolytic pathways (the metal hydride is further reduced and protonated to form  $\text{H}_2$ ) yields the product  $\text{H}_2$ .<sup>21</sup> In the context of MOF research, photocatalytic HER has made progress from two standpoints, as follows: (1) improvement in light absorption capacity and (2) utilization of well-characterized/nature-inspired molecular system by adopting the functionalization/encapsulation strategies (see Table 1). It has been previously reported that MOFs containing Ti(IV) and Ce(IV)-based SBUs coordinated to an electron-rich organic chromophore linker, such as  $\text{NH}_2\text{-BDC}$ , demonstrate photocatalytic HER activity.<sup>113–117</sup> Recently, some new organic/metalloligand



linker-based MOFs have been introduced in this area taking advantage of the well-characterized polypyridyl complexes of Ru(II),<sup>80,118</sup> Ir(III),<sup>118</sup> and Cu(I),<sup>71</sup> and porphyrin-based metal complexes.<sup>119,120</sup> Additionally, MOFs with some noble metal-based SBUs such as Ru(III)<sub>2</sub>, Eu(III), and Pr(III) have been found to achieve very high (gravimetric) TONs due to their superior catalytic activity.<sup>80,119–123</sup> For example, the Lin group synthesized two MOFs, namely Ru-TBP and Ru-TBP-Zn, bearing Ru(III)<sub>2</sub> paddlewheel-like SBUs and porphyrin-derived tetracarboxylate linkers (TBP and TBP-Zn, where TBP is the tetraanion of 5,10,15,20-tetra(*p*-benzoic acid)porphyrin, which is commonly referred to as TCPP in other reports), and studied their HER activities in acetonitrile (MeCN) solution with H<sub>2</sub>O as the proton source and TEOA as the sacrificial electron donor under visible light (Fig. 8a).<sup>120</sup> Despite having a similar ET mechanism (excited porphyrin transfer electron to Ru(III)<sub>2</sub> SBUs, Fig. 8a) in both MOFs, the HER activity of Ru-TBP-Zn (TON: 39.4) was found to be higher than that of Ru-TBP (TON: 21.2) after 72 h irradiation. This was ascribed to the significant role of Zn in enhancing the molar absorptivity of Ru-TBP-Zn. Furthermore, the enhanced HER activity of Ru-TBP-Zn compared to the homogeneous TBP-Zn control (TON: 1.4) con-

firmed that the proximity of the Ru(III)<sub>2</sub> SBUs and porphyrin ligand (~1.1 nm) as well as their hierarchical organization played a key role in facilitating multielectron transfer to drive the photocatalytic HER. The above-mentioned crucial factors for increased TON in type I-based photocatalytic HER MOFs have been commonly highlighted in several studies.<sup>118</sup> Inspired by the [FeFe]- and [NiFe]-hydrogenase model in nature,<sup>124</sup> numerous additional molecular entities such as Cu(II) and Ni(II)-EDTA, [Co(dmgH)<sub>2</sub>(4-COOH-py)Cl]<sup>+</sup> (dmgH = dimethylglyoxime, py = pyridine), and Ni(SH)(OH<sub>2</sub>) and metal sites such as Fe(II)-X (X = Br<sup>-</sup>, Cl<sup>-</sup>, AcO<sup>-</sup>, and BF<sub>4</sub><sup>-</sup>), Ti(III), and Co(I) species have been created in MOFs by modification of their SBUs. Evidently, they promoted the efficiency of the MOF and offered a selective pathway for HER by their specific functions.<sup>71,125–128</sup> One elegant example is Fe(II)-X (X = Br<sup>-</sup>, Cl<sup>-</sup>, AcO<sup>-</sup>, and BF<sub>4</sub><sup>-</sup>) supported on a Zr<sub>6</sub> cluster, which constituted the SBU of a mixed-linker MOF containing nitro-phenyl dicarboxylate and PT (Fig. 8b).<sup>71</sup> The PT-sites were used to assemble a [Cu(PT)(dppe)]<sup>+</sup>-type PS by a series of post-synthetic modifications. The resulting Fe-X@Zr<sub>6</sub>-Cu promoted the light-driven HER with a TON of up to 33 700 and TOF of up to 880 h<sup>-1</sup>. The HER activities of Fe-X@Zr<sub>6</sub>-Cu were found to correlate with the lability of the counter anion X, which is consistent with the generation of open coordination sites at the single-atom Fe centers by de-coordination of the labile X groups to facilitate the formation of Fe-hydride intermediates (Fig. 8b). The modification of the SBUs in the bulk structure of NH<sub>2</sub>-BDC-based MOFs with a large coordination sphere species is challenging due to their pore restrictions. However, these species can be covalently grafted to the SBUs precisely at the surface level. Recently, Zhang *et al.* employed a straightforward post-synthetic modification involving an amide reaction to graft [Pt(bpy)Cl<sub>2</sub>] onto the surface of NH<sub>2</sub>-MIL-125.<sup>129</sup> They demonstrated that the electron-withdrawing effect of the [Pt(bpy)Cl<sub>2</sub>] complex allowed it to serve as a highly efficient electron acceptor, which shifted the photoinduced charge migration pathway from internal BDC → TiO<sub>x</sub> migration to external BDC-PtN<sub>x</sub> migration. The assembled structure (NML-PtN<sub>2</sub>) demonstrated a 225-fold increase in photocatalytic hydrogen evolution activity (7.608 mmol g<sup>-1</sup> h<sup>-1</sup>) compared to the pristine NH<sub>2</sub>-MIL-125. However, further post-modification of the Pt coordination sphere with an additional bipyridine to produce NML-PtN<sub>4</sub> resulted in a 2.26-fold reduction in the hydrogen evolution performance. The authors identified the spatial hindrance and increased Gibbs free energy as the primary causes for this decreased efficiency, which was supported by both theoretical and experimental evidence.

The attachment of a polypyridyl-based metal complex as an additional molecular CAT in the linker leads to the construction of a type II PS/CAT pair (linker-linker) in MOFs. Therefore, several MOFs from the UiO family were built using a PS/CAT pair such as Ru/Pt,<sup>73,74</sup> Ru/Fe,<sup>77</sup> and Cu/Co<sup>75</sup> for photocatalytic HER. For example, an Ru/Pt pair covalently attached to two separate 5,5'-dcbpy linkers of the UiO-67 MOF provided close spatial proximity for efficient electron transfer from the excited PS [Ru(5,5'-dcbpy)(bpy)<sub>2</sub>]<sup>2+</sup> to the CAT [Pt(5,5'-dcbpy)]<sup>2+</sup>. The

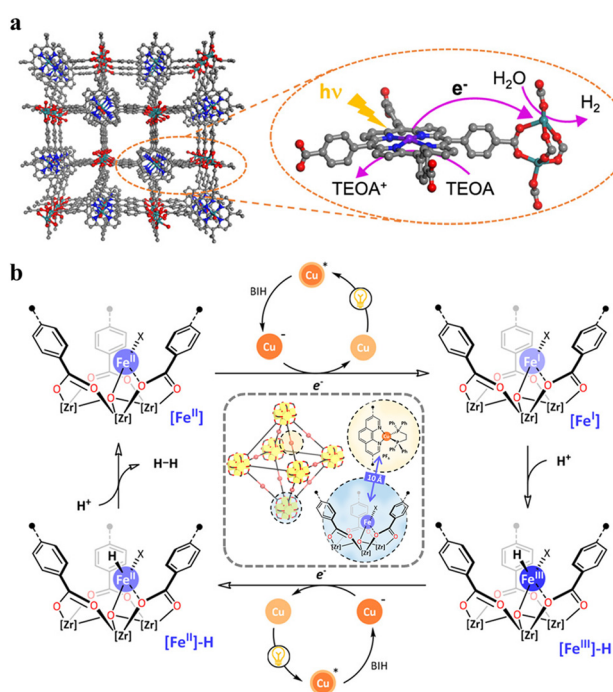


**Fig. 8** (a) Schematic representation of the Ru-TBP (Zn) crystal structure assembled from metallocporphyrin-centered tetracarboxylates and Ru(III)<sub>2</sub> paddlewheel (SBU), showing the visible light-driven HER. Photoexcited porphyrin ligands inject electrons to adjacent Ru<sub>2</sub> SBUs to reduce protons to hydrogen. Subsequently, the oxidized porphyrin ligands are reduced by sacrificial TEOA to regenerate the photocatalytic system. Adapted with permission from ref. 120. Copyright 2018, the American Chemical Society. (b) Sequentially installed Cu(I)-PS and Fe(II)-CAT in Zr<sub>6</sub>-mPT to afford Fe(II)-X@Zr<sub>6</sub>-Cu (X = Br<sup>-</sup>, Cl<sup>-</sup>, AcO<sup>-</sup>, and BF<sub>4</sub><sup>-</sup>) and proposed photocatalytic cycle for H<sub>2</sub> evolution. Adapted with permission from ref. 71. Copyright 2020, the American Chemical Society.



oxidatively quenched PS was re-reduced to its initial state by the sacrificial electron donor  $\text{Na}_2\text{EDTA}$  and the reduced CAT induced the HER in the MOF (Fig. 9a).<sup>73</sup> In addition, the increased stability of PS and CAT in the MOF enhanced the HER activity to several orders of magnitude in comparison to their homogenous control. Unlike the molecular catalytic entity, SACs are also known for their HER activity and were easily created in porphyrin-based MOFs<sup>130–133</sup> employing the porphyrin cavity. Categorically, under these circumstances, these types of MOFs create multiple photocatalytic channels (type I: linker-SBU, type II: linker-linker, and type IV, not ideal dyad: linker-SAC), which can participate in HER. For example, single atomic Pt(II) in the porphyrin cavity of the PCN 222 MOF bearing  $\text{Zr}_6$  clusters<sup>131</sup> or Al-TCPP MOF bearing Al<sub>2</sub> cluster<sup>132</sup> induced the linker to cluster charge transfer mechanism by promoting the charge transfer from the porphyrins (PS) to Pt(II) ions (CAT) in the framework, resulting in a significant improvement in their HER activity compared to their pristine systems. Recently, Kim *et al.* discovered that the HER activity of Pd(II) SACs in a TCPP-based MOF of  $\text{Cu}_2$  clusters outperformed Pt(II) SACs because of the longer lifetime of the photogenerated charge carriers and higher charge transfer efficiency of the former.<sup>84</sup> In another study, Wang *et al.* demonstrated that loading 2 wt% Pt particles as a cocatalyst in

Pd/Yb-PMOF (MOF based on Pd-TCPP linkers and Yb<sub>2</sub> clusters) enhanced the HER activity by nearly threefold compared to the control (Yb-PMOF, 2 wt% Pt). This improvement was attributed to the synergistic catalytic effect between the central Pd in the linker and the Yb ions in the SBU.<sup>134</sup> Recently, the biomimetic  $[\text{Fe}_2\text{S}_2]$  model  $[(i\text{-SCH}_2)_2\text{NC(O)C}_5\text{H}_4\text{N}][\text{Fe}_2(\text{CO})_6]$ <sup>83</sup> was used by Sasan *et al.* and introduced into this type of porphyrin-based MOF *via* the self-assembly molecular recognition approach (Fig. 9b). The central single atom (Zn) at the porphyrin pocket of the MOF (namely ZrPF) provided an axial coordination interaction to the pyridine-N from the  $[\text{Fe}_2\text{S}_2]$  model by forming  $[\text{FeFe}]\text{@ZrPF}$  MOF assemblies and created ideal molecular PS-CAT dyad-like systems within the MOF. With this unique type IV PS-CAT pair, the MOF assemblies retained their catalyst-specific function and HER pathway, while improving the HER activities and stability of the  $[\text{Fe}_2\text{S}_2]$  model significantly than their homogenous control in terms of rate and total hydrogen production yield.

The MOFs with type V PS/CAT pairs include various examples within the scope of HER (see Table 1). For example, Co-dioxime-diimine ( $\text{Co}(\text{m})\text{-L}_x$ ),<sup>135</sup>  $[\text{Co}(\text{TPA})\text{Cl}]\text{Cl}$  (TPA = tris(2-pyridylmethyl)amine),<sup>136</sup>  $[\text{Co}(\text{bpy})_3]^{2+}$ ,<sup>137</sup> and Pt(II)<sup>138</sup>-based HER CATs were encapsulated in numerous visible light active MOFs (see Table 1). The solution-state  $[\text{Fe}_2\text{S}_2]$  model directly

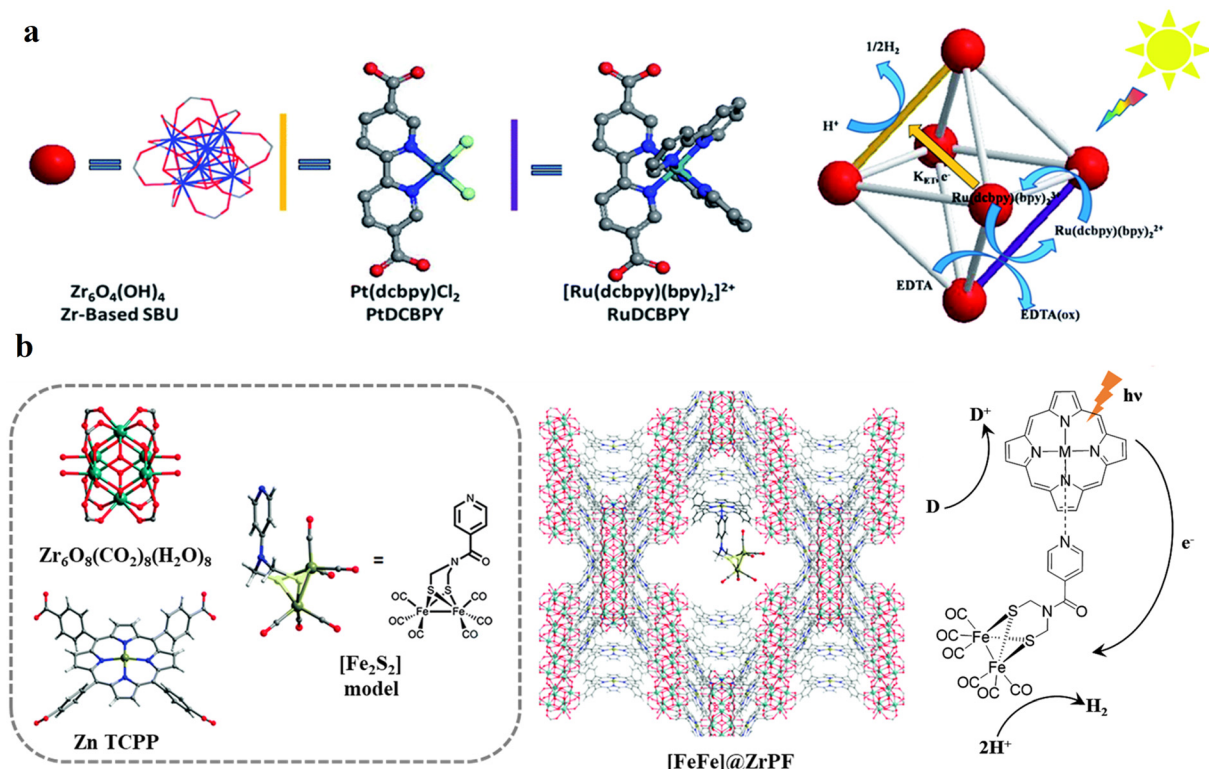


**Fig. 9** (a) Representation of the SBU (red balls), PS linker (yellow rods), and CAT linker (purple rods) in  $\text{UiO-67}$  MOF and proposed reaction scheme for the photocatalytic reduction of protons in the presence of EDTA-2Na (light source: LED  $\lambda > 420$  nm). The backbone of the MOF is shown as the octahedral cavity, where additional rods (grey) represent the bpdc linker (2,2'-biphenyl dicarboxylate). Adapted with permission from ref. 73. Copyright 2015, The Royal Society of Chemistry. (b) Building blocks and an additional CAT unit in the  $[\text{FeFe}]\text{@ZrPF}$  MOF (color scheme: Zr, green; Zn, dark grey; C, light grey; O, red; N, blue; Fe, light green; and S, yellow) for photocatalytic HER in the presence of ascorbic acid as a sacrificial donor (D). Adapted with permission from ref. 83. Copyright 2014, the Royal Society of Chemistry.



injected into a light-harvesting Gd-based MOF bearing a 4,4',4''-tricarboxyltriphenylamine (TCA) linker was examined by Wu *et al.*<sup>139</sup> Alternatively, the direct injection of solution-state PS can be used when the solid MOF contains an active CAT at its scaffold. For example, Eosin Y has recently been incorporated in a mixed-linker MOF of Cu (Zr/Cu-(H<sub>2</sub>BDC-BPD)), where Zr serves as CAT at the SBU.<sup>140</sup> Similarly, in a 2D MOF (M-dcbdt) composed of a butterfly-shaped metal-bis(dithiole) linker and divalent cations (M = Ni, Co, or Fe), the solution-state PS [Ru(bpy)<sub>3</sub>]<sup>2+</sup> can interact with the [MS<sub>4</sub>] units to facilitate the hydrogen evolution reaction (HER).<sup>91</sup> Li *et al.* developed a similar [MS<sub>4</sub>]-rich network in a 2D conjugated MOF nanostructure (HTHATN-Ni-NS) using an HTHATN linker (HTHATN = hexathiohexaaazatrinaphthylene).<sup>141</sup> By integrating an additional Pt(II) site at the uncoordinated NN sites of the linker, they constructed a bimetallic HTHATN-Ni-Pt-NS. This structure exhibited high electrical conductivity and an efficient hydrogen evolution rate of 47.2 mmol g<sup>-1</sup> h<sup>-1</sup>, which was 13.5 times higher than that of the pristine HTHATN-Ni-NS under visible light irradiation. The experimental and theoretical analyses revealed that the introduction of a small amount of Pt(II) provided catalytically active metal sites and optimized the  $\Delta G_{H^+}$  value of the Ni(II) centers, thereby enhancing the proton reduction performance. Pullen *et al.* exploited the same PS [Ru(bpy)<sub>3</sub>]<sup>2+</sup> in a solid-state MOF (UiO-66/[Fe-Fe]) containing an [Fe<sub>2</sub>S<sub>2</sub>] model ([FeFe](dcbdt)(CO)<sub>6</sub>, H<sub>2</sub>dcbdt: 1,4-dicarboxylbenzene-2,3-dithiolate).<sup>142,143</sup> Interestingly, according to the latter example, the authors hypothesized that only the surface-exposed [FeFe] centers were active in photocatalysis. This unexpected phenomenon was proposed to be due to intracrystal linker scrambling, which brings structurally intact catalysts from the crystal interior to the surface, where they can participate in catalysis. This explanation also suggests that [[FeFe](dcbdt)(CO)<sub>6</sub>] in the inner MOF layers is not reduced during earlier photocatalytic HER cycles, and only a fraction of the total CAT species remains active during the initial round of irradiation.

#### 4.2. CO<sub>2</sub> reduction reaction (CO<sub>2</sub>RR)

The CO<sub>2</sub> reduction reaction (CO<sub>2</sub>RR) is a multi-electron and multi-proton process and can yield a variety of reaction product(s), such as CO, HCOOH, MeOH, and even longer chain alcohols and higher alkanes. Therefore, artificial CO<sub>2</sub>RR systems not only help in establishing a second carbon cycle parallel to the natural one but potentially attenuate the adverse effects of CO<sub>2</sub> on the climate by utilizing it as a C1-feedstock. However, most molecular CATs mainly produce a two-electron reduction product, *i.e.*, CO or HCOOH, and typically have the following chemical composition: *fac*-[M(bpy)(CO)<sub>3</sub>X]<sup>n+</sup> with M = Re(I), Mn(II) (X = Cl<sup>-</sup>, Br<sup>-</sup>, PR<sub>3</sub>, *etc.*) producing CO as the main product, [Ru(bpy)Cl<sub>2</sub>(CO)<sub>2</sub>] and [Rh(bpy)(Cp\*)Cl]<sup>+</sup> (Cp\* = η<sub>5</sub>-C<sub>5</sub>Me<sub>5</sub>) producing HCOOH as the main product, and [M(cyclam)]<sup>2+</sup> with M = Co(II) or Ni(II) (cyclam = 1,4,8,11-tetraazacyclotetradecane) as well as porphyrin complexes, mainly with Co as the central metal, also yielding CO

as the main product. In view of the material incorporated in the MOF architectures, these systems bearing bpy ligands offer options for metal-containing linkers (type II, see Fig. 5) or attachment to SBUs (type I or type III). Similarly, metal-containing tetra-carboxylated porphyrins can also be used as linkers in MOFs. In contrast, the cyclam systems only enable noncovalent incorporation in the pores of the MOF (type V). Additionally, the chemistry and catalytic behavior of CATs in solution have been investigated in great detail, and thus also reviewed extensively over the years.<sup>144-146</sup> Consequently, their requirements for optimal catalytic activity are known. This allows the rational embedding of these CATs into suitable matrices for the design of well-functioning and heterogenized artificial photocatalytic systems. Redox-active SBUs such as Zr<sub>6</sub>, Ti<sub>8</sub> cluster, and Co-imidazolate tetrahedra [Co(2-MIM)<sub>4</sub>]<sup>2-</sup> in a solid MOF were also utilized *via* PS installation.<sup>69,147,148</sup> Encouraged by the beneficial aspects of MOF-integration such as improved (long-term) stability, recyclability and improved activity due to the spatial proximity between the CAT and PS, many of the above-listed CO<sub>2</sub>RR CATs have already been investigated in an MOF-based artificial photocatalytic scenario (see Table 2). One of the most commonly used CO<sub>2</sub>RR CATs for incorporation in MOFs is Re-based complexes containing mono- or di-carboxylated bpy-like ligands together with 3 CO ligands and a sixth ligand X completing the coordination environment around Re (see Fig. 6e). In a study employing three different MOF matrices, namely UiO-66, -67, and -68, in combination with [ReBr(CO)<sub>3</sub>(4,4'-dcbpy)] linkers as CAT and [Ru(bpy)<sub>2</sub>(5,5'-dcbpy)]Cl<sub>2</sub> linkers as PS, it was determined whether both are outside or inside the MOF or whether only CAT was incorporated *via* H-bonding with the linker-based NH<sub>2</sub>-groups.<sup>88</sup> The obtained data were evaluated as follows: high photoactivity and rapid deactivation of the UiO-66 containing system, which does not allow stability by neither increasing the uptake of CAT nor PS; low activity for UiO-67, which only takes up CAT and shows mediocre activity, and higher stability for UiO-68, incorporating PS and CAT. This clearly highlights that the MOF-matrices need to be fine-tuned to the specific PS and CAT species to enable optimal photoactivity. A similar effect was also observed for the MIL-101-NH<sub>2</sub>(Al) MOF matrix.<sup>149</sup> The incorporation of molecular PS and CAT in the pores led to improved and longer duration of photocatalytic activity from initially 1.5 h under homogeneous conditions to 40 h under the chosen MOF conditions. The deactivation was mainly ascribed to the degradation of PS, and thus a restart of the photocatalytic CO<sub>2</sub>RR process could be achieved by adding additional PS.

Interestingly, further development in the field led to biomimetically optimized photocatalytic activity. A mixed-linker MOF (Re-MOF-NH<sub>2</sub>) bearing 5,5'-dcbpy and NH<sub>2</sub>-functionalized 2,2'-biphenyl dicarboxylic acid (H<sub>2</sub>bpdc-(NH<sub>2</sub>)<sub>2</sub>) in a rational proportion was prepared, followed by the covalent attachment of [Re(CO)<sub>3</sub>(5,5'-dcbpy)Cl] (abbreviated as ReTC) to create Zr<sub>6</sub>O<sub>4</sub>(OH)<sub>4</sub>(ReTC)<sub>1.26</sub>(bpdc-(NH<sub>2</sub>)<sub>2</sub>)<sub>4.08</sub>(bpdc)<sub>0.63</sub>, allowing intermolecular stabilization of the carbamate intermediates in an enzyme-like fashion (Fig. 10a). This was demon-



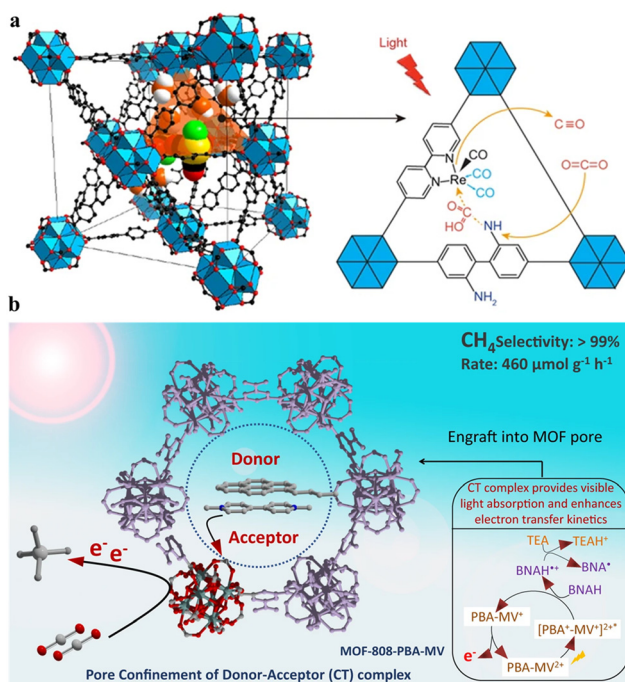


**Fig. 10** (a) Structure and cooperative interaction between an amino-functionality of  $\text{H}_2\text{bpdc}-(\text{NH}_2)_2$  and  $\text{H}_2\text{ReTC}$  within the  $\text{UiO-67}$ -based mixed-linker MOF employed in the photocatalytic  $\text{CO}_2$ -to- $\text{CO}$  conversion. Atom labelling: C, black; O, red; Zr, blue polyhedra; Re, yellow; and Cl, green. H atoms are omitted for clarity. Adapted with permission from ref. 150. Copyright 2017, Nature. (b) Schematic of grafting a donor-acceptor (PBA-MV) complex to MOF-808 (Zr) pore for visible light-driven  $\text{CO}_2$  reduction to selective  $\text{CH}_4$  production. Here, the D-A complex acts as a light harvester to boost the electron flow near the catalytic site in the presence of light. Adapted with permission from ref. 151. Copyright 2017, Nature.

stated to produce an approximately 3-fold increase in photocatalytic activity for the conversion of  $\text{CO}_2$  into  $\text{CO}$ .<sup>150</sup> Similar results were also observed by Batoo *et al.* for the  $\text{UiO-67}$  MOF ( $\text{Cu}/\text{I}_2\text{-Zr-BPDC/BPyDC}$ ) composed of  $[\text{Cu}(5,5'\text{-dcbpy})]^{2+}$  and  $\text{I}_2\text{-BPDC}$ .<sup>152</sup> Interestingly, under 450 nm light irritation, the  $\text{Cu}(\text{II})$  complex in  $\text{Cu}/\text{I}_2\text{-Zr-BPDC/BPyDC}$  was shown to solely produce  $\text{MeOH}$  from  $\text{CO}_2$  in the presence of  $[\text{Ru}(\text{bpy})_3]^{2+}$  and TEOA, while the photoactive  $[\text{Re}(\text{CO})_3(5,5'\text{-dcbpy})\text{Cl}]$  in the Re-MOF- $\text{NH}_2$  MOF was demonstrated to produce  $\text{CO}$  under visible light (400–700 nm) in the presence of TEA. However, given that Re is a very expensive and rare metal, recent developments in this field allowed it to be replaced by its lighter group 7 analogue, Mn. This more sustainable version of a  $\text{CO}$ -yielding  $\text{CO}_2\text{RR}$  CAT was also incorporated into MOF architectures. Lin and co-workers reported a direct isostructural comparison of Re and Mn CATs, which were both incorporated in  $\text{Hf}_{12}$ -based metal-organic layers (MOLs) containing  $[\text{Ru}(\text{bpy})_3]^{2+}$ -based PS as the linkers.<sup>153</sup> The replacement of the capping carboxylates by mono-carboxylated bipyridines enabled subsequent CAT integration using the respective  $[\text{M}(\text{CO})_5\text{Cl}]$  precursors ( $\text{M} = \text{Re, Mn}$ ). With BNAH or BIH, as easy to oxidize electron donors, the Re-based system proved to be *ca.* 4 times more efficient than the Mn-based MOLs. Nevertheless, the same Mn-

based CAT proved to be active in a  $\text{Zr}$ -MOF-808-based system coupling  $\text{CO}_2$  reduction with water oxidation, *i.e.*, it could drive the reductive half reaction of an artificial photosynthetic system.<sup>79</sup> A more detailed discussion can be found in Chapter 3.4. covering this topic. Using the same MOF, and by confining the charge transfer complex within the MOF pores, this group also reported  $\text{CH}_4$  formation ( $7.3 \text{ mmol g}^{-1}$ , 99% selectivity) from the  $\text{Zr}_6\text{-SBU}$  in an aqueous solution of BNAH and TEA (Fig. 10b).<sup>151</sup> To accomplish this, 1-pyrenebutyric acid (PBA) was post-synthetically grafted to the defect-engineered  $\text{Zr}$ -MOF-808 by replacing the exchangeable formate groups. Subsequently, methyl viologen (MV) was incorporated in the confined space of the post-modified MOF to form a donor-acceptor complex. This complex acted as an antenna to harvest visible light and regulate the electron transfer to the catalytic center ( $\text{Zr}_6$  cluster), enabling the visible light-driven  $\text{CO}_2$  reduction reaction. In contrast to the two reports on Re described above, Mn-based CATs were also incorporated in MOFs not only by mono-carboxylated bpy for SBU-attachment but also as linkers. The use of  $\text{UiO-67}$  with 5,5'-dcbpy moieties allowed subsequent modification with  $[\text{Mn}(\text{CO})_5\text{Br}]$ .<sup>154</sup> Interestingly, during photocatalytic  $\text{CO}_2\text{RR}$  in a DMF/TEOA mixture with  $[\text{Ru}(\text{dmbpy})_3]^{2+}$  (dmbpy = 4,4'-dimethyl-2,2'-bipyridine) as freely diffusing PS, the main product was formate ( $\text{HCOO}^-$ ), and when attaching the same PS to the SBU, as described above,  $\text{CO}$  was the main product. A long irradiation time (18 h) yielded a TON of 110 with a quantum yield of 6.7%, where in the first 4 h, the quantum yield even approached 13.8%, which are relatively high numbers. Due to their capability to catalyze multiple reductive transformations,  $[(\text{bpy})\text{Rh}(\text{Cp}^*)\text{Cl}]^+$ -based systems have been investigated in great detail.<sup>155</sup> Besides HER and organic transformations such as nicotinamide and carbonyl reductions, this CAT is also known to carry out  $\text{CO}_2\text{RR}$ . Utilizing an  $\text{UiO-67}$  framework, the linker exchange reaction with  $[(5,5'\text{-dcbpy})\text{Rh}(\text{Cp}^*)\text{Cl}]\text{Cl}$  (or the Rh-bound  $\text{Cl}^-$  being replaced by  $\text{H}_2\text{O}$ ) yielded the respective Rh-functionalized MOF. In the presence of  $[\text{Ru}(\text{bpy})_3]\text{Cl}_2$  as PS and TEOA as sacrificial electron donor under an atmosphere of  $\text{CO}_2$ , the main photocatalysis product was  $\text{H}_2$  but  $\text{CO}_2\text{RR}$  products were also detected. Formate was produced *ca.* half as efficiently as  $\text{H}_2$  and the selectivity of  $\text{HCOO}^-$  over  $\text{CO}$  was greater than 9:1.<sup>156</sup> In a very similar system,  $\text{HCOO}^-$  and  $\text{H}_2$  were formed in an approx. 1:1 ratio and the MOF-based photocatalytic approach proved to be as efficient as the molecular approach, while representing better stability and higher selectivity for  $\text{CO}$ .<sup>157</sup> In a structural closely related system, entrapping of  $\text{PW}_{12}\text{O}_{40}^{3-}$  in the pores of the MOF led to a *ca.* 2-fold increase in photocatalytic activity for  $\text{CO}_2\text{RR}$ , yielding  $\text{HCOO}^-$ . This was ascribed to the POM acting as an electron relay, and thereby optimizing the electron transfer between  $[\text{Ru}(\text{bpy})_3]^{2+}$  PS and  $[(5,5'\text{-dcbpy})\text{Rh}(\text{Cp}^*)\text{Cl}]\text{Cl}$  CAT.<sup>158</sup> Finally, the  $\text{Rh}(\text{Cp}^*)$  unit was also included in MOF architectures utilizing hydrogen bonding between and the amino groups of  $\text{MIL-101-NH}_2$  and the carboxylates of  $[(4,4'\text{-dcbpy})\text{Rh}(\text{Cp}^*)\text{Cl}]\text{Cl}$ . Similarly, the PS  $[\text{Ru}(\text{bpy})_2(4,4'\text{-dcbpy})](\text{PF}_6)_2$  was also introduced.<sup>159</sup> Interestingly, and in contrast to the two reports dis-

cussed above, exclusive formate formation was found. Moreover, the comparison between both PS and CAT being incorporated into the MOF *vs.* experiments with a PS only in the pores and without carboxylate anchors yielded a lower amount of formate. This again highlights the beneficial effect of the MOF skeleton bringing PS and CAT in closer proximity to ultimately improve the electron transfer, and therefore photocatalytic output. As described above,  $[(bpy)Rh(Cp^*)Cl]^{+}$ -like CATs are also capable of reducing oxidized nicotinamides such as biologically active  $NAD^+$  and  $NADP^+$ . This reactivity was exploited by Farha and colleagues in a photobiological network, where they introduced  $[(5,5'-dcbpy)Rh(Cp^*)Cl]$  as linkers into the NU-1006 framework together with the enzyme FDH (FDH = formate dehydrogenase), which reduced  $CO_2$  to formate when being trapped in the pores of the MOF. Utilizing pyrene-based linkers as PS and TEOA as the sacrificial electron donor, electron transfer from PS to the Rh centers led to NADH formation inside the pores of the MOF, *i.e.*, in very close proximity to the entrapped FDH, which could directly consume these biologically usable reducing equivalents to drive overall photocatalytic  $CO_2$ RR with a TOF of  $865\text{ h}^{-1}$ .<sup>111</sup> Recently, Li *et al.* developed a Zr-based MOF (GDUT-8) featuring uniquely thiophene-functionalized biphenyl dicarboxylates.<sup>67</sup> Upon light irradiation, the adjacent thiophene pendants in GDUT-8 underwent a Scholl reaction, transforming it into GDUT-8-Ox. This transformation significantly enhanced the electrical conductivity of the MOF by two orders of magnitude (from  $2.3 \times 10^{-5}\text{ S cm}^{-1}$  to  $6.1 \times 10^{-3}\text{ S cm}^{-1}$ ), facilitating the more efficient transport of photogenerated carriers. With the improved ligand-to-cluster charge transfer (LCCT) efficiency and a broader absorption profile (extending from 400 to 800 nm), GDUT-8-Ox ( $1078\text{ }\mu\text{mol g}^{-1}\text{ h}^{-1}$ ) outperformed GDUT-8 ( $533\text{ }\mu\text{mol g}^{-1}\text{ h}^{-1}$ ) in photocatalytic  $CO_2$  reduction, producing formate with 100% selectivity.

#### 4.3. Oxygen evolution reaction (OER)

The oxidation of  $H_2O$  to  $O_2$  ( $2H_2O \rightarrow O_2 + 4H^+ + 4e^-$ ) has always been a challenging task and is considered to be the bottleneck in the development of sustainable artificial solar fuel generation and water splitting systems. It requires the transfer of four electrons and rearrangement of multiple bonds, including the formation of the O–O bond at the catalytic site, which either takes place *via* radical-oxo-coupling (interaction of two M–O units, I2M mechanism) or water nucleophilic attack (WNA mechanism at single metal site). Subsequently, the respective peroxide species  $[M-O-O-M]$  and  $[M-O-O-H]$  can undergo further oxidation to release  $O_2$  (see Fig. 11).

The complexity of the whole process makes the overall reaction kinetics intricate.<sup>60,160</sup> In nature, the majority of redox processes occurs at the molecularly defined catalytic site *via* either one- or two-electron processes. Also, in artificial catalysis systems, one- or two-electron processes are typically easier, and therefore CAT decomposition<sup>160</sup> and the formation of highly reactive oxidized intermediates *via*  $H_2O \rightarrow \cdot OH + H^+ + e^-$  are frequently faster than  $O_2$  production.<sup>161</sup> Primarily, the CAT must possess a suitable potential match to accumulate

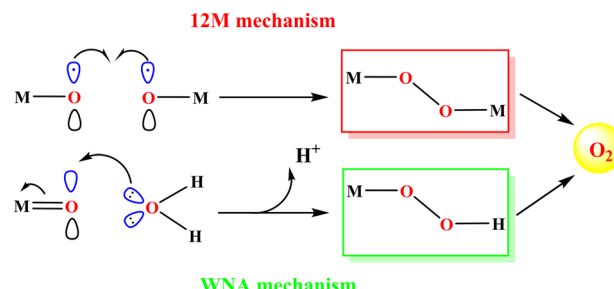


**Fig. 11** Schematic representation of the two mechanistic pathways for O–O bond formation for single-site (solvent water nucleophilic attack, WNA) and dinuclear (interaction of two M–O units, I2M) artificial oxygen evolution catalysts (OECs).

four equivalents of electrons from the PS and oxidize the water molecule to  $O_2$  (+1.23 V *vs.* NHE). Several other factors such as pH of the medium and sacrificial acceptors also play a role. Overall water splitting is associated with a large overpotential and high activation barrier. Currently, the water oxidation half reaction is studied by using sacrificial acceptors such as  $[S_2O_8]^{2-}$ , TCBQ (tetrachloro-benzoquinone),  $Fe^{3+}$  and  $Ce^{4+}$ .  $Ag^+$  is typically avoided as oxidant, given that it can form catalytically active nanoparticles.<sup>162,163</sup> In the context of MOFs, carboxylate linker-based type I-MOFs are restricted to reduction reactions (HER and  $CO_2$ RR), and there are few examples reported with the functionalization of the linker or SBU (type II–V herein, see Table 3). In the type II category, Wang *et al.* reported the synthesis of MOF flakes composed of linkers functionalized with an  $[Ru(bpy)_3]^{2+}$ -type PSs ( $[Ru(bpy)_2(5,5'-dcbpy)]^{2+}$ ) and iridium bipyridyl CAT ( $[Ir(5,5'-dcbpy)]^{3+}$ ) in a  $Zr_{12}$ -based SBU ( $Zr_{12}(\mu_3-O)_8(\mu_3-OH)_8(\mu_2-OH)_6$ ). Irradiating this MOF with LED light at 450 nm yielded  $O_2$  in the presence of different sacrificial acceptors such as  $Na_2S_2O_8$ , TCBQ, and  $Fe^{3+}$ . Interestingly, the authors could realize overall water splitting by co-assembling this MOF with a HER MOF within lipid bilayer vesicles (see Chapter 4.4 for more details).<sup>110</sup> Of course, it will be desirable to replace rare earth metals, such as Ru and Ir, numerous earth abundant and 1<sup>st</sup> row transition metal-based OECs are available with Mn, Fe, Cu or Co, partly inspired by the natural  $Mn_4Ca$  OEC.<sup>160</sup> However, incorporating them in MOF architectures requires careful synthetic linker design prior to the synthesis of the MOF or a suitable post-functionalization strategy to integrate them into the MOF. Meanwhile, polypyridyl-based carboxylated linkers are very elegant, but their complexes (PS or CAT) often suffer from degradation after prolonged reaction times. Consequently, carbon-free molecular CATs, such as polyoxometalates (POMs), have emerged as OECs. POM-based CATs can be incorporated within the pores of MOFs (type V) by using the MOF building blocks as PS. Another option is the incorporation of a well-known solution state PS within the pores and the SBU acting as CAT.<sup>164–166</sup>

A specific example in this context is the exceptionally stable cobalt-based MOF (MAF-48:  $[Co_8(OH)_4(H_2O)_2(bdt)_6]$ ) consisting of a 1,4-benzenedi(1H-1,2,3-triazole) linker ( $H_2bdt$ ) and  $Co_8(\mu_4-$



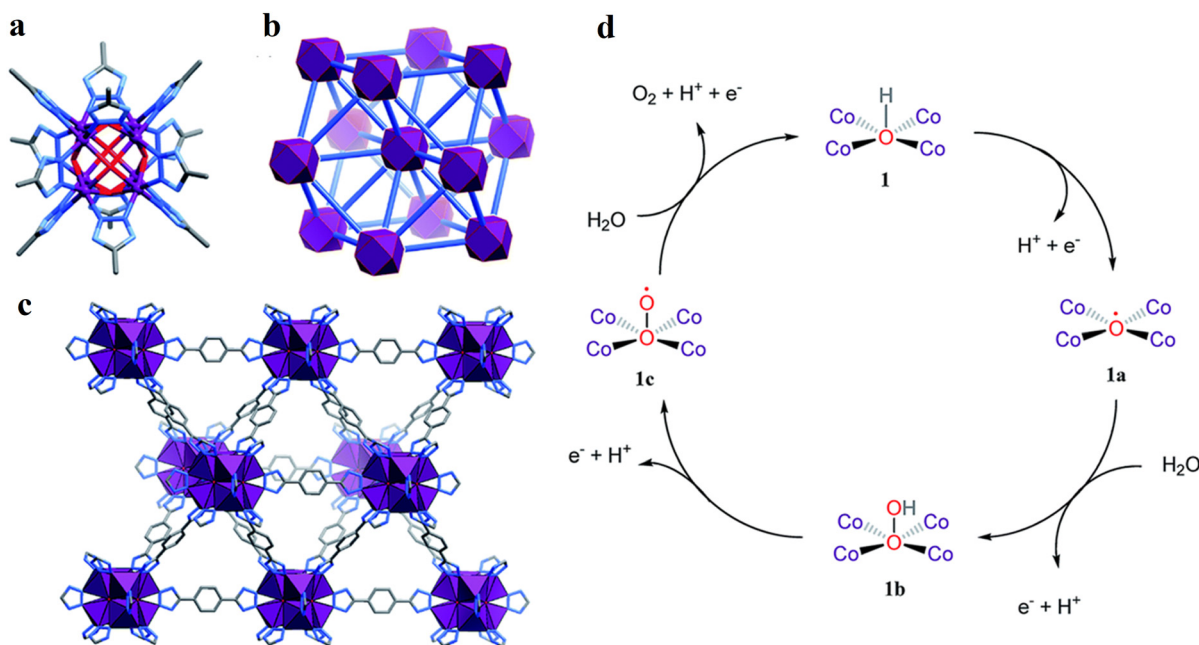


**Fig. 12** (a)  $\text{Co}_8(\mu_4\text{-OH})_6(\text{Rtrz})_{12}$  cluster ( $\text{Rtrz}^- = 1,2,3\text{-triazolate group}$ ), (b) network topology (octanuclear clusters: violet polyhedra and bistriazolate ligands: blue sticks), and (c) 3D coordination framework ( $\text{Co}_3\text{N}_3\text{O}_3$  units: violet polyhedra) of MAF-48 (hydrogen atoms are omitted for clarity). (d) Proposed reaction mechanism for using MAF-48 as CAT for light-driven water oxidation. Adapted with permission from ref. 165. Copyright 2019, the Royal Society of Chemistry.

$\text{OH})_6(\text{Rtrz})_{12}$  cluster ( $\text{Rtrz}^- = 1,2,3\text{-triazolate group from bdt}$ ) (Fig. 12a–c). Additionally,  $\text{Ru}(\text{bpy})_3^{2+}$  was added to the pores and visible light irradiation in the presence of  $\text{Na}_2\text{S}_2\text{O}_8$  yielded  $\text{O}_2$  with a TON  $\sim 1.2 \times 10^6$ .<sup>165</sup> According to the mechanistic investigations, the  $\mu_4\text{-OH}$  group within the  $\{\text{Co}_8(\mu_4\text{-OH})_6\}$  SBU actively participates in the reaction, providing an oxygen vacancy site with optimal  $\text{OH}^-$  adsorption energy. Each facet of  $\{\text{Co}_8(\mu_4\text{-OH})_6\}$  coordinates hydroxyl anions linking four coplanar  $\text{Co}^{II}$  ions in the conventional  $\mu_4$  mode, forming a  $\{\text{Co}_4(\mu_4\text{-OH})\}$  unit (abbreviated as **1**), which serves as the fun-

damental catalytic site for water oxidation (see Fig. 12d). Briefly, (i) complex **1** is oxidatively activated by the photo-generated hole. (ii) The nucleophilic attack of the water molecule forms an O–O bond. (iii) Complex **1b** is oxidized to complex **1c**. (iv) Complex **1c** is further oxidized to evolve  $\text{O}_2$ , accompanied by the regeneration of **1**. Another example encapsulates POM-based OECs within the large pores of porphyrin-based MOFs. Dolbecq *et al.* immobilized a sandwich-type  $[(\text{PW}_9\text{O}_{34})_2\text{Co}_4(\text{H}_2\text{O})_2]^{10-}$  in the hexagonal channels of the MOF-545 framework bearing  $\text{Zr}_6$ -based SBU (Fig. 13).<sup>167</sup>

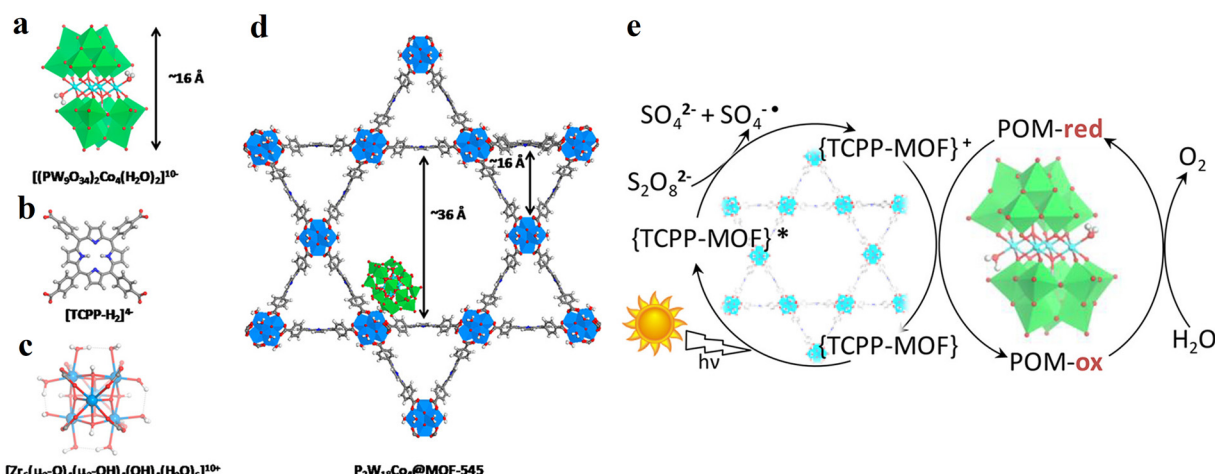


**Fig. 13** POM@MOF-545 components: (a)  $\text{P}_2\text{W}_{18}\text{Co}_4$  POM; (b) TCPP- $\text{H}_2$  linker; (c) Zr-based unit; and (d)  $\text{P}_2\text{W}_{18}\text{Co}_4@\text{MOF-545}$ . (e) Schematic representation of the proposed mechanism for the light-driven OER by  $\text{P}_2\text{W}_{18}\text{Co}_4@\text{MOF-545}$ . Adapted with permission from ref. 124. Copyright 2018, the American Chemical Society.

Elucidation of the mechanism revealed that first light was captured by the porphyrin, followed by the excited state undergoing one-electron oxidation by the sacrificial electron acceptor, and then one-electron oxidation of the POM evolved  $O_2$  after accumulation of 4 oxidizing equivalents.

#### 4.4. Overall water splitting/reaction

In contrast to Chapters 4.1 to 4.3, which only covered reductive or oxidative half reactions catalyzed by MOFs and with the help of sacrificial agents, the overall water splitting reaction driven by visible light and MOF-based CATs is very rare, as described in this chapter. The  $2H_2O \rightarrow 2H_2 + O_2$  reaction represents the “holy grail” of solar energy conversion. However, there is a limited number of reports utilizing molecular or molecular-like approaches with all active components being part of a single system (e.g. all compounds dissolved in one solution). The challenges associated with this approach are diverse, as follows: (i) undesirable charge recombination events of reduced CATs for reductive substrate transformations with oxidized CATs for OER and (ii) the reduced or oxidized product being poisons for the oxidative or reductive half reactions, respectively, the electron transport processes, and many more. Consequently, the typical systems for the overall water splitting do not contain all the active components in one homogeneous solution but instead embedded by some means in a molecular- or material-based boundary separating the two half reactions and the catalytically produced products to avoid the cross-reactivity described above. Interestingly, with the help of liposome architectures this has been achieved for two MOF-based overall water splitting system. In their Z-scheme-inspired work, Wang and colleagues utilized two separate Hf(IV)-based MOF architectures (namely WOR and HER consisting of 5,5'-dcbpy, and TCPP linkers, respectively) with type II PS/CAT pairs (according to the classification shown in Fig. 5) and organized (i)  $[Ru(bpy)_3(5,5'-dcbpy)]^{2+}/[Ir(5,5'-dcbpy)(H_2O)_x]^{3+}$ -modified WOR MOF inside the hydrophilic liposome interior, and (ii) Zn-TCPP/Pt-TCPP-modified and pentafluoropropionic acid-capped HER MOF nanosheet inside the hydrophobic bilayer.<sup>110</sup> As a redox shuttle bifunctional system consisting of an Fe(II)/Fe(III) pair for the reactions in a hydrophilic environment, a chlorinated quinol/quinone pair for charge transport in a hydrophobic environment was used. Individual testing of the HER and OER MOFs showed dramatically higher activity of the HER-MOF, indicating that the overall water splitting reaction will be OER activity-limited. A variety of other test reactions and the formation of  $H_2$  vs.  $O_2$  in the ratio of *ca.* 2 : 1 indicated an overall water splitting reaction and a quantum yield of  $1.5 \pm 1\%$  under 436 nm LED irradiation. In another study, Lan *et al.*<sup>33</sup> developed a trifluoroacetate (TFA)-capped MOF monolayer laterally connected by PS/CAT pairs and a cofactor such as an amino acid (AA), which was applied as an artificial metal-organic enzyme (MOZ) for overall  $CO_2$  photoreduction. The single solid MOF with -diimine and -dicarboxylate linker ( $L_{NN}$ : 4,4'-di(4-benzoato)-2,2'-bipyridine) and  $Hf_{12}$  clusters enabled the rational integration of type I-based PS/CAT pairs-AA cofactors, as follows: (1)  $[Ir(L_{NN})(L_{CN})_2]^{+}/[Ir(H-MBA)Cp^*Cl]^{+}$ -Gln for OER and (2)  $[Ir(L_{NN})(L_{CN})_2]^{+}$ /ferric protoporphyrin haemin-Asn for  $CO_2$ RR ( $L_{CN}$ : 2-(2,4-difluorophenyl)-5-(trifluoromethyl)pyridine), H-MBA: 2-(4'-methyl-[2,2'-bipyridin]-4-yl)acetic acid,  $Cp^*$ : pentamethylcyclopentadienyl, Gln: glutamine, and Asn: asparagine. The resultant Z schemes systems possessed the capability to catalyze OER and  $CO_2$ RR simultaneously in the presence of a catalytic amount of  $[Co(bpy)_3]^{2+}$  redox mediator. The authors also demonstrated the critical role of AA residues. For instance, Asn with a high  $pK_a$  offered H-bond interactions with  $CO_2$  and associated intermediates, while Gln with a small  $pK_a$  value sped up the PCET process in OER. The contribution of both factors significantly promoted the overall reaction efficiency.

In contrast to the systems described above, two other reports are available describing  $CO_2$  reduction in an aqueous medium in the absence of any sacrificial acceptor. Wang and co-workers reported the selective formation of CO together with  $O_2$  formation by a recyclable Cu-TCPP-based MOF hybridized with  $TiO_2$ . The authors obtained indirect proof *via* EPR spectroscopy and radical trapping experiments and proposed that CO formation occurs at the Cu site, while OER proceeds at the  $TiO_2$  semiconductor.<sup>168</sup> In contrast, the system from Maji and colleagues employed a type III MOF with  $[Ru(bpy)_3]^{2+}$ -like PS and  $[Mn(bpy)(CO_3)Br]$ -like CAT both being attached to the SBUs of Zr-MOF-808. This MOF yielded CO with  $>99\%$  selectivity as well as  $O_2$  in a *ca.* 2 : 1 ratio ( $CO/O_2$ ), as determined by GC-MS. The authors hypothesized that the SBU acts as OER CAT.<sup>79</sup>

#### 4.5. Oxidative organic transformation of alcohols and amines

Photocatalytic oxidation reactions of organic molecules are thermodynamically downhill processes<sup>169</sup> and are either associated as side reactions in HER/ $CO_2$ RR due to the utilization of alcohols or amines as sacrificial electron donors or as target reactions in the presence of an oxidant for producing value-added chemicals. Under an aerobic atmosphere and in the presence of  $O_2$  and  $H_2O$ , multiple ROS can be produced, which can result in very complex reaction pathways and different product distributions (see Fig. 14). Specifically, the presence of hydroxyl radicals,  $^{\bullet}OH$ , often causes the over-oxidation to carboxylic acids and the further degradation of

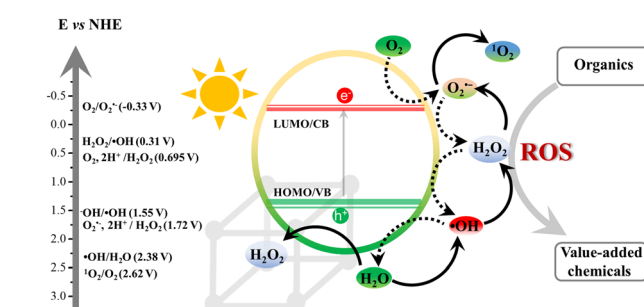
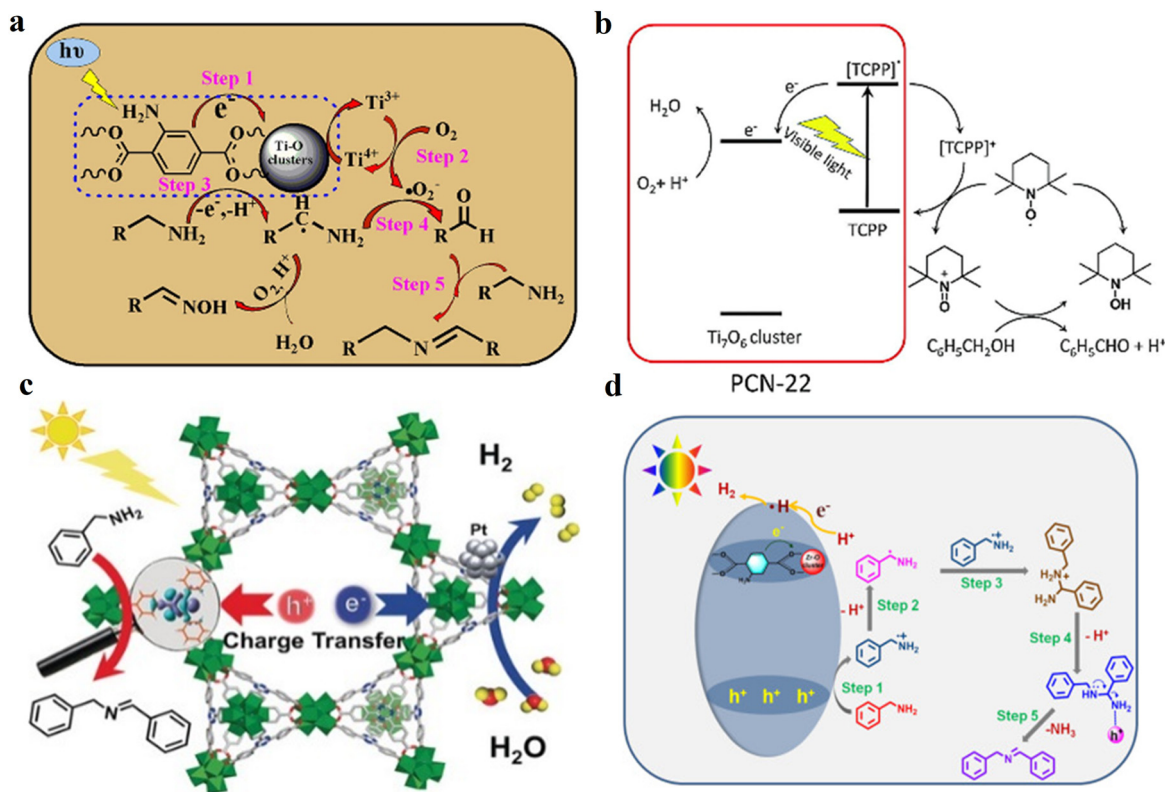


Fig. 14 General illustration of possible reactive oxygen species (ROS) in MOF-based photocatalysts responsible for oxidation reactions under an aqueous and aerobic conditions.<sup>171</sup>

organic molecules into  $\text{CO}_2$  and  $\text{H}_2\text{O}^{170}$ . One example in this context is the overoxidation of benzyl alcohol to the undesirable benzoic acid by photogenerated  $\cdot\text{OH}$ . Overoxidation and degradation can be avoided by using relatively mild oxidants such as the superoxide anion radical ( $\text{O}_2^{\cdot-}$ ) or singlet oxygen ( ${}^1\text{O}_2$ ). Given that the band positions of the photocatalysts and the redox properties of the photocatalysts and the redox properties of the photogenerated species usually play a decisive role in generating these specific oxidants, light-driven oxidant generation can lead to increased efficiency and product selectivity in the desired conversion. Within the scope of photocatalytic oxidations with MOFs, the following conversions are the most relevant to date and discussed in this chapter, as follows: (1) oxidation of benzyl alcohols and (2) oxidative coupling of amines, which are highly customizable on a case-by-case basis. Most importantly, the types of PS/CAT pairs in some of these MOFs affect the reaction mechanism and the catalytic results are specifically exemplified here. Additionally, Table 4 lists more reported examples.

The  $\text{NH}_2\text{-BDC}^{172-174}$  and TCPP<sup>175,176</sup> linker-based MOFs with PS/CAT pairs at the linker and SBU (type I) are well known in catalyzing the oxidation reactions of alcohols and amines under visible light. For example, Li and co-workers<sup>173</sup> reported the oxidation reactions of a series amines to imines with conversion yields of around 41–99% and selectivity of around

45–90% using molecular  $\text{O}_2$  as an oxidant over the  $\text{NH}_2\text{-MIL-125(Ti)}$  MOF under visible light irradiation. According to the experimental observation and ESR studies, the authors proposed that the Ti(IV) center of the SBU is initially photoreduced to Ti(III) via LMCT, and then the reduced species transfers the electron to  $\text{O}_2$  to form  $\text{O}_2^{\cdot-}$ , which then further reacts with the C-centered radical originating from the amines to produce the imine via subsequent steps (Fig. 15a). A similar photocatalytic mechanism for the visible light-driven oxidative coupling of amines was proposed by Niu *et al.* when working with the innovative MOF  $\text{NaRh-SiW}_{12}$ , a POM node-based crystalline MOF comprised of a paddlewheel  $\text{Rh}_2(\text{OAc})_4$  linker.<sup>177</sup> In general, POMs are reported to be good CATs for promoting  $\text{O}_2$  reduction into  $\text{O}_2^{\cdot-}$  within MOFs.<sup>128,178</sup> In particular, the  $\text{NaRh-SiW}_{12}$  MOF reported by Niu achieved a yield of 96.1% in photocatalytic imine production with TON of 480.5 and it was much more active than individual  $\text{Rh}_2(\text{OAc})_4$  or POMs.<sup>177</sup> In a separate work, Zhou *et al.* reported a TCPP-based MOF (namely, PCN 22) comprised of a Ti(IV) SBU for the photocatalytic alcohol oxidation reaction with TEMPO (2,2,6,6-tetramethylpiperidinyloxy) as an additional oxidant.<sup>175</sup> The PCN-22/TEMPO system achieved 28% conversion in 2 h with almost 100% selectivity for the corresponding benzaldehydes. The author proposed that the TCPP linkers in the MOF are



**Fig. 15** (a) Proposed mechanism of photocatalytic amine oxidation over  $\text{NH}_2\text{-MIL-125(Ti)}$ . Adapted with permission from ref. 173. Copyright 2015, Elsevier. (b) Proposed mechanism for PCN-22/TEMPO system. Adapted with permission from ref. 175. Copyright 2015, the Royal Society of Chemistry. (c) Illustration of simultaneous proton reduction and selective benzylamine oxidation over Pt/PCN-777 by photocatalysis. Adapted with permission from ref. 182. Copyright 2018, WILEY-VCH Verlag GmbH & Co. (d) Proposed mechanism for photocatalytic coupling of amine by the  $\text{UiO-66-NH}_2$  under anaerobic condition. Adapted with permission from ref. 174. Copyright 2019, Elsevier.



excited by visible light, followed by electron injection into the  $\text{Ti}_7\text{O}_6$  clusters to yield  $[\text{TCPP}]^+$ . Meanwhile, TEMPO is oxidized to  $\text{TEMPO}^+$  by  $[\text{TCPP}]^+$ , which selectively oxidizes the alcohol to aldehyde by a two-electron transfer mechanism (Fig. 15b). This mechanism is claimed to be similar to the dye-sensitized mechanism in a dye/ $\text{TiO}_2$ /TEMPO system.<sup>179</sup>  $\text{Br}^-$  is another example of a co-catalyst used by Wei *et al.* in the  $\text{NH}_2\text{-MIL-125}$  ( $\text{Ti}$ )/ $\text{NaBr}$  system, which facilitated the oxidation of alcohols to their corresponding carboxylic acids.<sup>180</sup> This system is versatile, efficiently converting a wide range of substrates, including both aliphatic and aromatic alcohols. The process involves a photoinduced single-electron transfer (SET) from  $\text{Br}^-$  to  $\text{NH}_2\text{-MIL-125}$  ( $\text{Ti}$ ), generating highly reactive bromine radical species. These species significantly enhance the photocatalytic activity for the oxidation of alcohols to acids. The oxidative transformation of alcohols and amines under anaerobic conditions is often overlooked during HER/ $\text{CO}_2$ RR processes. However, various groups recently reported MOF systems capable of simultaneously producing both oxidized and reduced products.<sup>174,181</sup> For instance, Jiang and co-workers employed a Pt-loaded type I-MOF (namely PCN-777) as an innovative platform to simultaneously produce specific imines ( $486 \mu\text{mol g}^{-1} \text{h}^{-1}$ , almost 100% selectivity) and  $\text{H}_2$  ( $332 \mu\text{mol g}^{-1} \text{h}^{-1}$ ), which were intrinsically separated in the solution and gas phase, respectively (Fig. 15c).<sup>182</sup> PCN-777 is composed of  $\text{Zr}_6$ -based SBU and 4,4',4''-(1,3,5-triazine-2,4,6-triyl) tribenzoic acid ( $\text{H}_3\text{TATB}$ ) linker. The linker is an expanded  $\pi$ -conjugated unit and improves the charge separation. Pt was encapsulated as nanoparticles to serve as a cocatalyst for  $\text{H}_2$  generation in the Pt/PCN 777 system. As a plausible mechanism for the oxidative coupling process of benzyl amine, the authors stated that the catalytic HER site is fed by a proton transfer (PT) process similar to a previously reported example,<sup>174</sup> while the photogenerated holes on the HOMO of MOFs activate benzylamine to the carbocationic species  $\text{PhCH}_2\text{NH}_2^+$ . The resulting intermediates are further coupled with the unreacted benzylamine to form the target product *N*-benzylbenzaldimine (Fig. 15d). Recent advances in MOFs have led to the development of mesoporous, photoactive MOFs, such as LTG-NiRu, reported by Bai *et al.*<sup>183</sup> This MOF, constructed from a  $[\text{Ru}(\text{phen})_3]^{2+}$ -derived metalloligand (L4) linker and  $\text{Ni}^{2+}$  nodes, featured highly stable 1D channels with a pore diameter of 2.1 nm. LTG-NiRu exhibited exceptional catalytic activity in the aerobic photocatalytic oxidative coupling of amine derivatives, achieving nearly 100% conversion of benzylamines within 1 h under visible light. Moreover, LTG-NiRu was experimentally validated for its high stability, excellent reusability, and effectiveness in synthesizing over 20 chemical products through oxidative cycloaddition, demonstrating its potential for gram-scale synthesis.

The Lin group developed a UiO-67 MOF, named  $\text{Zr}_6\text{-Cu/Fe-1}$  with a covalently integrated PS/CAT pair  $[\text{Cu}^I(5,5'\text{-dcbpy})(\text{dppe})](\text{PF}_6)/[\text{Fe}^{\text{III}}(5,5'\text{-dcbpy})(\text{OH})]\text{Cl}_2$  (type II according to the classification in Fig. 5). A dual photocatalytic cycle for the aerobic oxidation of benzyl alcohol is proposed and depicted in Fig. 16a.<sup>184</sup> Upon photoirradiation, the  $[\text{Cu}(\text{i})]\text{-PS}$  in the

MOF is first excited to  $[\text{Cu}]^*$ , which is subsequently oxidized by  $\text{O}_2$  to generate  $\text{O}_2^{\cdot-}$  and  $[\text{Cu}(\text{u})]$ . The strongly oxidizing  $[\text{Cu}(\text{u})]$  efficiently oxidizes  $[\text{Fe}(\text{m})\text{-OH}]$ , which is formed by the deprotonation of  $\text{H}_2\text{O}$  on the acidic  $\text{Fe}(\text{m})$  center to generate the highly reactive  $\cdot\text{OH}$ . Through hydrogen atom transfer (HAT),  $\cdot\text{OH}$  rapidly oxidizes the alcohol to generate alkoxy radical species as the key intermediate, which subsequently transforms into the aldehyde product. In the presence of  $\text{H}_2\text{O}$ , the generated  $[\text{Fe}(\text{m})]$  undergoes hydrolysis to afford  $[\text{Fe}(\text{m})\text{-OH}]$  for the next oxidation cycle. A dual photocatalytic cycle is also noticed in several MOFs (see Table 4)<sup>178,185-193</sup> containing an excited triplet state dominant organic/metalloligand linker, providing an additional photocatalytic channel for producing  $^1\text{O}_2$  *via* energy transfer and oxygen sensitization. For example, Jin and co-workers integrated an electron donor 5,15-di(*p*-benzoato)porphyrin ( $\text{H}_2\text{DPBP}$ ) as a linker into a naphthalene diimide (electron acceptor)-based Zr-MOF (Zr-NDI) to construct the mixed-linker MOF Zr-NDI- $\text{H}_2\text{DPBP}$ , which benefits from the two linkers with similar geometry and connectivity.<sup>190</sup> The resultant mixed-linker MOF enabled photocatalytic aerobic oxidative coupling of benzylamine to imine at a rate of  $136 \text{ mmol g}^{-1} \text{ h}^{-1}$ . The authors demonstrated with experiments and DFT calculations that this specific MOF uses both the electron transfer and energy transfer cascade (Fig. 16b) to transform  $\text{O}_2$  to  $\text{O}_2^{\cdot-}$  and  $^1\text{O}_2$ , respectively. Consequently, it was possible to oxidize benzylamine to  $\text{PhCH}_2\text{NH}_2^+$ , which then reacts further with ROS to yield the respective imine. By applying the mixed-linker strategy, a pillared-layer Zn-MOF (MOF-LS10) was constructed using 2,3,5,6-tetrakis(4-carboxyphenyl)pyrazine ( $\text{H}_4\text{TCPP}$ ) and 2,5-di(pyridin-4-yl)thiazolo[5,4-*d*]thiazole (DPTTZ).<sup>194</sup> Unlike previous examples, MOF-LS10 offers a single photocatalytic channel through an electron transfer process that generates  $\text{O}_2^{\cdot-}$  radicals, facilitating the benzylamine coupling reaction under visible light irradiation. The control experiment with its isoreticular MOF-LS11 (constructed using BTEB<sup>4-</sup> and DPTTZ,  $\text{H}_4\text{BTEB} = 1,2,4,5$ -tetrakis(4-carboxyphenyl)benzene) and MOF-LS12 (constructed using TCPP<sup>4-</sup> and DPB,  $\text{DPB} = 1,4$ -di(pyridin-4-yl)benzene) showed that the photocatalytic amine coupling activity followed the order of MOF-LS10 > MOF-LS11 > MOF-LS12, demonstrating the synergistic role of the pyrazine and TZTZ structural units in MOF-LS10.

Fe-based SACs within the light-absorbing porphyrin scaffold of PCN 224 MOF (type IV) provide another specific route to convert alcohol into aldehyde and accelerate the oxidation kinetics (Fig. 17a).<sup>195</sup> The  $\text{Fe}^{3+}/\text{Fe}^{2+}$  pair facilitates the generation of ROS (e.g.,  $\text{O}_2^{\cdot-}$  and  $\cdot\text{OH}$ ) from inactive  $\text{H}_2\text{O}_2$  by a light-driven Fenton-like free-radical chain mechanism. However, the role of the  $\text{Fe}^{3+}$  sites in the photocatalytic oxidation reaction varies.<sup>87,196</sup> Recently, Jiang and co-workers reported the synthesis of a MOF (namely, Fe-Uio-66) PS/CAT pair by incorporating  $\text{Fe}^{3+}$  into  $\text{Zr}_6$  clusters (type IV, Fig. 17b).<sup>87</sup> As established from experimental and *in situ* EPR studies, newly built  $\text{FeO}_x\text{-Zr}_6$  clusters not only enhanced the light harvesting capacity and but also promoted  $\cdot\text{OH}$  and  $\text{O}_2^{\cdot-}$  formation at the  $\text{FeO}_x$  and  $\text{Zr}_6$  clusters, respectively, *via* the metal-



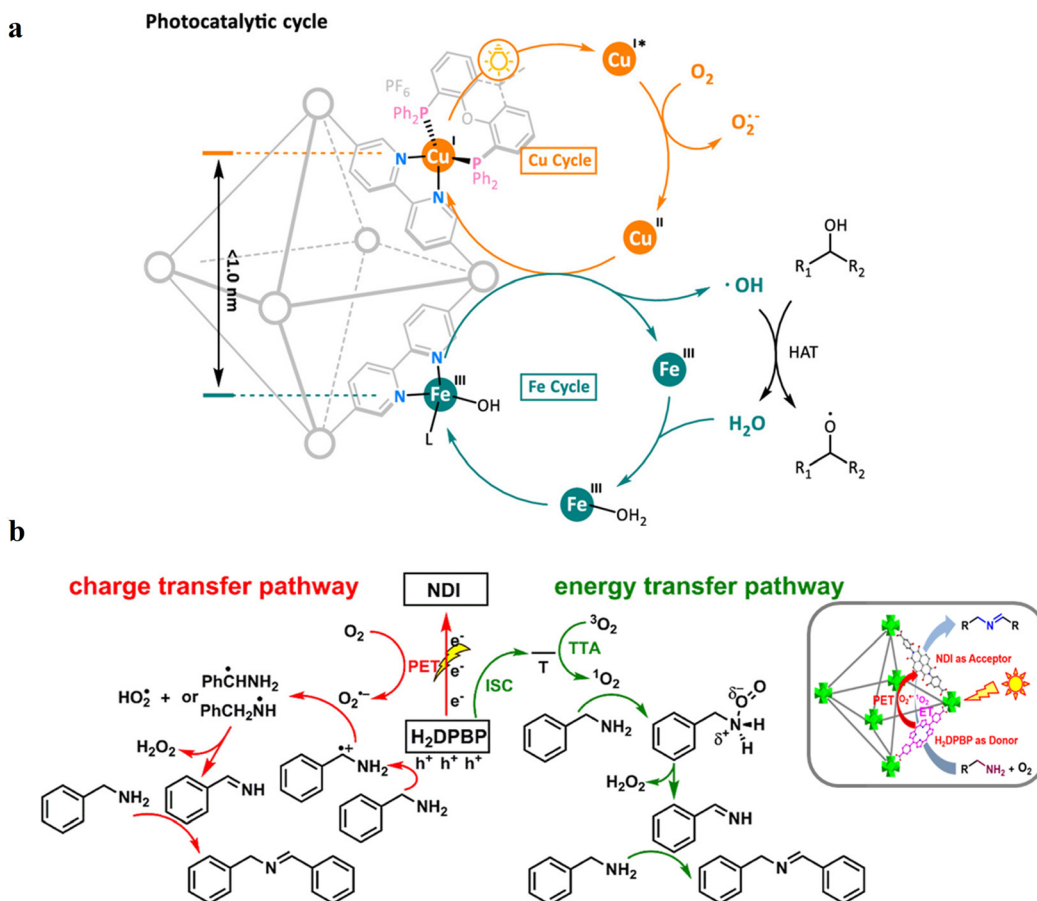


**Fig. 16** (a) Proposed mechanism for the photocatalytic aerobic oxidation of alcohols to generate alkoxyl radicals with  $Zr_6\text{-Cu/Fe-1}$ . Adapted with permission from ref. 184. Copyright 2021, the American Chemical Society. (b)  $Zr\text{-NDI-H}_2\text{DPBP}$  as mixed-linker donor ( $H_2\text{DPBP}$ ) and acceptor (NDI)-based MOF model, and their photoinduced electron transfer (PET) process involved in photocatalytic oxidative coupling of amines. Adapted with permission from ref. 190. Copyright 2023, the American Chemical Society.

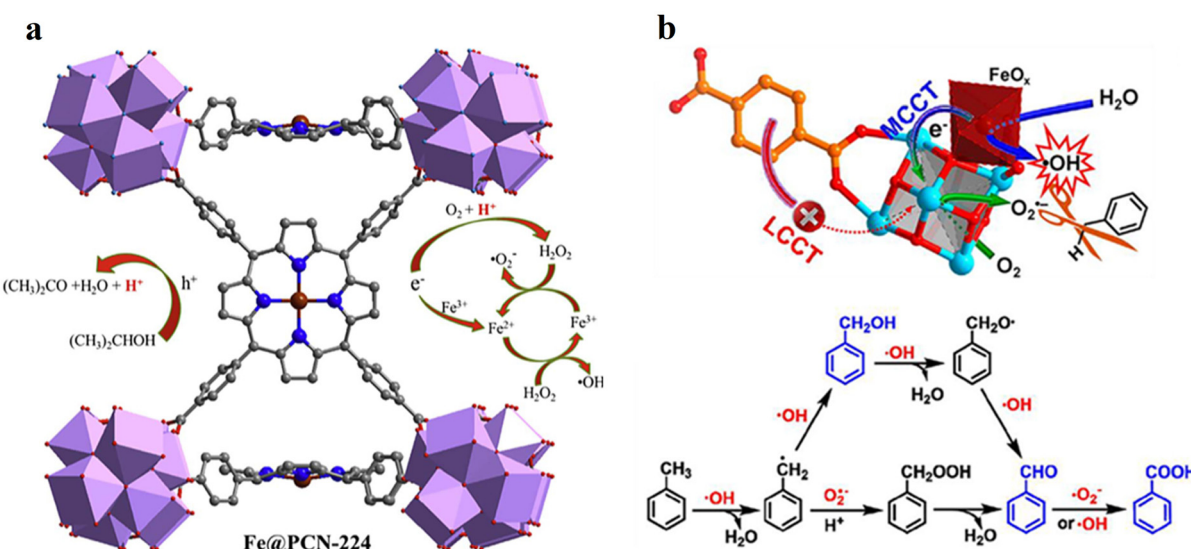


**Fig. 17** (a) Proposed mechanism of oxygen-related radical generation in photocatalytic systems with  $Fe\text{@PCN-224}$ . Adapted with permission from ref. 195. Copyright 2018, Elsevier. (b) Schematic illustration showing the conversion of  $H_2O$  to  $\cdot OH$  by visible light-driven MCCT process over Fe-doped  $UiO\text{-66}$  and proposed catalytic mechanism of toluene oxidation. Adapted with permission from ref. 87. Copyright 2019, the American Chemical Society.

to-cluster charge transfer (MCCT) pathway. The key role of this  $\cdot\text{OH}$  is to activate the unreactive C–H bonds of toluene to form benzyl radicals in the first step and promote the oxidation of benzaldehyde in the later stage to benzylic acid. Moreover, ROS generation *via* different types of photocatalytic channels and their role in catalytic oxidation reaction are also reflected in type V-MOFs such as  $[\text{Ru}(\text{bpy})_3]^{2+}$  encapsulated MIL-125-NH<sub>2</sub>,<sup>197</sup> and even in more complex systems such as Cu(I)W-DPNDI (see Table 4).<sup>198</sup>

## 5. Stability of MOFs – reuse, repair and recycle

The structural stability of the natural photosynthetic apparatus, specifically the individual molecular reactive sites and their macromolecular scaffold, represents the basis for achieving continuous photoactivity. Even under varying photon flux, temperature, *etc.*, it guarantees light absorption-induced charge separation, electron transport, and catalytic turnover for water splitting. Nevertheless, even the precisely tuned natural photosynthetic apparatus suffers from light-induced degradation but repair processes allow the recovery of its initial photoactivity.<sup>199</sup> In contrast, most molecular components degrade easily under homogeneous conditions and they are not easily recoverable and reusable in the homogenous state. Additionally, besides some specific examples, repair processes are not known.<sup>200</sup> Due to the integration of molecular components into large scaffolds, MOF-architectures offer great potential for stability improvement, recycling and repairing of the active components. In terms of recycling, MOFs offer the benefit of heterogeneous (photo)catalysts, given that they can be centrifuged or filtered from the reaction mixture and be reused in a new round of catalysis. Commonly, “digesting” and “chemical recycling” are performed to regenerate the MOFs.<sup>201</sup> Alternatively, the so-called heterogeneous MOF material can be embedded in a flow-reactor and be operative in continuous flow.<sup>202–204</sup> Of course, the reuse of MOFs in (photo)catalysis is only worthy when the active functional

units remain intact. Given that the 3D-structure of MOFs has a coordination framework, which provides some protection against the undesirable dimerization, aggregation and decomposition of the active molecular units, MOFs are ideal to provide stable and reusable (photo)catalysts. Some reported examples of MOFs surpassing molecular homogeneous catalysis systems in terms of stability are outlined in the following section.

### 5.1. Stabilization of photosensitizers

The reduced species  $[\text{Ru}(\text{bpy})_3]^{+}$ , generated from  $[\text{Ru}(\text{bpy})_3]^{2+}$  *via* reductive quenching, can lose a bipyridine (bpy) ligand over extended periods in solution unless faster electronic communication occurs with an electron-accepting CAT.<sup>205,206</sup> This issue can be circumvented in MOF-supported photocatalysis. In a recent study, Solé-Daura *et al.* encapsulated the  $[\text{PW}_{12}\text{O}_{40}]^{3-}$  (PW<sub>12</sub>) POM in a  $[(\text{Cp}^*)\text{Rh}(\text{bpydc})\text{Cl}]^{+}$ -functionalized UiO-67 MOF and demonstrated CO<sub>2</sub>RR in the presence of TEOA as a sacrificial donor. This study revealed that the encapsulated POMs act as efficient electron reservoirs, reacting with the photochemically reduced  $[\text{Ru}(\text{bpy})_3]^{+}$  and transferring electrons to the Rh CAT integrated in the MOF. This process favors the regeneration of the oxidized PS over its unproductive degradation, thereby boosting the TONs of the photocatalytic system.<sup>207</sup> Cu<sup>1</sup>-based PS with the general formula  $[\text{Cu}(\text{PP})(\text{NN})]^{+}$  (PP = diphosphine and NN = diimine derivatives) tend to dissociate into a homoleptic  $[\text{Cu}^1(\text{NN})_2]^{+}$  species in homogenous solution when irradiated.<sup>208</sup> Recently, Lin *et al.* showed that the deactivation of molecular  $[\text{Cu}(\text{Me}_2\text{PT})(\text{dppe})]\text{PF}_6$  occurs rapidly during HER with  $[\text{Co}(\text{phen})\text{Cl}_2]$  as the molecular CAT.<sup>75</sup> Experimentally, this was based on time-dependent and decreasing H<sub>2</sub> production and a rapid reduction of the MLCT band of  $[\text{Cu}(\text{Me}_2\text{PT})(\text{dppe})]\text{PF}_6$  upon irradiation (Fig. 18). However, when the respective molecular entities ( $[\text{Cu}(\text{PT})(\text{dppe})]\text{PF}_6$  and  $[\text{Co}(\text{PT})\text{Cl}_2]$ ) were assembled in a Zr<sub>6</sub>-based dual MOF, namely mPT-Cu/Co, it not only yielded an impressive TON of 18 700 (~95 times higher) in comparison to its homogenous control under identical conditions but also showed recyclability for three consecutive runs without a sig-

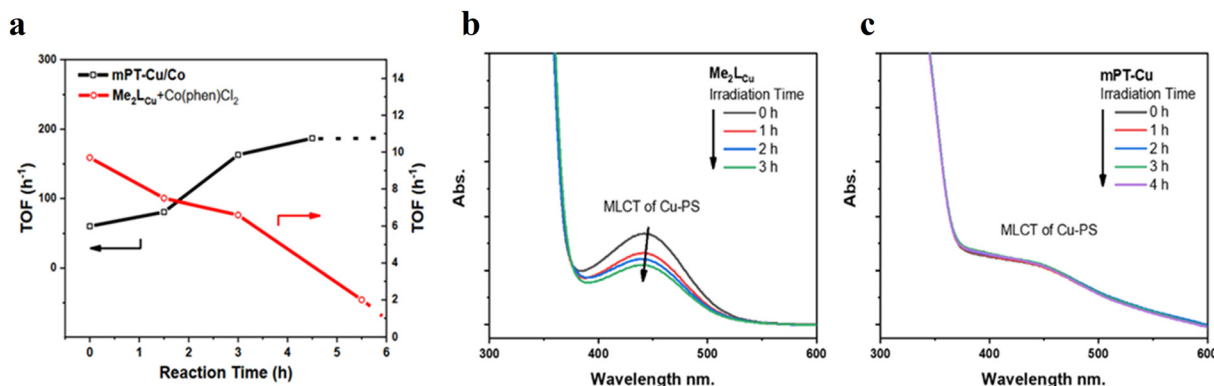


Fig. 18 (a) Time-dependent TOF curves of mPT-Cu/Co (black) and  $\text{Me}_2\text{L}_{\text{Cu}} + \text{Co}(\text{phen})\text{Cl}_2$  (red) in the first 5 h of photocatalytic HER, where  $\text{Me}_2\text{L}_{\text{Cu}}$  is  $[\text{Cu}(\text{Me}_2\text{PT})(\text{dppe})]\text{PF}_6$ , and UV-vis absorption changes for  $\text{Me}_2\text{L}_{\text{Cu}}$  (b) and mPT-Cu (c) under catalytic HER conditions ( $\text{N}_2$  atmosphere,  $\text{CH}_3\text{CN} : \text{AcOH} = 1.97 : 0.03$ ) at different irradiation times. Adapted with permission from ref. 75. Copyright 2020, the American Chemical Society.



nificant decrease in activity. The underlying reason for the repeated high photoactivity is assumed to rely on the maintained crystallinity of mPT-Cu/Co during HER as obtained from the powder X-ray diffraction (PXRD) studies and inductively coupled plasma mass spectrometry (ICP-MS), which revealed <1.4% Cu and <0.1% Co leached in the supernatant.

## 5.2. Stabilization of molecular catalysts

Using [FeFe]-hydrogenase mimics, an often-observed side reaction in homogeneous systems is the dimerization or tetramerization of [FeFe]-centers due to the de-coordination of the bridging sulfur ligand (Fig. 19a).<sup>209,210</sup> The [FeFe]-hydrogenase active site model complex has been employed in various types of MOFs and achieved a significant improvement in HER activity under irradiation in comparison to their homogeneous control.<sup>77,83,139,142,143,211</sup> In an exemplary study (Fig. 19b),<sup>142</sup> IR investigations after the ceased H<sub>2</sub> catalysis revealed that the majority of the [FeFe] active sites were still structurally intact. Furthermore, it was hypothesized that only the surface-exposed [FeFe] centers were active in photocatalysis. In a follow-up study,<sup>143</sup> it was shown that the photocatalytic HER activity from a suspension of UiO-66-[FeFe](dcbd)(CO)<sub>6</sub> in a solution of [Ru(bpy)<sub>3</sub>]<sup>2+</sup> and ascorbate could be recovered after 60 min of stirring by replacing mainly the PS-electron donor solution, which indicated that mainly the molecular homogeneous PS is not recyclable, not the CAT. Similarly, for another Fe-based system (but not hydrogenase mimic), the authors reported the prevention of active Fe-site aggregation in a series of bifunctional Fe-X@Zr<sub>6</sub>-Cu MOFs (X = Br<sup>-</sup>, Cl<sup>-</sup>, AcO<sup>-</sup> and BF<sub>4</sub><sup>-</sup>) comprised of Cu-PSS and catalytic Fe(II) supported

on SBUs for photocatalytic H<sub>2</sub> evolution (Fig. 19c).<sup>71</sup> The prevention of dimerization is also relevant in [M(NN)(CO)<sub>3</sub>X] CATs for CO<sub>2</sub> reduction (M = Mn, Re). These systems are well-characterized in homogeneous solution but deactivation *via* dimerization is a common side reaction in these catalytic processes.<sup>145,212,213</sup> Heterogenizing these molecular CATs in MOFs enables their spatial isolation to be maintained, leading to the significant inhibition of dimer formation, and thus prolonged stability of the CAT, resulting in a higher TON and prolonged catalytic activity.<sup>213,214</sup> For example, Li *et al.* combined an [Ru(bpy)<sub>3</sub>]<sup>2+</sup>/[Re(bpy)(CO)<sub>3</sub>X] pair within a MOF (Ru-MOF-253-Re) comprised of Al(III)-based SBUs and 5,5'-dcbpy linkers.<sup>214</sup> ICP analysis revealed that only 1.6% of the incorporated Re leached from the solid MOF in the solution, presenting indirect evidence that dimerization was significantly hampered inside the MOF.

## 5.3. Repair of active molecular units in MOF

In terms of reusing MOFs for catalysis, the most problematic issue that arises with most innovative MOF systems is the potential deactivation of CAT or PS after photolysis and due to diffusive loss.<sup>215</sup> As discussed above, nature also teaches mankind that even the most sophisticated systems may suffer from unavoidable degradation,<sup>200</sup> and in this case, green plants have developed complex repair strategies. Thus, related strategies can possibly be applied in MOF-based photocatalytic systems to regenerate their active molecular unit. A respective self-healing strategy was recently reported for a platinum-based 5,5'-dcbpy system with an [Ir(bpy)(ppy)<sub>2</sub>]-type PS in an UiO-67-type MOF structure (namely, Pt<sub>n</sub>-Ir\_BUUiO) (Fig. 20a).<sup>216</sup>

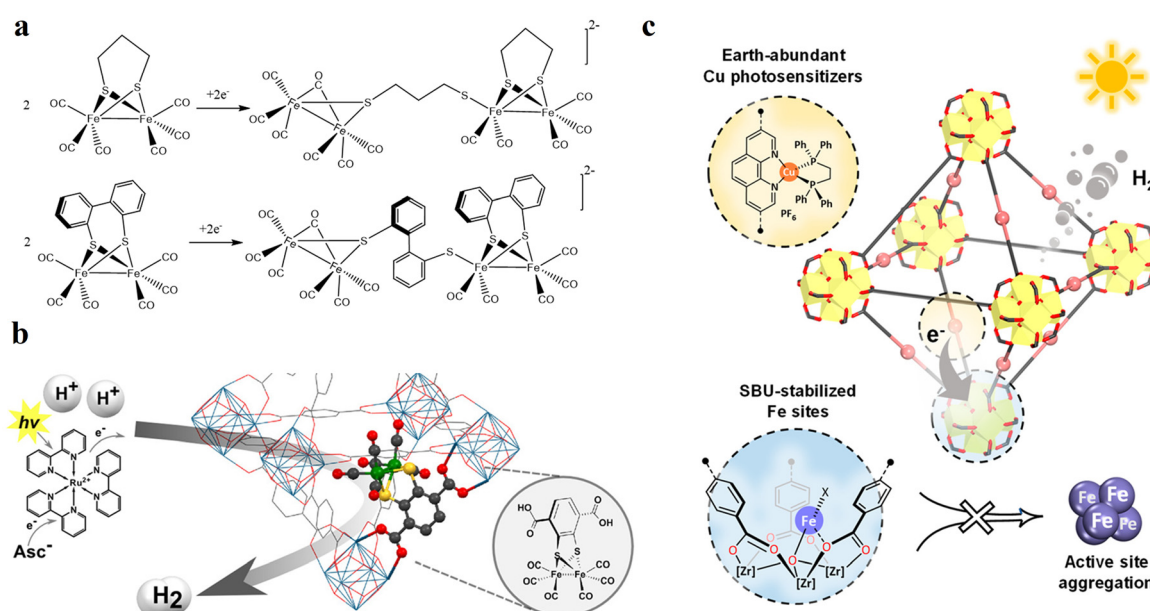


**Fig. 19** (a) Dimerization of one-electron reduced model complexes of the [FeFe]-hydrogenase active site, which can be prevented owing to their incorporation in MOFs.<sup>209,210</sup> (b) [FeFe] hydrogenase active site model complexes incorporated in an MOF (UiO-66-[FeFe](dcbd)(CO)<sub>6</sub>) with aq. [Ru(bpy)<sub>3</sub>]<sup>2+</sup> and ascorbate for the photocatalytic reduction of protons. Adapted with permission from ref. 142. Copyright 2013, the American Chemical Society. (c) Schematic illustration of Fe-X@Zr<sub>6</sub>-Cu-catalyzed, visible light-driven HER and catalytic site stabilization *via* site isolation. Adapted with permission from ref. 71. Copyright 2020, the American Chemical Society.



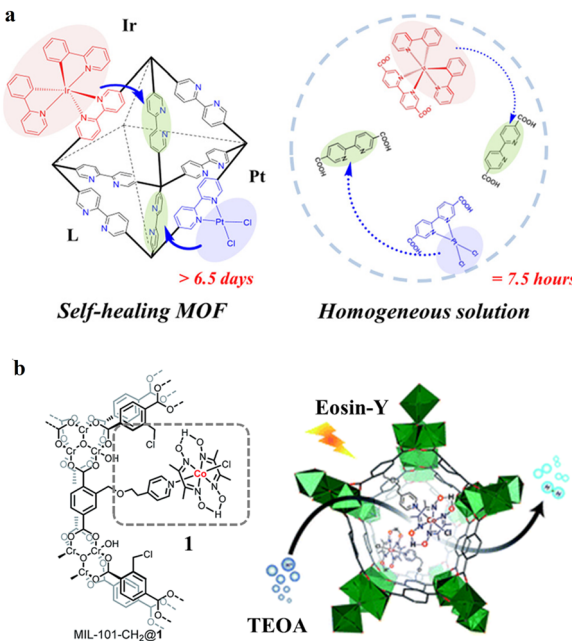


**Fig. 20** (a) Schematic operation principle of a self-healing MOF ( $\text{Pt}_n\text{-Ir-BUiO}$ ) and the corresponding homogeneous system. Adapted with permission from ref. 216. Copyright 2016, the American Chemical Society. (b) Post-synthetically incorporated molecular cobaloxime catalyst (1) on the aromatic rings of MIL-101(Cr) for photocatalytic proton reduction with Eosin-Y and TEOA. Adapted with permission from ref. 219. Copyright 2018, the Royal Society of Chemistry.

The authors successfully created a self-healing MOF catalyst by preventing the formation of colloidal platinum by increasing the ratio of 5,5'-dcbpy to platinum. This allowed the broken platinum-diimine bonds to re-form, thereby enabling continuous HER. In other examples with cobaloxime-based HER CATs (Fig. 20b), the integration of cobaloximes into the MOF framework showed the following benefit: it was reported from the homogeneous system that upon (light-driven) reduction, the cobaloxime CAT cobalt center dissociates from the ligands, followed by aggregation and deactivation to nanoparticles.<sup>217,218</sup> However, the incorporation of cobaloxime in the MIL-101(Cr) MOF architecture using the ship-in-a-bottle approach resulted in the effect that the dissociated ligand stayed close to the metal center and could re-coordinate, overall stabilizing the CAT. Additionally, the leaching was compensated by adding more cobaloxime, which restored the catalytic activity by up to 60% of that of the starting material.<sup>219</sup>

#### 5.4. Overall stability of MOF architecture

Besides a few robust MOF series such as UiO, ZIF, MIL, PCN, and NU, many MOFs have weak metal-linker coordination, which is prone to collapse in humid environments, both in the dark and under irradiation. This degradation leads to the loss of their modular structure, crystallinity, and more importantly, their active sites. From a fundamental perspective, MOFs with a low lattice energy are generally unstable in aqueous solutions. For instance, MOFs with dipolesitive metal ion SBUs such

as  $\text{Zn}^{2+}$ ,  $\text{Cu}^{2+}$ , and  $\text{Co}^{2+}$  are less stable compared to MOFs with SBUs carrying multiple positive charges, such as  $\text{Fe}_3$  in MIL-100 and MIL-101 or  $\text{Zr}_6$  in the UiO series, which exhibit much higher lattice energy and water stability.<sup>60</sup> Additionally, the higher degree of hydrolysis or solvolysis of the metal centers due to their Lewis acidity poses significant challenges for the long-term stability of MOFs in solvent environments.<sup>220,221</sup> Among the various strategies for increasing the overall stability linker modulation/design,<sup>222,223</sup> and post-synthetic modification has been used mostly in the context of photocatalytic reaction. One elegant example of the latter approach is the post-synthetic modification of a porphyrin titanium-based MOF (GIST-1) with various types of hydrophobic alkyl chains such as HPA (hexylphosphonic acid), DPA (dodecyl-phosphonic acid), and OPA (octadecylphosphonic acid).<sup>224</sup> These modifications do not alter the intrinsic structure of the frameworks but produce hydrophobic Ti-MOFs (HPA/DGIST-1, DPA/DGIST-1, and OPA/DGIST-1, respectively), which show higher activity in the selective reduction of  $\text{CO}_2$  to  $\text{HCOO}^-$  and improved stability in humid environments.

## 6. Conclusion and outlook

In summary, MOF architectures offer a combination of the benefits of modular and well-defined molecular CATs and PSs. This includes the ability to tailor the properties and enhance the (photo)activity of MOF by structurally altering their building blocks. Additionally, MOF architectures also provide the advantages of heterogeneous systems, such as stability, recyclability, and ease of handling. Currently, most MOFs in the field of artificial photosynthesis apply metal-oxo cluster-based SBUs (*e.g.* zirconium oxo-cluster) and the linkers are typically carboxylate species of porphyrin, bipyridine and others bearing sites for the coordinative attachment of PSs and CATs. Additionally, similar to natural enzymes, the pores within the structure of MOFs can provide active and selective reaction centers. Typically, the molecular properties of the individual building blocks such as light absorption and catalytic activity are maintained compared to homogeneous solution and the molecular entities often exhibit diminished degradation rates once incorporated in the MOF structure. Unlike standard heterogeneous catalysts, the activity of MOFs is not limited to their surface, but the entire coordination network provides pores with (photo)active reaction sites. Depending on the desired topology, 2-dimensional and 3-dimensional structures can be constructed, and based on the choice of CATs, which retain their reactivity pattern upon integration in MOFs, the knowledge-guided implementation of the desired light-driven catalytic conversions is possible. Moreover, by tuning the pore size of MOFs, the selectivity in catalysis can be tuned.

Although the close spatial proximity of the photo-active PS in the MOF structure can hinder light-driven conversions by inner filter effects and intermolecular annihilation deactivations in the excited states, the activity of MOFs is often higher than their homogeneous counterparts. Additionally, the het-



erogenization of the molecular units provides stability to the components and offers recyclability to quasi-molecular (photo)catalytic systems, which makes these MOFs an interesting class of materials.

In the future, even more sophisticated architectures will be possible, *e.g.*, potentially utilizing the fixed positioning of molecular CATs within the MOF framework to couple oxidative and reductive light-driven conversions similar to natural photosynthesis.

## Abbreviations

ABTC	3,3',5,5'-Azobenzenetetracarboxylate	H <sub>2</sub> DPBP	5,15-Di( <i>p</i> -benzoato)porphyrin
Ade	Adenine	4-HEP	4-(2-Hydroxyethyl)pyridine
BA	Benzoic acid	Hip	1 <i>H</i> -Imidazo[4,5- <i>f</i> ][1,10]phenanthroline
BDC/ <i>p</i> -BDC/	1,4-Benzenedicarboxylate/terephthalate	HTHATN	Hexathiohexaazatrinaphthylene
TPA		H <sub>2</sub> L1	2,2'-Bipyridine-4,4'-dibenzoic acid
Blm	Benzimidazolate	H <sub>2</sub> L2/H <sub>2</sub> L <sub>NN</sub>	(5,5'-Di(4-carboxyl-phenyl)-2,2'-bipyridine) or (4,4'-di(4-benzoato)-2,2'-bipyridine)
BNAH	1-Benzyl-1,4-dihydronicotinamide	H <sub>2</sub> L3	2"-([Azidomethyl]-[1,1':4',1":4",1""-quaterphenyl]-4,4"-dicarboxylic acid
BnNH <sub>2</sub>	Benzyl amine	H <sub>3</sub> L4	4-(1 <i>H</i> -Imidazo[4,5- <i>f</i> ][1,10]phenanthrolin-2-yl)benzoic acid
BnOH	Benzyl alcohol	H <sub>2</sub> L6	Bis(3,5-dicarboxyphenyl)pyridine
Bpdc	2,2'-Biphenyl dicarboxylate	H <sub>2</sub> L7	Tetrakis-3,5-bis[4-carboxyphenyl]phenylporphine
BPDC-(3,3'	3,3'-Diamino-1,1'-biphenyl-4,4'-dicarboxylate	H <sub>4</sub> L8	3,3',5,5'-Azoxybenzenetetracarboxylic acid
NH <sub>2</sub> ) <sub>2</sub>		H <sub>4</sub> L9	Tetracarboxylic acid from (2,6-dibromo-4-(trifluoromethyl)aniline and 3,5-bis(ethoxycarbonyl)-phenylboronic acid)
Bpy	2,2'-Bipyridine	H <sub>2</sub> NDI	Di-salicylic acid derivative of naphthalenediimides
bpydc = 5,5'-dcbpy	2,2'-Bipyridine-5,5'-dicarboxylate	H <sub>2</sub> PDI	Bis( <i>N</i> -carboxymethyl) peryleneimide
BTB	1,3,5-Benzenetribenzoate	H <sub>2</sub> Ph-Pz	1,4-Di(1 <i>H</i> -pyrazol-4-yl)benzene
Catbdc	2,3-Dihydroxyterephthalic acid	H <sub>2</sub> TCPP/	Tetrakis(4-carboxyphenyl)porphyrin
Cou6	Coumarin 6	H <sub>2</sub> TBP	
Cp*	$\eta_5$ -C <sub>5</sub> Me <sub>5</sub>	H <sub>4</sub> TCPP	2,3,5,6-Tetrakis(4-carboxyphenyl)pyrazine
	(1,2,3,4,5-pentamethylcyclopentadienyl)	H <sub>2</sub> TTA-6SH	2,4,6-Tris{4-[3,5-bis(mercaptopo)-4-carboxyphenyl]phenyl}-1,3,5-triazine
Cptpy	4'-{4-Carboxyphenyl}-terpyridine	H <sub>4</sub> TBAPy	1,3,6,8-Tetrakis( <i>p</i> -benzoic acid)pyrene
Cy*	<i>p</i> -Cymene	H <sub>4</sub> ptba	4,4',4",4""-(1,3,6,8-Pyrenetetrayltetra-2,1-ethylenediyi)tetraakis benzoic acid
Cyclam	1,4,8,11-Tetraazacyclotetradecane	KEX	Potassium ethyl xanthogenate
5,5'-dcbpy	2,2'-Bipyridine-5,5'-dicarboxylate	L5	N[(CH <sub>2</sub> ) <sub>2</sub> NHCH <sub>2</sub> (m-C <sub>6</sub> H <sub>4</sub> )CH <sub>2</sub> NH(CH <sub>2</sub> ) <sub>3</sub> N(E,E')-4,4'-Bis[ <i>p</i> -( <i>N,N</i> -dimethylamino)styryl]-2,2'-bipyridine
5,5'-dcppy	2-Phenylpyridine-5,5'-dicarboxylate	L10	2-(2,4-Difluorophenyl)-5-(trifluoromethyl)pyridine
DHBDC	2,5-Dihydroxy-1,4-bezenedicarboxylic acid	L <sub>CN</sub>	<i>N<sup>2</sup>,N<sup>2</sup>'-</i> Propanediylbis(2,3-butanedione 2-imine 3-oxime)
DIPEA	<i>N,N</i> -Diisopropylethylamine	L <sup>H</sup> <sub>2</sub>	2-(5'-Methyl-[2,2'-bipyridin]-5-yl)acetate
DMA	<i>N,N</i> -Dimethylaniline	MBA	2-Methyl imidazole
Dmbpy	4,4'-Dimethyl-2,2'-bipyridine	2-MIM	Methyl viologen
dmgH	Dimethylglyoxime	MV	2-Aminoterephthalate/2-aminobenzene-1,4-dicarboxylate
dppe	1,2-Bis(diphenylphosphanyl)ethane	NH <sub>2</sub> -BDC	5-Aminoisophthalate
dptz	Tetrazine derivative	NH <sub>2</sub> IPA	2'-Amino-[1,1':4,1"-terphenyl]-4,4"-dicarboxylate
DPTZTZ	2,5-Di(pyridin-4-yl)thiazolo[5,4- <i>d</i> ]thiazole	NH <sub>2</sub> -TPDC	Ionic liquid
EDTA	Ethylenediaminetetraacetic acid	N <sup>i</sup> Pr <sub>2</sub> EtH	Pyrenebutyric acid
Fe-TCBPP = Fe-TCPP	Iron 5,10,15,20-tetra[4-(4'-carboxyphenyl)phenyl]-porphyrin	PBA	9-Phenylcarbazole-3,6-dicarboxylic acid
H <sub>2</sub> bdt	1,4-Benzenedi(1 <i>H</i> -1,2,3-triazole)	PD	Bis(2-diphenylphosphino)phenyl ether
H <sub>2</sub> BPD-4F4TS	2,2',5,5'-Tetrafluoro-3,3',6,6'-tetrakis(2-thiophenethio)-4,4'-biphenyl dicarboxylic acid	POP	Polyoxometalates
H <sub>3</sub> BTC	Benzene1,2,4-tricarboxylic acid	POMs	Ppy
H <sub>2</sub> BIM	1,2-Bis((5 <i>H</i> -imidazol-4-yl)methylene)hydrazine	PrOH	2-Phenylpyridine
H <sub>2</sub> dcabd	1,4-Dicarboxylbenzene-2,3-dithiol	PT	Isopropanol
		Py	4,4'-{1,10-Phenanthroline-3,8-diyl)dibenzoate
		Qtpy	Pyridine
			4,4':2',2":4,4"-Quaterpyridine



TATB	4,4',4''-Triazine-2,4,6-triyl-tribenzoate
TCA	4,4',4''-Tricarboxyltriphenylamine
TCBQ	Tetrachlorobenzoquinone
TCPP/TBP	Tetrakis(4-carboxyphenyl)porphyrin
TEMPO	2,2,6,6-Tetramethylpiperidinyloxy
TFPP	5,10,15,20-Tetrakis-(2,3,4,5,6-pentafluorophenyl)-porphyrin
Terpy	2,2':6',2''-Terpyridine
TEOA	Triethanolamine
TET	Tetracene
THF	Tetrahydrofuran
TIB	1,3,5-Tris(1-imidazolyl) benzene
TP	Tris(4-(pyridin-4-yl)phenyl)amine
TPA	Tris(2-pyridylmethyl)amine
TPHN	(2''-Nitro[1,1':4',1''':4'',1'''-quaterphenyl]-4,4''-dicarboxylate)
TPP	Triphenylphosphine
Tp-PABA	Triformylphloroglucinol coupled <i>p</i> -aminobenzoate
TPPy	1,3,6,8-Tetra(pyridin-4-yl)pyrene
XantP	Dimethyl-4,5-bis(diphenylphosphino)xanthene

## Data availability

No primary research results, software or code has been included and no new data were generated or analysed as part of this review.

## Conflicts of interest

There are no conflicts to declare.

## Acknowledgements

A. P. is grateful for financial support by the Vector Stiftung (project number P2019-0110) and the Carl-Zeiss-Stiftung. The Deutsche Forschungsgemeinschaft (DFG) is gratefully acknowledged for financial support *via* TRR234 “CataLight” project number 364549901, (projects A1, A4, B8) and through the SPP2102, grant number 495050545. S. Y. is grateful to the Landesgraduiertenförderungsgesetzes (LGFG) Doctoral scholarships under the Postgraduate Scholarships Act of the Land of Baden-Wuerttemberg for financial support.

## References

- 1 D. G. Nocera, Solar Fuels and Solar Chemicals Industry, *Acc. Chem. Res.*, 2017, **50**, 616–619.
- 2 A. Galushchinskiy, R. González-Gómez, K. McCarthy, P. Farràs and A. Savateev, Progress in Development of Photocatalytic Processes for Synthesis of Fuels and Organic Compounds under Outdoor Solar Light, *Energy Fuels*, 2022, **36**, 4625–4639.
- 3 A. Pannwitz, D. M. Klein, S. Rodríguez-Jiménez, C. Casadevall, H. Song, E. Reisner, L. Hammarström and S. Bonnet, Roadmap towards solar fuel synthesis at the water interface of liposome membranes, *Chem. Soc. Rev.*, 2021, **50**, 4833–4855.
- 4 C. K. Prier, D. A. Rankic and D. W. C. MacMillan, Visible Light Photoredox Catalysis with Transition Metal Complexes: Applications in Organic Synthesis, *Chem. Rev.*, 2013, **113**, 5322–5363.
- 5 T. Kanda, K. Saito and H. Ishikita, Mechanism of Mixed-Valence  $\text{Fe}^{2.5+} \dots \text{Fe}^{2.5+}$  Formation in  $\text{Fe}_4\text{S}_4$  Clusters in the Ferredoxin Binding Motif, *J. Phys. Chem. B*, 2022, **126**, 3059–3066.
- 6 J. K. Bindra, J. Niklas, Y. Jeong, A. W. Jasper, M. Kretzschmar, J. Kern, L. M. Utschig and O. G. Poluektov, Coherences of Photoinduced Electron Spin Qubit Pair States in Photosystem I, *J. Phys. Chem. B*, 2023, **127**, 10108–10117.
- 7 H. Dau and I. Zaharieva, Principles, Efficiency, and Blueprint Character of Solar-Energy Conversion in Photosynthetic Water Oxidation, *Acc. Chem. Res.*, 2009, **42**, 1861–1870.
- 8 J. Duan, S. Mebs, K. Laun, F. Wittkamp, J. Heberle, T. Happe, E. Hofmann, U.-P. Apfel, M. Winkler, M. Senger, M. Haumann and S. T. Stripp, Geometry of the Catalytic Active Site in [FeFe]-Hydrogenase Is Determined by Hydrogen Bonding and Proton Transfer, *ACS Catal.*, 2019, **9**, 9140–9149.
- 9 O. Lampret, J. Duan, E. Hofmann, M. Winkler, F. A. Armstrong and T. Happe, The roles of long-range proton-coupled electron transfer in the directionality and efficiency of [FeFe]-hydrogenases, *Proc. Natl. Acad. Sci. U. S. A.*, 2020, **117**, 20520–20529.
- 10 H. Dau and I. Zaharieva, Principles, Efficiency, and Blueprint Character of Solar-Energy Conversion in Photosynthetic Water Oxidation, *Acc. Chem. Res.*, 2009, **42**, 1861–1870.
- 11 J. M. Lehn and J. P. Sauvage, Chemical storage of light energy—catalytic generation of hydrogen by visible-light or sunlight—irradiation of neutral aqueous-solutions, *New J. Chem.*, 1977, **1**, 449–451.
- 12 J. H. Montoya, L. C. Seitz, P. Chakthranont, A. Vojvodic, T. F. Jaramillo and J. K. Nørskov, Materials for solar fuels and chemicals, *Nat. Mater.*, 2017, **16**, 70–81.
- 13 J. L. White, M. F. Baruch, J. E. Pander, Y. Hu, I. C. Fortmeyer, J. E. Park, T. Zhang, K. Liao, J. Gu, Y. Yan, T. W. Shaw, E. Abelev and A. B. Bocarsly, Light-Driven Heterogeneous Reduction of Carbon Dioxide: Photocatalysts and Photoelectrodes, *Chem. Rev.*, 2015, **115**, 12888–12935.
- 14 T. Hisatomi, J. Kubota and K. Domen, Recent advances in semiconductors for photocatalytic and photoelectrochemical water splitting, *Chem. Soc. Rev.*, 2014, **43**, 7520–7535.
- 15 Z. Jiang, Y. Tang, Q. Tay, Y. Zhang, O. I. Malyi, D. Wang, J. Deng, Y. Lai, H. Zhou, X. Chen, Z. Dong and Z. Chen,



Understanding the Role of Nanostructures for Efficient Hydrogen Generation on Immobilized Photocatalysts, *Adv. Energy Mater.*, 2013, **3**, 1368–1380.

16 X. Li, J. Yu and M. Jaroniec, Hierarchical photocatalysts, *Chem. Soc. Rev.*, 2016, **45**, 2603–2636.

17 A. Corma and H. Garcia, Zeolite-based photocatalysts, *Chem. Commun.*, 2004, 1443.

18 Y. Yuan, N. Jin, P. Saghy, L. Dube, H. Zhu and O. Chen, Quantum Dot Photocatalysts for Organic Transformations, *J. Phys. Chem. Lett.*, 2021, **12**, 7180–7193.

19 H. Kumagai, Y. Tamaki and O. Ishitani, Photocatalytic Systems for CO<sub>2</sub> Reduction: Metal-Complex Photocatalysts and Their Hybrids with Photofunctional Solid Materials, *Acc. Chem. Res.*, 2022, **55**, 978–990.

20 K. E. Dalle, J. Warnan, J. J. Leung, B. Reuillard, I. S. Karmel and E. Reisner, Electro- and Solar-Driven Fuel Synthesis with First Row Transition Metal Complexes, *Chem. Rev.*, 2019, **119**, 2752–2875.

21 B. Zhang and L. Sun, Artificial photosynthesis: opportunities and challenges of molecular catalysts, *Chem. Soc. Rev.*, 2019, **48**, 2216–2264.

22 X.-L. Yang, J. Hu, H. Zhong, Q.-C. Lin, Z. Lin, L.-H. Chung and J. He, Building metal-thiolate sites and forming heterojunction in Hf- and Zr-based thiol-dense frameworks towards stable integrated photocatalyst for hydrogen evolution, *Chin. Chem. Lett.*, 2024, 110120.

23 L. Tang, Q. Lin, Z. Jiang, J. Hu, Z. Liu, W. Liao, H. Zhou, L. Chung, Z. Xu, L. Yu and J. He, Nanoscaling and Heterojunction for Photocatalytic Hydrogen Evolution by Bimetallic Metal–Organic Frameworks, *Adv. Funct. Mater.*, 2023, **33**, 2214450.

24 J. Schild, B. Reuillard, A. Morozan, P. Chenevier, E. Gravel, E. Doris and V. Artero, Approaching Industrially Relevant Current Densities for Hydrogen Oxidation with a Bioinspired Molecular Catalytic Material, *J. Am. Chem. Soc.*, 2021, **143**, 18150–18158.

25 S. Ren, D. Joulié, D. Salvatore, K. Torbensen, M. Wang, M. Robert and C. P. Berlinguette, Molecular electrocatalysts can mediate fast, selective CO<sub>2</sub> reduction in a flow cell, *Science*, 2019, **365**, 367–369.

26 H. Rao, L. C. Schmidt, J. Bonin and M. Robert, Visible-light-driven methane formation from CO<sub>2</sub> with a molecular iron catalyst, *Nature*, 2017, **548**, 74–77.

27 M. Lämmle, A. K. Mengelé, G. E. Shillito, S. Kupfer and S. Rau, Stability of Catalytic Centres in Light-Driven Hydrogen Evolution by Di- and Oligonuclear Photocatalysts, *Chem. – Eur. J.*, 2023, **29**, e20220272.

28 J. Odrobina, J. Scholz, A. Pannwitz, L. Francàs, S. Dechert, A. Llobet, C. Jooss and F. Meyer, Backbone Immobilization of the Bis(bipyridyl)pyrazolate Diruthenium Catalyst for Electrochemical Water Oxidation, *ACS Catal.*, 2017, **7**, 2116–2125.

29 A. K. Vannucci, L. Alibabaei, M. D. Losego, J. J. Concepcion, B. Kalanyan, G. N. Parsons and T. J. Meyer, Crossing the divide between homogeneous and heterogeneous catalysis in water oxidation, *Proc. Natl. Acad. Sci. U. S. A.*, 2013, **110**, 20918–20922.

30 M. R. Norris, J. J. Concepcion, Z. Fang, J. L. Templeton and T. J. Meyer, Low-Overpotential Water Oxidation by a Surface-Bound Ruthenium-Chromophore-Ruthenium-Catalyst Assembly, *Angew. Chem., Int. Ed.*, 2013, **52**, 13580–13583.

31 L. Alibabaei, M. K. Brenneman, M. R. Norris, B. Kalanyan, W. Song, M. D. Losego, J. J. Concepcion, R. A. Binstead, G. N. Parsons and T. J. Meyer, Solar water splitting in a molecular photoelectrochemical cell, *Proc. Natl. Acad. Sci. U. S. A.*, 2013, **110**, 20008–20013.

32 Y. Wu, H. Zhong, W. Xu, R. Su, Y. Qin, Y. Qiu, L. Zheng, W. Gu, L. Hu, F. Lv, S. Zhang, S. P. Beckman, Y. Lin, C. Zhu and S. Guo, Harmonizing Enzyme-like Cofactors to Boost Nanozyme Catalysis, *Angew. Chem., Int. Ed.*, 2024, **63**, e202319108.

33 G. Lan, Y. Fan, W. Shi, E. You, S. S. Veroneau and W. Lin, Biomimetic active sites on monolayered metal–organic frameworks for artificial photosynthesis, *Nat. Catal.*, 2022, **5**, 1006–1018.

34 Y. Fang, J. A. Powell, E. Li, Q. Wang, Z. Perry, A. Kirchon, X. Yang, Z. Xiao, C. Zhu, L. Zhang, F. Huang and H.-C. Zhou, Catalytic reactions within the cavity of coordination cages, *Chem. Soc. Rev.*, 2019, **48**, 4707–4730.

35 C. Tan, D. Chu, X. Tang, Y. Liu, W. Xuan and Y. Cui, Supramolecular Coordination Cages for Asymmetric Catalysis, *Chem. – Eur. J.*, 2019, **25**, 662–672.

36 A. Corma and H. Garcia, Supramolecular Host–Guest Systems in Zeolites Prepared by Ship-in-a-Bottle Synthesis, *Eur. J. Inorg. Chem.*, 2004, **2004**, 1143–1164.

37 J. Gascon, A. Corma, F. Kapteijn and F. X. Llabrés i Xamena, Metal Organic Framework Catalysis: *Quo vadis?*, *ACS Catal.*, 2014, **4**, 361–378.

38 L. S. Xie, G. Skorupskii and M. Dincă, Electrically Conductive Metal–Organic Frameworks, *Chem. Rev.*, 2020, **120**, 8536–8580.

39 M. Kalaj and S. M. Cohen, Postsynthetic Modification: An Enabling Technology for the Advancement of Metal–Organic Frameworks, *ACS Cent. Sci.*, 2020, **6**, 1046–1057.

40 B. F. Hoskins and R. Robson, Design and construction of a new class of scaffolding-like materials comprising infinite polymeric frameworks of 3D-linked molecular rods. A reappraisal of the zinc cyanide and cadmium cyanide structures and the synthesis and structure of the diamond-related frameworks  $[N(CH_3)_4][CuI ZnII(CN)_4]$  and  $CuI[4',4'',4''-tetracyanotetraphenylmethane]BF_4 \cdot xC_6H_5NO_2$ , *J. Am. Chem. Soc.*, 1990, **112**, 1546–1554.

41 H. Furukawa, K. E. Cordova, M. O’Keeffe and O. M. Yaghi, The Chemistry and Applications of Metal–Organic Frameworks, *Science*, 2013, **341**, 1230444.

42 H.-C. Zhou, J. R. Long and O. M. Yaghi, Introduction to Metal–Organic Frameworks, *Chem. Rev.*, 2012, **112**, 673–674.

43 H. Li, M. Eddaoudi, M. O’Keeffe and O. M. Yaghi, Design and synthesis of an exceptionally stable and highly porous metal–organic framework, *Nature*, 1999, **402**, 276–279.



44 M. Stojanović, N. Flores-Diaz, Y. Ren, N. Vlachopoulos, L. Pfeifer, Z. Shen, Y. Liu, S. M. Zakeeruddin, J. V. Milić and A. Hagfeldt, The Rise of Dye-Sensitized Solar Cells: From Molecular Photovoltaics to Emerging Solid-State Photovoltaic Technologies, *Helv. Chim. Acta*, 2021, **104**, e2000230.

45 M. P. Suh, H. J. Park, T. K. Prasad and D.-W. Lim, Hydrogen Storage in Metal–Organic Frameworks, *Chem. Rev.*, 2012, **112**, 782–835.

46 J.-R. Li, J. Sculley and H.-C. Zhou, Metal–Organic Frameworks for Separations, *Chem. Rev.*, 2012, **112**, 869–932.

47 N. Kolobov, M. G. Goesten and J. Gascon, Metal–Organic Frameworks: Molecules or Semiconductors in Photocatalysis?, *Angew. Chem., Int. Ed.*, 2021, **60**, 26038–26052.

48 Y. Fan, H. Zheng, S. Labalme and W. Lin, Molecular Engineering of Metal–Organic Layers for Sustainable Tandem and Synergistic Photocatalysis, *J. Am. Chem. Soc.*, 2023, **145**, 4158–4165.

49 D. Yang and B. C. Gates, Catalysis by Metal Organic Frameworks: Perspective and Suggestions for Future Research, *ACS Catal.*, 2019, **9**, 1779–1798.

50 D. M. Fabian, S. Hu, N. Singh, F. A. Houle, T. Hisatomi, K. Domen, F. E. Osterloh and S. Ardo, Particle suspension reactors and materials for solar-driven water splitting, *Energy Environ. Sci.*, 2015, **8**, 2825–2850.

51 B. Rungtaweevoranit, C. S. Diercks, M. J. Kalmutzki and O. M. Yaghi, Spiers Memorial Lecture: Progress and prospects of reticular chemistry, *Faraday Discuss.*, 2017, **201**, 9–45.

52 P. M. Stanley, J. Haimerl, N. B. Shustova, R. A. Fischer and J. Warnan, *Nat. Chem.*, 2022, **14**, 1342–1356.

53 M. Ji, X. Lan, Z. Han, C. Hao and J. Qiu, Luminescent Properties of Metal–Organic Framework MOF-5: Relativistic Time-Dependent Density Functional Theory Investigations, *Inorg. Chem.*, 2012, **51**, 12389–12394.

54 X.-P. Wu, L. Gagliardi and D. G. Truhlar, Cerium Metal–Organic Framework for Photocatalysis, *J. Am. Chem. Soc.*, 2018, **140**, 7904–7912.

55 M. Zeama, M. A. Morsy, M. Abdelnaby, L. Gutiérrez-Arzaluz, O. F. Mohammed and Z. H. Yamani, Experimental and Theoretical Study on the Interchange between Zr and Ti within the MIL-125-NH<sub>2</sub> Metal Cluster, *Chem. – Asian J.*, 2021, **16**, 2520–2528.

56 K. G. M. Laurier, F. Vermoortele, R. Ameloot, D. E. De Vos, J. Hofkens and M. B. J. Roeffaers, Iron(III)-Based Metal–Organic Frameworks As Visible Light Photocatalysts, *J. Am. Chem. Soc.*, 2013, **135**, 14488–14491.

57 H.-Q. Yin, Z.-M. Zhang and T.-B. Lu, Ordered Integration and Heterogenization of Catalysts and Photosensitizers in Metal-/Covalent-Organic Frameworks for Boosting CO<sub>2</sub> Photoreduction, *Acc. Chem. Res.*, 2023, **56**, 2676–2687.

58 M. Dan-Hardi, C. Serre, T. Frot, L. Rozes, G. Maurin, C. Sanchez and G. Férey, A New Photoactive Crystalline Highly Porous Titanium(IV) Dicarboxylate, *J. Am. Chem. Soc.*, 2009, **131**, 10857–10859.

59 M. Alvaro, E. Carbonell, B. Ferrer, F. X. Llabrés iXamena and H. García, Semiconductor Behavior of a Metal–Organic Framework (MOF), *Chem. – Eur. J.*, 2007, **13**, 5106–5112.

60 S. Navalón, A. Dhakshinamoorthy, M. Álvaro, B. Ferrer and H. García, Metal–Organic Frameworks as Photocatalysts for Solar-Driven Overall Water Splitting, *Chem. Rev.*, 2023, **123**, 445–490.

61 N. Kolobov, M. G. Goesten and J. Gascon, *Angew. Chem., Int. Ed.*, 2021, **60**, 26038–26052.

62 J. H. Cava, S. Jakobsen, U. Olsbye, N. Guillou, C. Lamberti, S. Bordiga and K. P. Lillerud, A New Zirconium Inorganic Building Brick Forming Metal Organic Frameworks with Exceptional Stability, *J. Am. Chem. Soc.*, 2008, **130**, 13850–13851.

63 M. Cheng, P. Yan, X. Zheng, B. Gao, X. Yan, G. Zhang, X. Cui and Q. Xu, Porphyrin-based Bi-MOFs with Enriched Surface Bi Active Sites for Boosting Photocatalytic CO<sub>2</sub> Reduction, *Chem. – Eur. J.*, 2023, **29**, e202302395.

64 D. Sun, Y. Fu, W. Liu, L. Ye, D. Wang, L. Yang, X. Fu and Z. Li, Studies on photocatalytic CO<sub>2</sub> reduction over NH<sub>2</sub>-uiio-66(Zr) and its derivatives: Towards a better understanding of photocatalysis on metal-organic frameworks, *Chem. – Eur. J.*, 2013, **19**, 14279–14285.

65 Y. Fu, D. Sun, Y. Chen, R. Huang, Z. Ding, X. Fu and Z. Li, An Amine-Functionalized Titanium Metal–Organic Framework Photocatalyst with Visible-Light-Induced Activity for CO<sub>2</sub> Reduction, *Angew. Chem., Int. Ed.*, 2012, **51**, 3364–3367.

66 K. Wang, B. Yan, B. Zhou, Y. Zhang, G.-L. Lin, T.-S. Zhang, M. Zhou, H.-M. Shen, Y.-F. Yang, J. Xia, H. Li and Y. She, Acceleration of Photoinduced Electron Transfer by Modulating Electronegativity of Substituents in Stable Zr-Metal–Organic Frameworks to Boost Photocatalytic CO<sub>2</sub> Reduction, *ACS Appl. Mater. Interfaces*, 2024, **16**, 33601–33610.

67 N. Li, G.-Q. Lai, L.-H. Chung, F. Yu, J. He and Y.-Q. Lan, Achieving High CO<sub>2</sub> Photoreduction Activity by Conductive Crosslinks of Metal–Organic Framework, *CCS Chem.*, 2024, **6**, 1211–1221.

68 J. T. Bryant, M. W. Logan, Z. Chen, M. Djokic, D. R. Cairnie, D. A. Vazquez-Molina, A. Nijamudheen, K. R. Langlois, M. J. Markley, G. Pombar, A. A. Holland, J. D. Caranto, J. K. Harper, A. J. Morris, J. L. Mendoza-Cortes, T. Jurca, K. W. Chapman and F. J. Uribe-Romo, Synergistic Steric and Electronic Effects on the Photoredox Catalysis by a Multivariate Library of Titania Metal–Organic Frameworks, *J. Am. Chem. Soc.*, 2023, **145**, 4589–4600.

69 J.-R. An, Y. Wang, W.-W. Dong, X.-J. Gao, O.-Y. Yang, Y.-L. Liu, J. Zhao and D.-S. Li, Efficient Visible-Light Photoreduction of CO<sub>2</sub> to CH<sub>4</sub> over an Fe-Based Metal–Organic Framework (PCN-250-Fe<sub>3</sub>) in a Solid-Gas Mode, *ACS Appl. Energy Mater.*, 2022, **5**, 2384–2390.



70 S. K. Lee, M. Kondo, M. Okamura, T. Enomoto, G. Nakamura and S. Masaoka, Function-Integrated Ru Catalyst for Photochemical CO<sub>2</sub> Reduction, *J. Am. Chem. Soc.*, 2018, **140**, 16899–16903.

71 Y. Pi, X. Feng, Y. Song, Z. Xu, Z. Li and W. Lin, Metal-Organic Frameworks Integrate Cu Photosensitizers and Secondary Building Unit-Supported Fe Catalysts for Photocatalytic Hydrogen Evolution, *J. Am. Chem. Soc.*, 2020, **142**, 10302–10307.

72 Y. Zhu, G. Lan, Y. Fan, S. S. Veroneau, Y. Song, D. Micheroni and W. Lin, Merging Photoredox and Organometallic Catalysts in a Metal-Organic Framework Significantly Boosts Photocatalytic Activities, *Angew. Chem., Int. Ed.*, 2018, **57**, 14090–14094.

73 C.-C. Hou, T.-T. Li, S. Cao, Y. Chen and W.-F. Fu, Incorporation of a [Ru(dcbpy)(bpy)<sub>2</sub>]<sup>2+</sup> photosensitizer and a Pt(dcbpy)Cl<sub>2</sub> catalyst into metal-organic frameworks for photocatalytic hydrogen evolution from aqueous solution, *J. Mater. Chem. A*, 2015, **3**, 10386–10394.

74 S. Yang, D. Fan, W. Hu, B. Pattengale, C. Liu, X. Zhang and J. Huang, Elucidating Charge Separation Dynamics in a Hybrid Metal-Organic Framework Photocatalyst for Light-Driven H<sub>2</sub> Evolution, *J. Phys. Chem. C*, 2018, **122**, 3305–3311.

75 X. Feng, Y. Pi, Y. Song, C. Brzezinski, Z. Xu, Z. Li and W. Lin, Metal-Organic Frameworks Significantly Enhance Photocatalytic Hydrogen Evolution and CO<sub>2</sub> Reduction with Earth-Abundant Copper Photosensitizers, *J. Am. Chem. Soc.*, 2020, **142**, 690–695.

76 S. Guo, L. Kong, P. Wang, S. Yao, T. Lu and Z. Zhang, Switching Excited State Distribution of Metal-Organic Framework for Dramatically Boosting Photocatalysis, *Angew. Chem., Int. Ed.*, 2022, **61**, e202206193.

77 W. Wang, X.-W. Song, Z. Hong, B. Li, Y. Si, C. Ji, K. Su, Y. Tan, Z. Ju, Y. Huang, C.-N. Chen and D. Yuan, Incorporation of iron hydrogenase active sites into a stable photosensitizing metal-organic framework for enhanced hydrogen production, *Appl. Catal., B*, 2019, **258**, 117979.

78 D. Wang, R. Huang, W. Liu, D. Sun and Z. Li, Fe-Based MOFs for Photocatalytic CO<sub>2</sub> Reduction: Role of Coordination Unsaturated Sites and Dual Excitation Pathways, *ACS Catal.*, 2014, **4**, 4254–4260.

79 S. R. V. Parambil, S. Karmakar, F. A. Rahimi and T. K. Maji, Confining Molecular Photosensitizer and Catalyst in MOF toward Artificial Photosynthesis: Validating Electron Transfer by *In Situ* DRIFT Study, *ACS Appl. Mater. Interfaces*, 2023, **15**, 27821–27831.

80 Y. Song, Y. Pi, X. Feng, K. Ni, Z. Xu, J. S. Chen, Z. Li and W. Lin, Cerium-Based Metal-Organic Layers Catalyze Hydrogen Evolution Reaction through Dual Photoexcitation, *J. Am. Chem. Soc.*, 2020, **142**, 6866–6871.

81 S. Karmakar, S. Barman, F. A. Rahimi and T. K. Maji, Covalent grafting of molecular photosensitizer and catalyst on MOF-808: effect of pore confinement toward visible light-driven CO<sub>2</sub> reduction in water, *Energy Environ. Sci.*, 2021, **14**, 2429–2440.

82 P. M. Stanley, K. Hemmer, M. Hegelmann, A. Schulz, M. Park, M. Elsner, M. Cokoja and J. Warnan, Topology- and wavelength-governed CO<sub>2</sub> reduction photocatalysis in molecular catalyst-metal-organic framework assemblies, *Chem. Sci.*, 2022, **13**, 12164–12174.

83 K. Sasan, Q. Lin, C. Mao and P. Feng, Incorporation of iron hydrogenase active sites into a highly stable metal-organic framework for photocatalytic hydrogen generation, *Chem. Commun.*, 2014, **50**, 10390.

84 J. H. Kim, S. Wu, L. Zdrail, N. Denisov and P. Schmuki, 2D Metal-Organic Framework Nanosheets based on Pd-TCPP as Photocatalysts for Highly Improved Hydrogen Evolution, *Angew. Chem., Int. Ed.*, 2024, **63**, e202319255.

85 Q. Zuo, T. Liu, C. Chen, Y. Ji, X. Gong, Y. Mai and Y. Zhou, Ultrathin Metal-Organic Framework Nanosheets with Ultrahigh Loading of Single Pt Atoms for Efficient Visible-Light-Driven Photocatalytic H<sub>2</sub> Evolution, *Angew. Chem., Int. Ed.*, 2019, **58**, 10198–10203.

86 X. Fang, Q. Shang, Y. Wang, L. Jiao, T. Yao, Y. Li, Q. Zhang, Y. Luo and H. Jiang, Single Pt Atoms Confined into a Metal-Organic Framework for Efficient Photocatalysis, *Adv. Mater.*, 2018, **30**, 1705112.

87 C. Xu, Y. Pan, G. Wan, H. Liu, L. Wang, H. Zhou, S.-H. Yu and H.-L. Jiang, Turning on Visible-Light Photocatalytic C–H Oxidation over Metal-Organic Frameworks by Introducing Metal-to-Cluster Charge Transfer, *J. Am. Chem. Soc.*, 2019, **141**, 19110–19117.

88 P. M. Stanley, J. Haimerl, C. Thomas, A. Urstoege, M. Schuster, N. B. Shustova, A. Casini, B. Rieger, J. Warnan and R. A. Fischer, Host–Guest Interactions in a Metal-Organic Framework Isoreticular Series for Molecular Photocatalytic CO<sub>2</sub> Reduction, *Angew. Chem., Int. Ed.*, 2021, **60**, 17854–17860.

89 J.-Y. Zhou, X.-Y. Guan, H.-P. Zhang, D. Luo, X. Wang, X.-P. Zhou and D. Li, Exposing coordination-unsaturated Co sites in Co-MOF for efficient photocatalytic water oxidation, *Inorg. Chem. Front.*, 2024, **11**, 5484–5489.

90 M. Wang, J. Liu, C. Guo, X. Gao, C. Gong, Y. Wang, B. Liu, X. Li, G. G. Gurzadyan and L. Sun, Metal-organic frameworks (ZIF-67) as efficient cocatalysts for photocatalytic reduction of CO<sub>2</sub>: the role of the morphology effect, *J. Mater. Chem. A*, 2018, **6**, 4768–4775.

91 H. Zhong, Z. Jiang, J. Hu, L.-H. Chung and J. He, 2D metal-organic frameworks bearing butterfly-shaped metal-bis(dithiolene) linkers from dithiol-functionalized benzenedicarboxylic acid, *Chem. Commun.*, 2024, **60**, 7578–7581.

92 S. Subudhi, S. P. Tripathy and K. Parida, Highlights of the characterization techniques on inorganic, organic (COF) and hybrid (MOF) photocatalytic semiconductors, *Catal. Sci. Technol.*, 2021, **11**, 392–415.

93 P. Hirschle, T. Preiß, F. Auras, A. Pick, J. Völkner, D. Valdepérez, G. Witte, W. J. Parak, J. O. Rädler and S. Wuttke, Exploration of MOF nanoparticle sizes using



various physical characterization methods – is what you measure what you get?, *CrystEngComm*, 2016, **18**, 4359–4368.

94 Z.-H. Yan, M.-H. Du, J. Liu, S. Jin, C. Wang, G.-L. Zhuang, X.-J. Kong, L.-S. Long and L.-S. Zheng, Photo-generated dinuclear {Eu(II)}<sub>2</sub> active sites for selective CO<sub>2</sub> reduction in a photosensitizing metal-organic framework, *Nat. Commun.*, 2018, **9**, 3353.

95 D. R. Cairnie and A. J. Morris, A Technical Guide for Performing Spectroscopic Measurements on Metal-Organic Frameworks, *J. Visualized Exp.*, 2023, **194**, e65072.

96 L. Hanna and J. V. Lockard, From IR to X-rays: gaining molecular level insights on metal-organic frameworks through spectroscopy, *J. Phys.: Condens. Matter*, 2019, **31**, 483001.

97 M. Bláha, V. Valeš, Z. Bastl, M. Kalbáč and H. Shiozawa, Host–Guest Interactions in Metal–Organic Frameworks Doped with Acceptor Molecules as Revealed by Resonance Raman Spectroscopy, *J. Phys. Chem. C*, 2020, **124**, 24245–24250.

98 E. Brunner and M. Rauche, Solid-state NMR spectroscopy: an advancing tool to analyse the structure and properties of metal–organic frameworks, *Chem. Sci.*, 2020, **11**, 4297–4304.

99 S. Mandal, S. P. Nanavati, D. J. Willock and R. Ananthakrishnan, Photoactive Ag(I)-Based Coordination Polymer as a Potential Semiconductor for Photocatalytic Water Splitting and Environmental Remediation: Experimental and Theoretical Approach, *J. Phys. Chem. C*, 2019, **123**, 23940–23950.

100 E. M. Thoresen, S. Øien-Ødegaard, G. Kaur, M. Tilset, K. P. Lillerud and M. Amedjkouh, Strongly visible light-absorbing metal–organic frameworks functionalized by cyclometalated ruthenium(II) complexes, *RSC Adv.*, 2020, **10**, 9052–9062.

101 J. Shi, F. Chen, L. Hou, G. Li, Y. Li, X. Guan, H. Liu and L. Guo, Eosin Y bidentately bridged on UiO-66-NH<sub>2</sub> by solvothermal treatment towards enhanced visible-light-driven photocatalytic H<sub>2</sub> production, *Appl. Catal., B*, 2021, **280**, 119385.

102 D. Chen, Z. Jin and H. Xing, Titanium–Porphyrin Metal–Organic Frameworks as Visible-Light-Driven Catalysts for Highly Efficient Sonophotocatalytic Reduction of Cr(VI), *Langmuir*, 2022, **38**, 12292–12299.

103 C. Wang and W. Lin, Diffusion-Controlled Luminescence Quenching in Metal–Organic Frameworks, *J. Am. Chem. Soc.*, 2011, **133**, 4232–4235.

104 Q. Zhang, C. Zhang, L. Cao, Z. Wang, B. An, Z. Lin, R. Huang, Z. Zhang, C. Wang and W. Lin, Förster Energy Transport in Metal–Organic Frameworks Is Beyond Step-by-Step Hopping, *J. Am. Chem. Soc.*, 2016, **138**, 5308–5315.

105 J. Li, S. Yuan, J.-S. Qin, L. Huang, R. Bose, J. Pang, P. Zhang, Z. Xiao, K. Tan, A. V. Malko, T. Cagin and H.-C. Zhou, Fluorescence Enhancement in the Solid State by Isolating Perylene Fluorophores in Metal–Organic Frameworks, *ACS Appl. Mater. Interfaces*, 2020, **12**, 26727–26732.

106 J.-S. Qin, S. Yuan, L. Zhang, B. Li, D.-Y. Du, N. Huang, W. Guan, H. F. Drake, J. Pang, Y.-Q. Lan, A. Alsalme and H.-C. Zhou, Creating Well-Defined Hexabenzocoronene in Zirconium Metal–Organic Framework by Postsynthetic Annulation, *J. Am. Chem. Soc.*, 2019, **141**, 2054–2060.

107 M. Elcheikh Mahmoud, H. Audi, A. Assoud, T. H. Ghaddar and M. Hmadedh, Metal–Organic Framework Photocatalyst Incorporating Bis(4'-(4-carboxyphenyl)-terpyridine)ruthenium(II) for Visible-Light-Driven Carbon Dioxide Reduction, *J. Am. Chem. Soc.*, 2019, **141**, 7115–7121.

108 K. Ling, M. M. Ogle, E. Flores, F. Godoy and A. A. Martí, Exploring the Photophysical Properties of UiO-67 MOF Doped with Rhenium Carbonyl Complexes, *J. Photochem. Photobiol.*, 2022, **11**, 100127.

109 A. Santiago-Portillo, H. G. Baldoví, E. Carbonell, S. Navalón, M. Álvaro, H. García and B. Ferrer, Ruthenium (II) Tris(2,2'-bipyridyl) Complex Incorporated in UiO-67 as Photoredox Catalyst, *J. Phys. Chem. C*, 2018, **122**, 29190–29199.

110 H. Hu, Z. Wang, L. Cao, L. Zeng, C. Zhang, W. Lin and C. Wang, Metal–organic frameworks embedded in a liposome facilitate overall photocatalytic water splitting, *Nat. Chem.*, 2021, **13**, 358–366.

111 Y. Chen, P. Li, J. Zhou, C. T. Buru, L. Dordević, P. Li, X. Zhang, M. M. Cetin, J. F. Stoddart, S. I. Stupp, M. R. Wasielewski and O. K. Farha, Integration of Enzymes and Photosensitizers in a Hierarchical Mesoporous Metal–Organic Framework for Light-Driven CO<sub>2</sub> Reduction, *J. Am. Chem. Soc.*, 2020, **142**, 1768–1773.

112 Q. Ye, D. R. Cairnie, D. Troya, N. Kumar, X. Yang and A. J. Morris, Photoinduced Dynamic Ligation in Metal–Organic Frameworks, *J. Am. Chem. Soc.*, 2024, **146**, 101–105.

113 W.-M. Liao, J.-H. Zhang, Z. Wang, Y.-L. Lu, S.-Y. Yin, H.-P. Wang, Y.-N. Fan, M. Pan and C.-Y. Su, Semiconductive Amine-Functionalized Co(II)-MOF for Visible-Light-Driven Hydrogen Evolution and CO<sub>2</sub> Reduction, *Inorg. Chem.*, 2018, **57**, 11436–11442.

114 W. Hou, C. Chen, D. Xie and Y. Xu, Substituted Ti(IV) in Ce-UiO-66-NH<sub>2</sub> Metal–Organic Frameworks Increases H<sub>2</sub> and O<sub>2</sub> Evolution under Visible Light, *ACS Appl. Mater. Interfaces*, 2023, **15**, 2911–2921.

115 L. Pukdeejorhor, S. Wannapaiboon, J. Berger, K. Rodewald, S. Thongratkaew, S. Impeng, J. Warnan, S. Bureekaew and R. A. Fischer, Defect engineering in MIL-125-(Ti)-NH<sub>2</sub> for enhanced photocatalytic H<sub>2</sub> generation, *J. Mater. Chem. A*, 2023, **11**, 9143–9151.

116 S. Dai, E. Montero-Lanzuela, A. Tissot, H. G. Baldoví, H. García, S. Navalón and C. Serre, Room temperature design of Ce(IV)-MOFs: from photocatalytic HER and OER to overall water splitting under simulated sunlight irradiation, *Chem. Sci.*, 2023, **14**, 3451–3461.



117 V. Kavun, E. Uslamin, B. van der Linden, S. Canossa, A. Goryachev, E. E. Bos, J. Garcia Santaclar, G. Smolentsev, E. Repo and M. A. van der Veen, Promoting Photocatalytic Activity of  $\text{NH}_2\text{-MIL-125(Ti)}$  for  $\text{H}_2$  Evolution Reaction through Creation of Ti III - and Co I -Based Proton Reduction Sites, *ACS Appl. Mater. Interfaces*, 2023, **15**, 54590–54601.

118 Y. Song, Z. Li, Y. Zhu, X. Feng, J. S. Chen, M. Kaufmann, C. Wang and W. Lin, Titanium Hydroxide Secondary Building Units in Metal–Organic Frameworks Catalyze Hydrogen Evolution under Visible Light, *J. Am. Chem. Soc.*, 2019, **141**, 12219–12223.

119 J. Gu, Y. Peng, T. Zhou, J. Ma, H. Pang and Y. Yamauchi, Porphyrin-based framework materials for energy conversion, *Nano Res. Energy*, 2022, **1**, e9120009.

120 G. Lan, Y.-Y. Zhu, S. S. Veroneau, Z. Xu, D. Micheroni and W. Lin, Electron Injection from Photoexcited Metal–Organic Framework Ligands to Ru<sub>2</sub> Secondary Building Units for Visible-Light-Driven Hydrogen Evolution, *J. Am. Chem. Soc.*, 2018, **140**, 5326–5329.

121 W. Liu, S. Zhang, B. Wu, X. Gong, J. Shao, S. Wang and J. Tian, Platinum-Assisted Bimetallic Ru–Eu/Pr MOFs for Photocatalytic  $\text{H}_2$  Evolution from Water Splitting, *ACS Appl. Nano Mater.*, 2023, **6**, 16826–16836.

122 T. Toyao, M. Saito, S. Dohshi, K. Mochizuki, M. Iwata, H. Higashimura, Y. Horiuchi and M. Matsuoka, Development of a Ru complex-incorporated MOF photocatalyst for hydrogen production under visible-light irradiation, *Chem. Commun.*, 2014, **50**, 6779.

123 Y. Song, Z. Li, Y. Zhu, X. Feng, J. S. Chen, M. Kaufmann, C. Wang and W. Lin, Titanium Hydroxide Secondary Building Units in Metal–Organic Frameworks Catalyze Hydrogen Evolution under Visible Light, *J. Am. Chem. Soc.*, 2019, **141**, 12219–12223.

124 B. Zhang and L. Sun, Artificial photosynthesis: opportunities and challenges of molecular catalysts, *Chem. Soc. Rev.*, 2019, **48**, 2216–2264.

125 P. M. Stanley, A. Y. Su, V. Ramm, P. Fink, C. Kimna, O. Liele, M. Elsner, J. A. Lercher, B. Rieger, J. Warnan and R. A. Fischer, Photocatalytic  $\text{CO}_2$  -to-Syngas Evolution with Molecular Catalyst Metal–Organic Framework Nanozymes, *Adv. Mater.*, 2023, **35**, 2207380.

126 X. Ma, H. Liu, W. Yang, G. Mao, L. Zheng and H.-L. Jiang, Modulating Coordination Environment of Single-Atom Catalysts and Their Proximity to Photosensitive Units for Boosting MOF Photocatalysis, *J. Am. Chem. Soc.*, 2021, **143**, 12220–12229.

127 V. Kavun, E. Uslamin, B. van der Linden, S. Canossa, A. Goryachev, E. E. Bos, J. Garcia Santaclar, G. Smolentsev, E. Repo and M. A. van der Veen, Promoting Photocatalytic Activity of  $\text{NH}_2\text{-MIL-125(Ti)}$  for  $\text{H}_2$  Evolution Reaction through Creation of Ti III - and Co I -Based Proton Reduction Sites, *ACS Appl. Mater. Interfaces*, 2023, **15**, 54590–54601.

128 W. Liang, M. Z. M. Noor, W. Lewis, A. Macmillan, X. Zhang, R. Tang, A. Kochubei, D. Wiley, B. S. Haynes and J. Huang, Design of an  $\text{ocu}$ –Metal–Organic Framework for a Photocatalysis Reaction, *ChemPhotoChem*, 2023, **7**, e202300031.

129 X. Zhang, Z. Li, H. Li, D. Yang, Z. Ren, Y. Zhang, J. Zhang and X. Bu, Surface–Grafted Single–Atomic Pt–N<sub>x</sub> Complex with a Precisely Regulating Coordination Sphere for Efficient Electron Acceptor-Inducing Interfacial Electron Transfer, *Angew. Chem., Int. Ed.*, 2024, **63**, e202404386.

130 F. Leng, H. Liu, M. Ding, Q. P. Lin and H. L. Jiang, Boosting Photocatalytic Hydrogen Production of Porphyrinic MOFs: The Metal Location in Metalloporphyrin Matters, *ACS Catal.*, 2018, **8**, 4583–4590.

131 C. Lin, C. Han, H. Zhang, L. Gong, Y. Gao, H. Wang, Y. Bian, R. Li and J. Jiang, Porphyrin-Based Metal–Organic Frameworks for Efficient Photocatalytic  $\text{H}_2$  Production under Visible-Light Irradiation, *Inorg. Chem.*, 2021, **60**, 3988–3995.

132 X. Fang, Q. Shang, Y. Wang, L. Jiao, T. Yao, Y. Li, Q. Zhang, Y. Luo and H. Jiang, Single Pt Atoms Confined into a Metal–Organic Framework for Efficient Photocatalysis, *Adv. Mater.*, 2018, **30**, 1705112.

133 H. Feng, H. Li, X. Liu, Y. Huang, Q. Pan, R. Peng, R. Du, X. Zheng, Z. Yin, S. Li and Y. He, Porphyrin-based Ti-MOFs conferred with single-atom Pt for enhanced photocatalytic hydrogen evolution and NO removal, *Chem. Eng. J.*, 2022, **428**, 132045.

134 S. Wang, S. Li, C. Zheng, H. Feng and Y.-S. Feng, Bimetallic Porphyrin-Based Metal–Organic Framework as a Superior Photocatalyst for Enhanced Photocatalytic Hydrogen Production, *Inorg. Chem.*, 2024, **63**, 554–563.

135 M. A. Nasalevich, R. Becker, E. V. Ramos-Fernandez, S. Castellanos, S. L. Veber, M. V. Fedin, F. Kapteijn, J. N. H. Reek, J. I. van der Vlugt and J. Gascon, Co@NH<sub>2</sub>-MIL-125(Ti): cobaloxime-derived metal–organic framework-based composite for light-driven  $\text{H}_2$  production, *Energy Environ. Sci.*, 2015, **8**, 364–375.

136 Z. Li, J.-D. Xiao and H.-L. Jiang, Encapsulating a Co(II) Molecular Photocatalyst in Metal–Organic Framework for Visible-Light-Driven  $\text{H}_2$  Production: Boosting Catalytic Efficiency via Spatial Charge Separation, *ACS Catal.*, 2016, **6**, 5359–5365.

137 H. Zheng, L. Pei, J. Bai, P. Wu, X. Zhao, Y. Yang, Z. Chen, M. Zhang and J. Wang, Eosin Y-Based Metal–Organic Framework Synergistic with Cobalt(II) Complex for Hydrogen Evolution through Photoinduced Intermolecular Electron Transfer, *Inorg. Chem.*, 2023, **62**, 21424–21431.

138 R. Rojas-Luna, J. Amaro-Gahete, D. G. Gil-Gavilán, M. Castillo-Rodríguez, C. Jiménez-Sanchidrián, J. R. Ruiz, D. Esquivel and F. J. Romero-Salguero, Visible-light-harvesting basolite-A520 metal organic framework for photocatalytic hydrogen evolution, *Microporous Mesoporous Mater.*, 2023, **355**, 112565.

139 P. Wu, X. Guo, L. Cheng, C. He, J. Wang and C. Duan, Photoactive Metal–Organic Framework and Its Film for



Light-Driven Hydrogen Production and Carbon Dioxide Reduction, *Inorg. Chem.*, 2016, **55**, 8153–8159.

140 B. C. Yallur, V. Adimule, W. Nabgan, M. S. Raghu, F. A. Alharthi, B.-H. Jeon and L. Parashuram, Solar-light-sensitive Zr/Cu-(H2BDC-BPD) metal organic framework for photocatalytic dye degradation and hydrogen evolution, *Surf. Interfaces*, 2023, **36**, 102587.

141 J. Li, Q. Lin, N. Li, Z. Li, G. Tan, S. Liu, L. Chung, W. Liao, L. Yu and J. He, Symbiotically Reinforced Bimetallic Photocatalysis in Conjugated Metal–Organic Framework Nanosheets, *Adv. Funct. Mater.*, 2023, **33**, 2210717.

142 S. Pullen, H. Fei, A. Orthaber, S. M. Cohen and S. Ott, Enhanced Photochemical Hydrogen Production by a Molecular Diiron Catalyst Incorporated into a Metal–Organic Framework, *J. Am. Chem. Soc.*, 2013, **135**, 16997–17003.

143 C. Bozal-Ginesta, S. Pullen, S. Ott and L. Hammarström, Self-Recovery of Photochemical H<sub>2</sub> Evolution with a Molecular Diiron Catalyst Incorporated in a UiO-66 Metal–Organic Framework, *ChemPhotoChem*, 2020, **4**, 287–290.

144 Y. Yamazaki, H. Takeda and O. Ishitani, Photocatalytic reduction of CO<sub>2</sub> using metal complexes, *J. Photochem. Photobiol. C*, 2015, **25**, 106–137.

145 Y. Kuramochi, O. Ishitani and H. Ishida, Reaction mechanisms of catalytic photochemical CO<sub>2</sub> reduction using Re (I) and Ru(II) complexes, *Coord. Chem. Rev.*, 2018, **373**, 333–356.

146 H. Takeda, C. Cometto, O. Ishitani and M. Robert, Electrons, Photons, Protons and Earth-Abundant Metal Complexes for Molecular Catalysis of CO<sub>2</sub> Reduction, *ACS Catal.*, 2017, **7**, 70–88.

147 L. Wang, H. Zhang, Z. Zhang, J. Zhang, Y. He, Q. Li, J. Bao, M. Fang and Y. Wu, Highly Efficient and Selective Visible-light Photocatalytic CO<sub>2</sub> Reduction to CO Using a 2D Co(II)-Imidazole MOF as Cocatalyst and Ru(bpy)<sub>3</sub> Cl<sub>2</sub> as Photosensitizer, *Chem.-Asian J.*, 2023, **18**, e202300297.

148 Z. Su, B. Yu, J. Feng, M. Zhong, X. Li and J. Shi, Co-Encapsulation of Rhenium and Ruthenium Complexes into the Scaffolds of Metal–Organic Framework to Promote CO<sub>2</sub> Reduction, *Catalysts*, 2023, **13**, 1510.

149 P. M. Stanley, C. Thomas, E. Thyraug, A. Urstroeger, M. Schuster, J. Hauer, B. Rieger, J. Warnan and R. A. Fischer, Entrapped Molecular Photocatalyst and Photosensitizer in Metal–Organic Framework Nanoreactors for Enhanced Solar CO<sub>2</sub> Reduction, *ACS Catal.*, 2021, **11**, 871–882.

150 U. J. Ryu, S. J. Kim, H.-K. Lim, H. Kim, K. M. Choi and J. K. Kang, Synergistic interaction of Re complex and amine functionalized multiple ligands in metal–organic frameworks for conversion of carbon dioxide, *Sci. Rep.*, 2017, **7**, 612.

151 S. Karmakar, S. Barman, F. A. Rahimi, D. Rambabu, S. Nath and T. K. Maji, Confining charge-transfer complex in a metal-organic framework for photocatalytic CO<sub>2</sub> reduction in water, *Nat. Commun.*, 2023, **14**, 4508.

152 K. M. Batoo, E. Ali, B. A. Hussein, A. Al-khalidi, U. S. Altimari, S. Hussain, S. H. Kareem, M. K. Abid, A. Alawadi and A. Ihsan, The cooperative performance of iodo and copper in a Zr-based UiO-67 metal-organic framework for highly selective photocatalytic CO<sub>2</sub> reduction to methanol, *J. Mol. Struct.*, 2024, **1307**, 137927.

153 G. Lan, Z. Li, S. S. Veroneau, Y.-Y. Zhu, Z. Xu, C. Wang and W. Lin, Photosensitizing Metal–Organic Layers for Efficient Sunlight-Driven Carbon Dioxide Reduction, *J. Am. Chem. Soc.*, 2018, **140**, 12369–12373.

154 H. Fei, M. D. Sampson, Y. Lee, C. P. Kubiak and S. M. Cohen, Photocatalytic CO<sub>2</sub> Reduction to Formate Using a Mn(I) Molecular Catalyst in a Robust Metal–Organic Framework, *Inorg. Chem.*, 2015, **54**, 6821–6828.

155 A. Mengele and S. Rau, Product Selectivity in Homogeneous Artificial Photosynthesis Using [(bpy)Rh (Cp\*)Xn<sup>+</sup>]-Based Catalysts, *Inorganics*, 2017, **5**, 35.

156 W.-M. Liao, J.-H. Zhang, Z. Wang, S.-Y. Yin, M. Pan, H.-P. Wang and C.-Y. Su, Post-synthetic exchange (PSE) of UiO-67 frameworks with Ru/Rh half-sandwich units for visible-light-driven H<sub>2</sub> evolution and CO<sub>2</sub> reduction, *J. Mater. Chem. A*, 2018, **6**, 11337–11345.

157 M. B. Chambers, X. Wang, N. Elgrishi, C. H. Hendon, A. Walsh, J. Bonnefoy, J. Canivet, E. A. Quadrelli, D. Farrusseng, C. Mellot-Draznieks and M. Fontecave, Photocatalytic Carbon Dioxide Reduction with Rhodium-based Catalysts in Solution and Heterogenized within Metal–Organic Frameworks, *ChemSusChem*, 2015, **8**, 603–608.

158 Y. Benseghir, A. Lemarchand, M. Duguet, P. Mialane, M. Gomez-Mingot, C. Roch-Marchal, T. Pino, M.-H. Ha-Thi, M. Haouas, M. Fontecave, A. Dolbecq, C. Sasseoye and C. Mellot-Draznieks, Co-immobilization of a Rh Catalyst and a Keggin Polyoxometalate in the UiO-67 Zr-Based Metal–Organic Framework: In Depth Structural Characterization and Photocatalytic Properties for CO<sub>2</sub> Reduction, *J. Am. Chem. Soc.*, 2020, **142**, 9428–9438.

159 X. Wang, F. M. Wisser, J. Canivet, M. Fontecave and C. Mellot-Draznieks, Immobilization of a Full Photosystem in the Large-Pore MIL-101 Metal–Organic Framework for CO<sub>2</sub> reduction, *ChemSusChem*, 2018, **11**, 3315–3322.

160 M. D. Kärkäs, O. Verho, E. V. Johnston and B. Åkermark, *Chem. Rev.*, 2014, **114**, 11863–12001.

161 W. Stedman, H. Kang, S. Lin, J. L. Kissil, M. S. Bartolomei and P. M. Lieberman, Cohesins localize with CTCF at the KSHV latency control region and at cellular c-myc and H19/Igf2 insulators, *EMBO J.*, 2008, **27**, 654–666.

162 Y. Horiuchi, T. Toyao, K. Miyahara, L. Zakary, D. Do Van, Y. Kamata, T.-H. Kim, S. W. Lee and M. Matsuoka, Visible-light-driven photocatalytic water oxidation catalysed by iron-based metal–organic frameworks, *Chem. Commun.*, 2016, **52**, 5190–5193.

163 J. Schneider and D. W. Bahnemann, Undesired Role of Sacrificial Reagents in Photocatalysis, *J. Phys. Chem. Lett.*, 2013, **4**, 3479–3483.



164 L. Chi, Q. Xu, X. Liang, J. Wang and X. Su, Iron-Based Metal–Organic Frameworks as Catalysts for Visible Light-Driven Water Oxidation, *Small*, 2016, **12**, 1351–1358.

165 N.-Y. Huang, J.-Q. Shen, Z.-M. Ye, W.-X. Zhang, P.-Q. Liao and X.-M. Chen, An exceptionally stable octacobalt-cluster-based metal–organic framework for enhanced water oxidation catalysis, *Chem. Sci.*, 2019, **10**, 9859–9864.

166 L. Li, Z.-B. Fang, W. Deng, J.-D. Yi, R. Wang and T.-F. Liu, Precise Construction of Stable Bimetallic Metal–Organic Frameworks with Single-Site Ti(IV) Incorporation in Nodes for Efficient Photocatalytic Oxygen Evolution, *CCS Chem.*, 2022, **4**, 2782–2792.

167 G. Paille, M. Gomez-Mingot, C. Roch-Marchal, B. Lassalle-Kaiser, P. Mialane, M. Fontecave, C. Mellot-Draznieks and A. Dolbecq, A Fully Noble Metal-Free Photosystem Based on Cobalt-Polyoxometalates Immobilized in a Porphyrinic Metal–Organic Framework for Water Oxidation, *J. Am. Chem. Soc.*, 2018, **140**, 3613–3618.

168 L. Wang, P. Jin, J. Huang, H. She and Q. Wang, Integration of Copper(II)-Porphyrin Zirconium Metal–Organic Framework and Titanium Dioxide to Construct Z-Scheme System for Highly Improved Photocatalytic CO<sub>2</sub> Reduction, *ACS Sustainable Chem. Eng.*, 2019, **7**, 15660–15670.

169 X. Yang and D. Wang, Photocatalysis: From Fundamental Principles to Materials and Applications, *ACS Appl. Energy Mater.*, 2018, **1**, 6657–6693.

170 V. Augugliaro, M. Bellardita, V. Loddo, G. Palmisano, L. Palmisano and S. Yurdakal, Overview on oxidation mechanisms of organic compounds by TiO<sub>2</sub> in heterogeneous photocatalysis, *J. Photochem. Photobiol. C*, 2012, **13**, 224–245.

171 L. Luo, T. Zhang, M. Wang, R. Yun and X. Xiang, Recent Advances in Heterogeneous Photo-Driven Oxidation of Organic Molecules by Reactive Oxygen Species, *ChemSusChem*, 2020, **13**, 5173–5184.

172 D. Wang and Z. Li, Bi-functional NH<sub>2</sub>-MIL-101(Fe) for one-pot tandem photo-oxidation/Knoevenagel condensation between aromatic alcohols and active methylene compounds, *Catal. Sci. Technol.*, 2015, **5**, 1623–1628.

173 D. Sun, L. Ye and Z. Li, Visible-light-assisted aerobic photocatalytic oxidation of amines to imines over NH<sub>2</sub>-MIL-125(Ti), *Appl. Catal. B*, 2015, **164**, 428–432.

174 R. Liu, S. Meng, Y. Ma, L. Niu, S. He, X. Xu, B. Su, D. Lu, Z. Yang and Z. Lei, Atmospherical oxidative coupling of amines by UiO-66-NH<sub>2</sub> photocatalysis under milder reaction conditions, *Catal. Commun.*, 2019, **124**, 108–112.

175 S. Yuan, T.-F. Liu, D. Feng, J. Tian, K. Wang, J. Qin, Q. Zhang, Y.-P. Chen, M. Bosch, L. Zou, S. J. Teat, S. J. Dalgarno and H.-C. Zhou, A single crystalline porphyrinic titanium metal–organic framework, *Chem. Sci.*, 2015, **6**, 3926–3930.

176 W. Sheng, F. Huang, X. Dong and X. Lang, Solvent-controlled synthesis of Ti-based porphyrinic metal–organic frameworks for the selective photocatalytic oxidation of amines, *J. Colloid Interface Sci.*, 2022, **628**, 784–793.

177 Y. Liu, L. Li, S. Meng, J. Wang, Q. Xu, P. Ma, J. Wang and J. Niu, Fabrication of Polyoxometalate-Based Metal–Organic Frameworks Integrating Paddlewheel Rh<sub>2</sub>(OAc)<sub>4</sub> for Visible-Light-Driven Oxidative Coupling of Amines, *Inorg. Chem.*, 2023, **62**, 12954–12964.

178 Y. Liu, K. Ji, J. Wang, H. Li, X. Zhu, P. Ma, J. Niu and J. Wang, Enhanced Carrier Separation in Visible-Light-Responsive Polyoxometalate-Based Metal–Organic Frameworks for Highly Efficient Oxidative Coupling of Amines, *ACS Appl. Mater. Interfaces*, 2022, **14**, 27882–27890.

179 M. Zhang, C. Chen, W. Ma and J. Zhao, Visible-Light-Induced Aerobic Oxidation of Alcohols in a Coupled Photocatalytic System of Dye-Sensitized TiO<sub>2</sub> and TEMPO, *Angew. Chem., Int. Ed.*, 2008, **47**, 9730–9733.

180 X.-Z. Wei, F. Wondu Dagnaw, J. Liu and L. Ma, Highly selective photocatalytic oxidation of alcohols under the application of novel metal organic frameworks (MOFs) based catalytic system, *J. Colloid Interface Sci.*, 2023, **629**, 136–143.

181 Y. Xu, L. Zhu, Z. Lv, Y. Zhang, T. Miao, Q. Deng, Y. Wang, Z. Liang, X. Fu and L. Li, Design and fabrication of Zr-based MOF photocatalyst with functionalized moieties for CO<sub>2</sub> reduction and coupling selective oxidation of benzyl alcohol, *Appl. Catal. A*, 2024, **682**, 119826.

182 H. Liu, C. Xu, D. Li and H. Jiang, Photocatalytic Hydrogen Production Coupled with Selective Benzylamine Oxidation over MOF Composites, *Angew. Chem.*, 2018, **130**, 5477–5481.

183 D. Bai, J. Qiu, J. Li, S. Zhou, X. Cui, X. Tang, Y. Tang, W. Liu and B. Chen, Mesoporous Mixed-Metal–Organic Framework Incorporating a [Ru(Phen)<sub>3</sub>]<sup>2+</sup> Photosensitizer for Highly Efficient Aerobic Photocatalytic Oxidative Coupling of Amines, *ACS Appl. Mater. Interfaces*, 2023, **15**, 30320–30331.

184 X. Feng, Y. Pi, Y. Song, Z. Xu, Z. Li and W. Lin, Integration of Earth-Abundant Photosensitizers and Catalysts in Metal–Organic Frameworks Enhances Photocatalytic Aerobic Oxidation, *ACS Catal.*, 2021, **11**, 1024–1032.

185 S. Oudi, A. R. Oveisí, S. Daliran, M. Khajeh, R. Luque, U. Sen and H. García, Straightforward synthesis of a porous chromium-based porphyrinic metal-organic framework for visible-light triggered selective aerobic oxidation of benzyl alcohol to benzaldehyde, *Appl. Catal. A*, 2021, **611**, 117965.

186 Z. W. Jiang, Y. C. Zou, T. T. Zhao, S. J. Zhen, Y. F. Li and C. Z. Huang, Controllable Synthesis of Porphyrin-Based 2D Lanthanide Metal–Organic Frameworks with Thickness- and Metal-Node-Dependent Photocatalytic Performance, *Angew. Chem., Int. Ed.*, 2020, **59**, 3300–3306.

187 J. A. Johnson, J. Luo, X. Zhang, Y.-S. Chen, M. D. Morton, E. Echeverría, F. E. Torres and J. Zhang, Porphyrin-Metalation-Mediated Tuning of Photoredox Catalytic Properties in Metal–Organic Frameworks, *ACS Catal.*, 2015, **5**, 5283–5291.

188 L. Zeng, T. Liu, C. He, D. Shi, F. Zhang and C. Duan, Organized Aggregation Makes Insoluble Perylene Diimide

Efficient for the Reduction of Aryl Halides via Consecutive Visible Light-Induced Electron-Transfer Processes, *J. Am. Chem. Soc.*, 2016, **138**, 3958–3961.

189 C. Wang, Z. Xie, K. E. deKrafft and W. Lin, Doping Metal-Organic Frameworks for Water Oxidation, Carbon Dioxide Reduction, and Organic Photocatalysis, *J. Am. Chem. Soc.*, 2011, **133**, 13445–13454.

190 W.-J. Xu, B.-X. Huang, G. Li, F. Yang, W. Lin, J.-X. Gu, H.-G. Deng, Z.-G. Gu and H.-G. Jin, Donor-Acceptor Mixed-Naphthalene Diimide-Porphyrin MOF for Boosting Photocatalytic Oxidative Coupling of Amines, *ACS Catal.*, 2023, **13**, 5723–5732.

191 R. Zhang, Y. Liu, Z. Wang, P. Wang, Z. Zheng, X. Qin, X. Zhang, Y. Dai, M.-H. Whangbo and B. Huang, Selective photocatalytic conversion of alcohol to aldehydes by singlet oxygen over Bi-based metal-organic frameworks under UV-vis light irradiation, *Appl. Catal., B*, 2019, **254**, 463–470.

192 D. Xie, S. Li, W. Yang, S. Fan and Y. Feng, Selective Photocatalytic Conversion of Benzyl Alcohol to Benzaldehyde by Antimony(v) Porphyrin Metal-Organic Frameworks under Visible-Light Irradiation, *ChemistrySelect*, 2022, **7**, e202103521.

193 H. Li, Y. Yang, X. Jing, C. He and C. Duan, Mixed-ligand metal-organic frameworks as an effective photocatalyst for selective oxidation reaction, *Chem. Commun.*, 2023, **59**, 11220–11223.

194 B. Ge, Y. Ye, Y. Yan, H. Luo, Y. Chen, X. Meng, X. Song and Z. Liang, Thiazolo[5,4-*d*]thiazole-Based Metal-Organic Framework for Catalytic CO<sub>2</sub> Cycloaddition and Photocatalytic Benzylamine Coupling Reactions, *Inorg. Chem.*, 2023, **62**, 19288–19297.

195 L. Shi, L. Yang, H. Zhang, K. Chang, G. Zhao, T. Kako and J. Ye, Implantation of Iron(III) in porphyrinic metal organic frameworks for highly improved photocatalytic performance, *Appl. Catal., B*, 2018, **224**, 60–68.

196 M. Li, Y. Zhao, Y. Yang, R. Zhang, Y. Wang, Y. Teng, Z. Su and J. Zhang, High-Efficiency Photocatalytic Oxidation of Benzyl Alcohol by NH<sub>2</sub>-UiO-66-(Indole-2,3-Dione)-Fe, *Chem. - Asian J.*, 2024, **19**, e202400346.

197 Y. Isaka, Y. Kondo, Y. Kuwahara, K. Mori and H. Yamashita, Incorporation of a Ru complex into an amine-functionalized metal-organic framework for enhanced activity in photocatalytic aerobic benzyl alcohol oxidation, *Catal. Sci. Technol.*, 2019, **9**, 1511–1517.

198 C. Si, X. Liu, T. Zhang, J. Xu, J. Li, J. Fu and Q. Han, Constructing a Photocatalyst for Selective Oxidation of Benzyl Alcohol to Benzaldehyde by Photo-Fenton-like Catalysis, *Inorg. Chem.*, 2023, **62**, 4210–4219.

199 E.-M. Aro, I. Virgin and B. Andersson, Photoinhibition of Photosystem II. Inactivation, protein damage and turnover, *Biochim. Biophys. Acta, Bioenerg.*, 1993, **1143**, 113–134.

200 A. K. Mengele and S. Rau, Learning from Nature's Example: Repair Strategies in Light-Driven Catalysis, *JACS Au*, 2023, **3**, 36–46.

201 J. Chu, F.-S. Ke, Y. Wang, X. Feng, W. Chen, X. Ai, H. Yang and Y. Cao, Facile and reversible digestion and regeneration of zirconium-based metal-organic frameworks, *Commun. Chem.*, 2020, **3**, 5.

202 K. Shu, B. Guan, J. Guo, X. Wu, Y. Chen, Z. Ma, J. Zhang, J. Chen, S. Yao, S. Bao, X. Jiang, L. Chen, H. Dang, Z. Guo, Z. Li, J. Hu, C. Yi and Z. Huang, The Current Progresses and Future Perspectives of Photoreactors and Catalysts Used in Photocatalytic Reduction of CO<sub>2</sub>, *Ind. Eng. Chem. Res.*, 2023, **62**, 15699–15732.

203 M. Cabrero-Antonino, B. Ferrer, H. G. Baldoví and S. Navalón, Toward solar-driven photocatalytic CO<sub>2</sub> methanation under continuous flow operation using benchmark MIL-125(Ti)-NH<sub>2</sub> supported ruthenium nanoparticles, *Chem. Eng. J.*, 2022, **445**, 136426.

204 X. Chen, H. Jiang, B. Hou, W. Gong, Y. Liu and Y. Cui, Boosting Chemical Stability, Catalytic Activity, and Enantioselectivity of Metal-Organic Frameworks for Batch and Flow Reactions, *J. Am. Chem. Soc.*, 2017, **139**, 13476–13482.

205 B. Durham, J. V. Caspar, J. K. Nagle and T. J. Meyer, Photochemistry of tris(2,2'-bipyridine)ruthenium(2+) ion, *J. Am. Chem. Soc.*, 1982, **104**, 4803–4810.

206 A. Soupart, F. Alary, J.-L. Heully, P. I. P. Elliott and I. M. Dixon, Exploration of Uncharted <sup>3</sup> PES Territory for [Ru(bpy)<sub>3</sub>]<sup>2+</sup>: A New <sup>3</sup> MC Minimum Prone to Ligand Loss Photochemistry, *Inorg. Chem.*, 2018, **57**, 3192–3196.

207 A. Solé-Daura, Y. Benseghir, M.-H. Ha-Thi, M. Fontecave, P. Mialane, A. Dolbecq and C. Mellot-Draznieks, Origin of the Boosting Effect of Polyoxometalates in Photocatalysis: The Case of CO<sub>2</sub> Reduction by a Rh-Containing Metal-Organic Framework, *ACS Catal.*, 2022, **12**, 9244–9255.

208 S. Saeedi and T. A. White, Cu(I) photosensitizers with alkylated diphosphines: Towards enhancing photostability and architecture extension, *Inorg. Chim. Acta*, 2020, **512**, 119876.

209 P. S. Singh, H. C. Rudbeck, P. Huang, S. Ezzaher, L. Eriksson, M. Stein, S. Ott and R. Lomoth, (I,0) Mixed-Valence State of a Diiron Complex with Pertinence to the [FeFe]-Hydrogenase Active Site: An IR, EPR, and Computational Study, *Inorg. Chem.*, 2009, **48**, 10883–10885.

210 I. Aguirre de Carcer, A. DiPasquale, A. L. Rheingold and D. M. Heinekey, Active-Site Models for Iron Hydrogenases: Reduction Chemistry of Dinuclear Iron Complexes, *Inorg. Chem.*, 2006, **45**, 8000–8002.

211 S. Roy, V. Pascanu, S. Pullen, G. González Miera, B. Martín-Matute and S. Ott, Catalyst accessibility to chemical reductants in metal-organic frameworks, *Chem. Commun.*, 2017, **53**, 3257–3260.

212 J. Shipp, S. Parker, S. Spall, S. L. Peralta-Arriaga, C. C. Robertson, D. Chekulaev, P. Portius, S. Turega, A. Buckley, R. Rothman and J. A. Weinstein, Photocatalytic Reduction of CO<sub>2</sub> to CO in Aqueous Solution under Red-Light Irradiation by a Zn-Porphyrin-



Sensitized Mn(I) Catalyst, *Inorg. Chem.*, 2022, **61**, 13281–13292.

213 H. Takeda, K. Koike, H. Inoue and O. Ishitani, Development of an Efficient Photocatalytic System for CO<sub>2</sub> Reduction Using Rhenium(I) Complexes Based on Mechanistic Studies, *J. Am. Chem. Soc.*, 2008, **130**, 2023–2031.

214 X. Deng, J. Albero, L. Xu, H. García and Z. Li, Construction of a Stable Ru-Re Hybrid System Based on Multifunctional MOF-253 for Efficient Photocatalytic CO<sub>2</sub> Reduction, *Inorg. Chem.*, 2018, **57**, 8276–8286.

215 Z. Thompson and J. A. Cowan, Artificial Metalloenzymes: Recent Developments and Innovations in Bioinorganic Catalysis, *Small*, 2020, **16**, 2000392.

216 D. Kim, D. R. Whang and S. Y. Park, Self-Healing of Molecular Catalyst and Photosensitizer on Metal–Organic Framework: Robust Molecular System for Photocatalytic H<sub>2</sub> Evolution from Water, *J. Am. Chem. Soc.*, 2016, **138**, 8698–8701.

217 S. El Ghachoui, M. Fournier, S. Cherdö, R. Guillot, M.-F. Charlot, E. Anxolabéhère-Mallart, M. Robert and A. Aukauloo, Monometallic Cobalt–Trisglyoximato Complexes as Precatalysts for Catalytic H<sub>2</sub> Evolution in Water, *J. Phys. Chem. C*, 2013, **117**, 17073–17077.

218 E. Anxolabéhère-Mallart, C. Costentin, M. Fournier, S. Nowak, M. Robert and J.-M. Savéant, Boron-Capped Tris(glyoximato) Cobalt Clathrochelate as a Precursor for the Electrodeposition of Nanoparticles Catalyzing H<sub>2</sub> Evolution in Water, *J. Am. Chem. Soc.*, 2012, **134**, 6104–6107.

219 S. Roy, A. Bhunia, N. Schuth, M. Haumann and S. Ott, Light-driven hydrogen evolution catalyzed by a cobaloxime catalyst incorporated in a MIL-101(Cr) metal–organic framework, *Sustainable Energy Fuels*, 2018, **2**, 1148–1152.

220 D. Yang and B. C. Gates, Analyzing Stabilities of Metal–Organic Frameworks: Correlation of Stability with Node Coordination to Linkers and Degree of Node Metal Hydrolysis, *J. Phys. Chem. C*, 2024, **128**, 8551–8559.

221 Y. Keum, S. Park, Y. Chen and J. Park, Titanium–Carboxylate Metal–Organic Framework Based on an Unprecedented Ti–Oxo Chain Cluster, *Angew. Chem., Int. Ed.*, 2018, **57**, 14852–14856.

222 G.-L. Yang, Y. Xie, Z.-H. Jiao, J. Zhao, S.-L. Hou, Y. Shi, J. Han and B. Zhao, A strong-alkali resistant zinc–organic framework with 1,3,6,8-tetra(pyridin-4-yl)pyrene for efficient photocatalytic hydrogen evolution, *J. Mater. Chem. A*, 2023, **11**, 16255–16262.

223 X. Kong, T. He, J. Zhou, C. Zhao, T. Li, X. Wu, K. Wang and J. Li, In Situ Porphyrin Substitution in a Zr(IV)–MOF for Stability Enhancement and Photocatalytic CO<sub>2</sub> Reduction, *Small*, 2021, **17**, 2005357.

224 Z. Jin, D. Liu, X. Liu, P. Chen, D. Chen, H. Xing and X. Liu, Hydrophobic Porphyrin Titanium-Based MOFs for Visible-Light-Driven CO<sub>2</sub> Reduction to Formate, *Inorg. Chem.*, 2024, **63**, 1499–1506.

225 Q. Mo, L. Zhang, S. Li, H. Song, Y. Fan and C.-Y. Su, Engineering Single-Atom Sites into Pore-Confining Nanospaces of Porphyrinic Metal–Organic Frameworks for the Highly Efficient Photocatalytic Hydrogen Evolution Reaction, *J. Am. Chem. Soc.*, 2022, **144**, 22747–22758.

226 C. Lu, D. Xiong, C. Chen, J. Wang, Y. Kong, T. Liu, S. Ying and F.-Y. Yi, Indium-Based Metal–Organic Framework for Efficient Photocatalytic Hydrogen Evolution, *Inorg. Chem.*, 2022, **61**, 2587–2594.

227 G.-Q. Lai, Z. Jiang, H. Zhong, L.-H. Chung, N. Li and J. He, UiO-66 framework equipped with cadmium-thiocatecholato moieties as photocatalyst bearing stable active sites and intrinsic photosensitizing units for hydrogen evolution reaction, *Chin. J. Struct. Chem.*, 2023, **42**, 100090.

228 S. Yang, B. Pattengale, S. Lee and J. Huang, Real-Time Visualization of Active Species in a Single-Site Metal–Organic Framework Photocatalyst, *ACS Energy Lett.*, 2018, **3**, 532–539.

229 Y. Diao, N. Xu, M.-Q. Li, X. Zhu and Z. Xu, Porphyrin Grafting on a Mercapto-Equipped Zr(IV)-Carboxylate Framework Enhances Photocatalytic Hydrogen Production, *Inorg. Chem.*, 2020, **59**, 12643–12649.

230 J. Bai, J. Wang, H. Zheng, X. Zhao, P. Wu, L. Pei and J. Wang, Modulating Photoinduced Electron Transfer between Photosensitive MOF and Co(II) Proton Reduction Sites for Boosting Photocatalytic Hydrogen Production, *Small*, 2023, **19**, 2305024.

231 X. Kong, Z. Lin, Z. Zhang, T. Zhang and W. Lin, Hierarchical Integration of Photosensitizing Metal–Organic Frameworks and Nickel-Containing Polyoxometalates for Efficient Visible-Light-Driven Hydrogen Evolution, *Angew. Chem.*, 2016, **128**, 6521–6526.

232 H. Zhong, S. Chen, Z. Jiang, J. Hu, J. Dong, L. Chung, Q. Lin, W. Ou, L. Yu and J. He, Utilizing Metal–Thiocatecholate Functionalized UiO-66 Framework for Photocatalytic Hydrogen Evolution Reaction, *Small*, 2023, **19**, 2207266.

233 Y. Kataoka, K. Sato, Y. Miyazaki, K. Masuda, H. Tanaka, S. Naito and W. Mori, Photocatalytic hydrogen production from water using porous material [Ru2(p-BDC)2]n, *Energy Environ. Sci.*, 2009, **2**, 397.

234 Y. Kataoka, Y. Miyazaki, K. Sato, T. Saito, Y. Nakanishi, Y. Kiatagwa, T. Kawakami, M. Okumura, K. Yamaguchi and W. Mori, Modification of MOF catalysts by manipulation of counter-ions: experimental and theoretical studies of photochemical hydrogen production from water over microporous diruthenium (II, III) coordination polymers, *Supramol. Chem.*, 2011, **23**, 287–296.

235 A. Fateeva, P. A. Chater, C. P. Ireland, A. A. Tahir, Y. Z. Khimyak, P. V. Wiper, J. R. Darwent and M. J. Rosseinsky, A water-stable porphyrin-based metal–organic framework active for visible-light photocatalysis, *Angew. Chem., Int. Ed.*, 2012, **51**, 7440–7444.

236 S. Li, H. M. Mei, S. L. Yao, Z. Y. Chen, Y. L. Lu, L. Zhang and C. Y. Su, Well-distributed Pt-nanoparticles within con-

fined coordination interspaces of self-sensitized porphyrin metal-organic frameworks: Synergistic effect boosting highly efficient photocatalytic hydrogen evolution reaction, *Chem. Sci.*, 2019, **10**, 10577–10585.

237 R. Abazari, S. Sanati, N. Li and J. Qian, Fluorinated Metal–Organic Frameworks with Dual-Functionalized Linkers to Enhance Photocatalytic H<sub>2</sub> Evolution and High Water Adsorption, *Inorg. Chem.*, 2023, **62**, 18680–18688.

238 L. Liu, Y. Xiao, X. Guo, W. Fan, N. Yang, C. Jia, S. Jin and F. Zhang, One-dimensional nanotube of a metal–organic framework boosts charge separation and photocatalytic hydrogen evolution from water: synthesis and underlying understanding, *EES Catal.*, 2024, **2**, 789–794.

239 L. Tayebi, R. Rahimi and A. R. Akbarzadeh, Enhanced Photocatalytic CO<sub>2</sub> Reduction by Novel Designed Porphyrin-Based MOFs: From Accurate QSPR Model to Experimental Exploration, *ACS Omega*, 2022, **7**, 40869–40881.

240 N.-Y. Huang, J.-Q. Shen, X.-W. Zhang, P.-Q. Liao, J.-P. Zhang and X.-M. Chen, Coupling Ruthenium Bipyridyl and Cobalt Imidazolate Units in a Metal–Organic Framework for an Efficient Photosynthetic Overall Reaction in Diluted CO<sub>2</sub>, *J. Am. Chem. Soc.*, 2022, **144**, 8676–8682.

241 S. Choi, W.-J. Jung, K. Park, S.-Y. Kim, J.-O. Baeg, C. H. Kim, H.-J. Son, C. Pac and S. O. Kang, Rapid Exciton Migration and Amplified Funneling Effects of Multi-Porphyrin Arrays in a Re(I)/Porphyrinic MOF Hybrid for Photocatalytic CO<sub>2</sub> Reduction, *ACS Appl. Mater. Interfaces*, 2021, **13**, 2710–2722.

242 H. Liu, D. Si, M. F. Smith, R. Li, X. Li, L. Li, H. Huang, Z. Fang, H. Zhou and T. Liu, Efficient CO<sub>2</sub> photoreduction enabled by the energy transfer pathway in metal–organic framework, *Aggregate*, 2023, **4**, e383.

243 S. Xie, C. Deng, Q. Huang, C. Zhang, C. Chen, J. Zhao and H. Sheng, Facilitated Photocatalytic CO<sub>2</sub> Reduction in Aerobic Environment on a Copper–Porphyrin Metal–Organic Framework, *Angew. Chem., Int. Ed.*, 2023, **62**, e202216717.

244 M. Cheng, P. Yan, X. Zheng, B. Gao, X. Yan, G. Zhang, X. Cui and Q. Xu, Porphyrin-based Bi-MOFs with Enriched Surface Bi Active Sites for Boosting Photocatalytic CO<sub>2</sub> Reduction, *Chem. – Eur. J.*, 2023, **29**, e202302395.

245 M. Cheng, B. Gao, X. Zheng, W. Wu, W. Kong, P. Yan, Z. Wang, B. An, Y. Zhang, Q. Li and Q. Xu, CO<sub>2</sub>-assisted rapid synthesis of porphyrin-based Bi-MOFs for photocatalytic CO<sub>2</sub> reduction: An efficient strategy for carbon cycle, *Appl. Catal., B*, 2024, **353**, 124097.

246 Q. Shi, M.-H. Chen, J. Xiong, T. Li, Y.-Q. Feng and B. Zhang, Porphyrin-Based Two-Dimensional Metal–Organic framework nanosheets for efficient photocatalytic CO<sub>2</sub> transformation, *Chem. Eng. J.*, 2024, **481**, 148301.

247 Z. Wei, W. Xu, P. Peng, Q. Sun, Y. Li, N. Ding, C. Zhao, S. Li and S. Pang, Covalent synthesis of Ti-MOF for enhanced photocatalytic CO<sub>2</sub> reduction, *Mol. Catal.*, 2024, **558**, 114042.

248 T.-C. Zhuo, Y. Song, G.-L. Zhuang, L.-P. Chang, S. Yao, W. Zhang, Y. Wang, P. Wang, W. Lin, T.-B. Lu and Z.-M. Zhang, H-Bond-Mediated Selectivity Control of Formate versus CO during CO<sub>2</sub> Photoreduction with Two Cooperative Cu/X Sites, *J. Am. Chem. Soc.*, 2021, **143**, 6114–6122.

249 M. Liu, Y.-F. Mu, S. Yao, S. Guo, X.-W. Guo, Z.-M. Zhang and T.-B. Lu, Photosensitizing single-site metal–organic framework enabling visible-light-driven CO<sub>2</sub> reduction for syngas production, *Appl. Catal., B*, 2019, **245**, 496–501.

250 Z. Wang, P. Yeary, Y. Fan, C. Deng and W. Lin, Active Site Isolation and Enhanced Electron Transfer Facilitate Photocatalytic CO<sub>2</sub> Reduction by A Multifunctional Metal–Organic Framework, *ACS Catal.*, 2024, **14**, 9217–9223.

251 R. Huang, Y. Peng, C. Wang, Z. Shi and W. Lin, A Rhodium–Functionalized Metal–Organic Framework as a Single-Site Catalyst for Photochemical Reduction of Carbon Dioxide, *Eur. J. Inorg. Chem.*, 2016, **2016**, 4358–4362.

252 D. Sun, Y. Gao, J. Fu, X. Zeng, Z. Chen and Z. Li, Construction of a supported Ru complex on bifunctional MOF-253 for photocatalytic CO<sub>2</sub> reduction under visible light, *Chem. Commun.*, 2015, **51**, 2645–2648.

253 Y. Liu, Y. Yang, Q. Sun, Z. Wang, B. Huang, Y. Dai, X. Qin and X. Zhang, Chemical Adsorption Enhanced CO<sub>2</sub> Capture and Photoreduction over a Copper Porphyrin Based Metal Organic Framework, *ACS Appl. Mater. Interfaces*, 2013, **5**, 7654–7658.

254 H. Zhang, J. Wei, J. Dong, G. Liu, L. Shi, P. An, G. Zhao, J. Kong, X. Wang, X. Meng, J. Zhang and J. Ye, Efficient Visible-Light-Driven Carbon Dioxide Reduction by a Single-Atom Implanted Metal–Organic Framework, *Angew. Chem., Int. Ed.*, 2016, **55**, 14310–14314.

255 S. Fu, S. Yao, S. Guo, G.-C. Guo, W. Yuan, T.-B. Lu and Z.-M. Zhang, Feeding Carbonylation with CO<sub>2</sub> via the Synergy of Single-Site/Nanocluster Catalysts in a Photosensitizing MOF, *J. Am. Chem. Soc.*, 2021, **143**, 20792–20801.

256 X. Zhao, C.-Y. Zhu, H. Rao, D.-Y. Du, M. Zhang, P. She, L. Li and J.-S. Qin, Local microenvironment modulation of zirconium-porphyrinic frameworks for CO<sub>2</sub> reduction, *Chem. Eng. J.*, 2024, **496**, 153875.

257 X. Zhao, C.-Y. Zhu, J.-S. Qin, H. Rao, D.-Y. Du, M. Zhang, P. She, L. Li and Z.-M. Su, Local protons enhance photocatalytic CO<sub>2</sub> reduction by porphyrinic zirconium-organic frameworks, *Mater. Chem. Front.*, 2024, **8**, 2439–2446.

258 P. M. Stanley and J. Warnan, Molecular Dye-Sensitized Photocatalysis with Metal-Organic Framework and Metal Oxide Colloids for Fuel Production,  *Energies*, 2021, **14**, 4260.

259 O.-Y. Yang, X.-J. Gao, G.-D. Qi, Y. Wang, W.-W. Dong, Z.-F. Tian, J. Zhao, D.-S. Li and Q. Zhang, Dye-Anchoring Strategy with a Metal–Organic Framework for a Highly



Efficient Visible-Light-Driven Photocatalytic  $\text{CO}_2$  Reduction through the Solid–Gas Mode, *ACS Appl. Energy Mater.*, 2023, **6**, 334–341.

260 W. Lian, Y. Huang, Q. Yin, Z. Guo, Y. Xu and T. Miao, Syntheses of heterometallic organic frameworks catalysts via multicomponent postmodification: For improving  $\text{CO}_2$  photoreduction efficiency, *J. Colloid Interface Sci.*, 2024, **675**, 94–103.

261 Y. Lee, S. Kim, H. Fei, J. K. Kang and S. M. Cohen, Photocatalytic  $\text{CO}_2$  reduction using visible light by metal-monocatecholate species in a metal–organic framework, *Chem. Commun.*, 2015, **51**, 16549–16552.

262 C. Zheng, X. Qiu, J. Han, Y. Wu and S. Liu, Zero-Dimensional-g-CNQD-Coordinated Two-Dimensional Porphyrin MOF Hybrids for Boosting Photocatalytic  $\text{CO}_2$  Reduction, *ACS Appl. Mater. Interfaces*, 2019, **11**, 42243–42249.

263 Y. Dong, Y. Jiang, S. Ni, G. Guan, S. Zheng, Q. Guan, L. Pei and Q. Yang, Ligand Defect-Induced Active Sites in Ni-MOF-74 for Efficient Photocatalytic  $\text{CO}_2$  Reduction to  $\text{CO}$ , *Small*, 2024, **20**, 2308005.

264 X. Gao, B. Guo, C. Guo, Q. Meng, J. Liang and J. Liu, Zirconium-Based Metal–Organic Framework for Efficient Photocatalytic Reduction of  $\text{CO}_2$  to  $\text{CO}$ : The Influence of Doped Metal Ions, *ACS Appl. Mater. Interfaces*, 2020, **12**, 24059–24065.

265 J. Wang, K. Sun, D. Wang, X. Niu, Z. Lin, S. Wang, W. Yang, J. Huang and H.-L. Jiang, Precise Regulation of the Coordination Environment of Single  $\text{Co}(\text{II})$  Sites in a Metal–Organic Framework for Boosting  $\text{CO}_2$  Photoreduction, *ACS Catal.*, 2023, **13**, 8760–8769.

266 J. Li, H. Huang, W. Xue, K. Sun, X. Song, C. Wu, L. Nie, Y. Li, C. Liu, Y. Pan, H. L. Jiang, D. Mei and C. Zhong, Self-adaptive dual-metal-site pairs in metal-organic frameworks for selective  $\text{CO}_2$  photoreduction to  $\text{CH}_4$ , *Nat. Catal.*, 2021, **4**, 719–729.

267 T. Kajiwara, M. Fujii, M. Tsujimoto, K. Kobayashi, M. Higuchi, K. Tanaka and S. Kitagawa, Photochemical Reduction of Low Concentrations of  $\text{CO}_2$  in a Porous Coordination Polymer with a Ruthenium(II)–CO Complex, *Angew. Chem., Int. Ed.*, 2016, **55**, 2697–2700.

268 S. Wang, W. Yao, J. Lin, Z. Ding and X. Wang, Cobalt Imidazolate Metal–Organic Frameworks Photosplit  $\text{CO}_2$  under Mild Reaction Conditions, *Angew. Chem., Int. Ed.*, 2014, **53**, 1034–1038.

269 B. Han, X. Ou, Z. Deng, Y. Song, C. Tian, H. Deng, Y. Xu and Z. Lin, Nickel Metal–Organic Framework Monolayers for Photoreduction of Diluted  $\text{CO}_2$ : Metal–Node-Dependent Activity and Selectivity, *Angew. Chem.*, 2018, **130**, 17053–17057.

270 K. M. Choi, D. Kim, B. Rungtaweevoranit, C. A. Trickett, J. T. D. Barmanbek, A. S. Alshammari, P. Yang and O. M. Yaghi, Plasmon-Enhanced Photocatalytic  $\text{CO}_2$  Conversion within Metal–Organic Frameworks under Visible Light, *J. Am. Chem. Soc.*, 2017, **139**, 356–362.

271 L. Ye, Y. Gao, S. Cao, H. Chen, Y. Yao, J. Hou and L. Sun, Assembly of highly efficient photocatalytic  $\text{CO}_2$  conversion systems with ultrathin two-dimensional metal–organic framework nanosheets, *Appl. Catal., B*, 2018, **227**, 54–60.

272 P. M. Stanley, M. Parkulab, B. Rieger, J. Warnan and R. A. Fischer, Understanding entrapped molecular photosystem and metal–organic framework synergy for improved solar fuel production, *Faraday Discuss.*, 2021, **231**, 281–297.

273 X. Wang, J. Li, M. Kou, W. Dou, D. Bai, X. Tang, Y. Tang and W. Liu, Dual-Function Precious-Metal-Free Metal–Organic Framework for Photocatalytic Conversion and Chemical Fixation of Carbon Dioxide, *Inorg. Chem.*, 2023, **62**, 19015–19024.

274 Y.-L. Dong, H.-R. Liu, S.-M. Wang, G.-W. Guan and Q.-Y. Yang, Immobilizing Isatin-Schiff Base Complexes in  $\text{NH}_2$ -UiO-66 for Highly Photocatalytic  $\text{CO}_2$  Reduction, *ACS Catal.*, 2023, **13**, 2547–2554.

275 S. R. V. Parambil, F. A. Rahimi, R. Ghosh, S. Nath and T. K. Maji, Pore-Confined  $\pi$ -Chromophoric Tetracene as a Visible Light Harvester toward MOF-Based Photocatalytic  $\text{CO}_2$  Reduction in Water, *Inorg. Chem.*, 2023, **62**, 19312–19322.

276 S. Zhang, L. Li, S. Zhao, Z. Sun and J. Luo, Construction of Interpenetrated Ruthenium Metal–Organic Frameworks as Stable Photocatalysts for  $\text{CO}_2$  Reduction, *Inorg. Chem.*, 2015, **54**, 8375–8379.

277 S. Zhang, L. Li, S. Zhao, Z. Sun, M. Hong and J. Luo, Hierarchical metal–organic framework nanoflowers for effective  $\text{CO}_2$  transformation driven by visible light, *J. Mater. Chem. A*, 2015, **3**, 15764–15768.

278 H. Hu, Z. Wang, L. Cao, L. Zeng, C. Zhang, W. Lin and C. Wang, Metal–organic frameworks embedded in a liposome facilitate overall photocatalytic water splitting, *Nat. Chem.*, 2021, **13**, 358–366.

279 C. Wang, Z. Xie, K. E. deKrafft and W. Lin, Doping Metal–Organic Frameworks for Water Oxidation, Carbon Dioxide Reduction, and Organic Photocatalysis, *J. Am. Chem. Soc.*, 2011, **133**, 13445–13454.

280 J. H. Tang, G. Han, G. Li, K. Yan and Y. Sun, Near-infrared light photocatalysis enabled by a ruthenium complex-integrated metal–organic framework via two-photon absorption, *iScience*, 2022, **25**, 104064.

281 K. Wu, X.-Y. Liu, P.-W. Cheng, Y.-L. Huang, J. Zheng, M. Xie, W. Lu and D. Li, Linker Engineering for Reactive Oxygen Species Generation Efficiency in Ultra-Stable Nickel-Based Metal–Organic Frameworks, *J. Am. Chem. Soc.*, 2023, **145**, 18931–18938.

